

# MODELING NONLOCALITY IN QUANTUM SYSTEMS

A Dissertation

Submitted to the Faculty

of

Purdue University

by

James A. Charles

In Partial Fulfillment of the

Requirements for the Degree

of

Doctor of Philosophy

December 2018

Purdue University

West Lafayette, Indiana

**THE PURDUE UNIVERSITY GRADUATE SCHOOL**  
**STATEMENT OF COMMITTEE APPROVAL**

Dr. Tillmann Kubis, Co-chair

Department of Electrical and Computer Engineering

Dr. Gerhard Klimeck, Co-chair

Department of Electrical and Computer Engineering

Dr. Sabre Kais

Department of Chemistry

Dr. Zhihong Chen

Department of Electrical and Computer Engineering

**Approved by:**

Dr. Pedro Irazoqui

Head of the Graduate Program

## ACKNOWLEDGMENTS

I would like to express my gratitude to my co-advisor, Professor Tillmann Kubis, for his support during these years. His direction and continuous support during my PhD has been invaluable in learning how to conduct research. I would also like to thank my other co-advisor, Professor Gerhard Klimeck for his helpful discussions and suggestions. He helped guide the research by looking at the big picture. Additionally, thank you to my other committee members Professor Zhihong Chen and Professor Sabre Kais. Professor Chen made sure that the experimental side of things was always considered. Professor Kais gave his advice and insights as an expert in chemistry. They were invaluable members of my PhD committee and helped guide the research. Thanks also to my preliminary committee member Dmitri Nikinov for his questions and insights from an industrial perspective.

I would also like to thank my friends and family for their support both professionally and personally. They were always there for me when I needed it. Finally, I would like to thank my wife, Alicia Charles, for her never-ending support during my PhD. She made the five year journey much easier and more enjoyable.

## TABLE OF CONTENTS

	Page
LIST OF FIGURES . . . . .	vi
SYMBOLS . . . . .	ix
ABSTRACT . . . . .	x
1 INTRODUCTION . . . . .	1
1.1 Overview . . . . .	1
1.1.1 Non-Equilibrium Green's Function Method . . . . .	1
1.1.2 Outline of this Thesis . . . . .	1
1.2 Motivation Part I: Modeling of Nonlocal Scattering in Quantum Systems	2
1.2.1 Scattering in Ultra-Scaled Devices . . . . .	2
1.2.2 The important of non-local scattering . . . . .	3
1.3 Motivation Part II: Towards NEGF in liquid systems . . . . .	4
1.3.1 Modeling molecules in a liquid . . . . .	4
2 PART I: STATE OF THE ART OF MODELING SCATTERING IN QUAN- TUM SYSTEMS . . . . .	8
2.1 Dyson and Keldysh Equations . . . . .	8
2.2 Local Electron-Phonon Scattering Self-energies . . . . .	9
2.2.1 Electron Density and Current . . . . .	17
2.2.2 Algorithm Flow . . . . .	18
2.3 How to solve the Keldysh and Dyson Equations? . . . . .	18
2.3.1 Traditional Recursive Green's Function Algorithm . . . . .	20
3 LOCAL SCATTERING RESULTS . . . . .	23
3.1 Silicon TFET . . . . .	23
3.2 Resonance TFET . . . . .	24
4 NEW NONLOCAL RECURSIVE GREEN'S FUNCTION ALGORITHM . .	30

	Page
4.1 Validation : Nonlocal Recursive Green's Function Algorithm . . . . .	30
4.2 Nonlocal Recursive Green's Function Derivation and Details . . . . .	39
4.2.1 General concept for the retarded Green's function . . . . .	39
4.2.2 Recursive Green's Function Algorithm Overview . . . . .	40
4.2.3 Forward recursive Green's function . . . . .	40
4.2.4 Backward recursive Green's function . . . . .	44
4.3 Non-local Recursive Green's Function Results . . . . .	45
5 PART II: OVERVIEW OF THE STATE OF THE ART OF MODELING CHEMICAL SYSTEMS IN LIQUIDS . . . . .	47
5.1 Overview of Density Functional Theory and its Applications . . . . .	47
5.1.1 Thermal and Excited State Density Functional Theory . . . . .	48
5.1.2 Density Functional Theory Applied to Water . . . . .	49
5.1.3 Implicit Solvent Models . . . . .	50
5.2 Molecular Electronics . . . . .	51
6 IMPLICIT, EXPLICIT AND HYBRID SOLVENT METHODS . . . . .	53
6.1 General Ingredients for Implicit Solvent Methods . . . . .	53
6.2 General Ingredients for Explicit Solvent Methods . . . . .	59
6.3 Hybrid Methods . . . . .	60
7 HAMILTONIAN - DESCRIPTION OF THE SYSTEM . . . . .	64
7.1 Overview of Different Tight-Binding Theories . . . . .	64
7.1.1 Density Functional Tight-Binding . . . . .	66
7.2 DFTB Bandstructure and Density of States . . . . .	70
8 NON-EQUILIBRIUM GREEN'S FUNCTION OPEN BOUNDARY CON- DITION SOLUTION METHODS . . . . .	73
8.1 Sancho Rubio . . . . .	73
8.2 Transfer Matrix . . . . .	74
8.3 Scattering in the Leads . . . . .	77
8.4 General Leads . . . . .	77

	Page
9 EXTENSION OF NON-EQUILIBRIUM GREEN'S FUNCTION FOR ARBITRARY THREE-DIMENSIONAL LIQUID LEADS . . . . .	81
9.1 Verification . . . . .	81
9.2 Nonequilibrium Green's Function with Crystalline Lead Results . . . .	83
9.3 Hamiltonian for Liquid Leads . . . . .	86
9.4 Extension of Thermodynamic Integration for Quantum Mechanical Calculations . . . . .	88
9.5 Future Outlook . . . . .	92
10 CONCLUSION . . . . .	94
REFERENCES . . . . .	97
PUBLICATIONS . . . . .	105
VITA . . . . .	109

## LIST OF FIGURES

Figure	Page
1.1 Contribution of different scattering mechanisms to the mobility of a single layer MoS2 device for different temperatures. The data is obtained from [27].	5
1.2 Contribution of different scattering mechanisms to the mobility of a two-dimensional electron gas of GaAs. The data is obtained from [28]. . . . .	6
2.1 Overview of the Poisson and Self-consistent Born approximation iterative approach used . . . . .	19
2.2 Recursive Green's function Algorithm Overview . . . . .	20
3.1 Schematic of a PIN circular nanowire TFET that is simulated. . . . .	24
3.2 Comparison of scattered to ballistic transfer characteristics for a 3nm circular nanowire TFET with a $V_{ds} = 1.0V$ . Two scattered cases are shown. With and without energy renormalization. Including energy renormalization increases the phonon-assisted tunneling and thus increases current. . .	25
3.3 Comparison of scattered to ballistic DOS near the transition region at $x = 8$ nm for the IV in figure 5 at $V_{gs} = 0.6$ V. The energy shift between scattered and ballistic is about 16 meV. . . . .	26
3.4 Cross-sectional schematics of a triple-HJ TFET. Schematic design obtained from [53]. . . . .	27
3.5 IV Characteristics for the Resonance TFET comparison ballistic to local scattering with different scattering strengths. Optical C is used the Silicon non-polar deformation constant value of 110 eV/nm. Optical B is approximately two times this value and Optical A is four times optical C. .	28
3.6 Subthreshold Slope comparison for the different configurations. Optical C is used the Silicon non-polar deformation constant value of 110 eV/nm. Optical B is approximately two times this value and Optical A is four times optical C. [53]. . . . .	29
4.1 Current-voltage comparison for traditional RGF and nonlocal RGF. . . .	31
4.2 Numerical comparison of $G^R$ calculated with non-local RGF and with full inversion. Note: Same atom orbitals are summed for clarity. . . . .	32

Figure	Page
4.3 The anti-diagonal of $\Sigma_{POP}^R$ comparison of full inversion and NL-RGF for different screening lengths. The lines are full-inversion and the symbols are NL-RGF. . . . .	33
4.4 Timing for NL-RGF as a function of non-locality in the transport direction. For comparison, the timing is plotted against the traditional (local) RGF. . . . .	34
4.5 Memory for NL-RGF as a function of non-locality in the transport direction. For comparison, the memory is plotted against the traditional (local) RGF. . . . .	35
4.6 Timing for NL-RGF as a function of non-locality in the transport direction for three different sizes of slabs. A horizontal line at the ratio of non-local to local time of 150 is added to guide the eye. . . . .	36
4.7 Memory for NL-RGF as a function of non-locality in the transport direction for three different sizes of slabs. . . . .	37
4.8 The theoretical comparison of complexity of NL-RGF to full inversion. The break even point is marked with a red dashed line to guide the eye. . . . .	38
4.9 IV characteristics for a 2nm diameter InGaAs wire in effective mass. The ballistic result is also shown for comparison. . . . .	46
5.1 Typical molecular electronic simulation setup. The molecule is placed between two ideal copper contacts. The delineation between the device and the infinite, ideal, and equilibrium leads is shown with a vertical dashed line on both sides. . . . .	52
6.1 A schematic of the different components that makeup the implicit solvent method. . . . .	56
6.2 Example of Lennard Jones Potential including the different contributions. . . . .	60
6.3 A schematic of the structure in the explicit solvent method. Acetone is surrounded by water. The dashed line represents the mathematical boundary conditions. . . . .	61
7.1 Comparison between density functional theory (solid lines) and tight-binding (open circles) for bulk Copper. The Fermi level is denoted with a solid red line. The bands are each colored with a different color to guide the eye. . . . .	65
7.2 Bulk bandstructure of TiO. The fermi level is marked with a horizontal dash line and the points of high symmetry are marked with vertical dashed lines. . . . .	71



Figure	Page
7.3 The Density of States of TiO. The fermi level is marked with a horizontal dash line. The local density of states on each atom for each orbital is also shown. . . . .	72
8.1 Scattering in the leads algorithm used in all subsequent scattering calculations.	77
8.2 Electron density projected along the transport direction for a simple homogeneous Silicon nanowire of length 10nm and cross section 2nm. Without scattering in the leads, the density is not constant even though the device is effectively infinite. This is caused by artifical reflections due a discontinuous DOS between the lead and device interface. . . . .	78
8.3 Comparison of ideal leads, InAs, and alloy in the device region and alloy everywhere for an InGaAs nanowire. Figure is obtained from [103]. . . . .	80
9.1 Schematic of the model. The device/lead interface needed for the NEGF algorithm is shown on the left. The model abstraction is shown on the right. . . . .	82
9.2 Schematic of the system for verification. A large sphere of Silicon is taken with a device/lead interface chosen. . . . .	83
9.3 Position-resolved density of states of a sphere of Silicon when the lead is purposefully made too small. . . . .	84
9.4 Position-resolved density of states of a sphere of Silicon when the lead is made large enough to reduce variations in the DOS. . . . .	85
9.5 Comparison of band gap calculated from the periodic silicon band structure and the projected 3D density of states. . . . .	85
9.6 The density of states calculated from NEGF near the LUMO of caffeine. The coupling is varied from 0 (no coupling) to 1 (full coupling). . . . .	87
9.7 DFTB relaxed structure with methane embedded in water. . . . .	88
9.8 $\frac{dE}{d\lambda}$ profiles for methane and acetone using the DFTB-relaxed method. Implicit solvent method values are from [108] using DFTB. . . . .	92

## SYMBOLS

$\epsilon$	dielectric constant
$\epsilon_R$	relative dielectric constant
$\epsilon_\infty$	relative dielectric constant for infinite frequency
$\epsilon_s$	relative dielectric constant DC
$n_0$	phonon occupation number
$q$	charge of an electron
$\lambda$	variational coupling parameter used in thermodynamic integration
$\eta$	dephasing value for general leads algorithm

## ABSTRACT

Charles, James A. Ph.D., Purdue University, December 2018. Modeling Nonlocality in Quantum Systems. Major Professors: Tillmann Kubis, Gerhard Klimeck.

The widely accepted Non-equilibrium Greens functions (NEGF) method and the Self-Consistent Born Approximation, to include scattering, is employed. Due to the large matrix sizes typically needed when solving Greens functions, an efficient recursive algorithm is typically utilized. However, the current state of the art of this so-called recursive Greens function algorithm only allows the inclusion of local scattering or non-locality within a limited range. Most scattering mechanisms are Coulombic and are therefore non-local. Recently, we have developed an addition to the recursive Greens function algorithm that can handle arbitrary non-locality. Validation and performance will be assessed for nanowires.

The second half of this work discusses the modeling of an active ingredient in a liquid environment. The state of the art is outlined with options for different modeling approaches – mainly the implicit and the explicit solvation model. Extensions of the explicit model to include an open, quantum environment is the main work of the second half. First results for an extension of the commonly used molecular dynamics with thermodynamic integration are also presented.

# 1. INTRODUCTION

## 1.1 Overview

### 1.1.1 Non-Equilibrium Green's Function Method

#### Introduction

The non-equilibrium Green's function (NEGF) has shown a wide range of utilities in varying applications such as electron transport [1], [2], thermal transport [3], and optoelectronics [4], [5]. The theory was first introduced by Schwinger (1961) [6], Kadanoff and Baym (1962) [7] and Fujita (1964) [8]. Thermal fluctuations and interactions with the environment are typically considered in a consistent way within the self-consistent Born approximation (SCBA) as a perturbation.

### 1.1.2 Outline of this Thesis

This proposal is broken down into two topics. At first glance, the two topics may seem separate and distinct but the connection between them will be made clear in future chapters. The first topic discussed is scattering in ultra-scaled devices. The first goal will be to motivate why scattering is important in ultra-scaled devices of diverse applications and then motivate what non-local scattering is and why accurate modeling of non-local scattering is important for device predictions. The second topic is the application to the NEGF method to molecules in a liquid. The state of the art will be discussed and what is missing. The motivation for using NEGF in these applications will be made. The details of the modeling and method will be discussed in future chapters.

## 1.2 Motivation Part I: Modeling of Nonlocal Scattering in Quantum Systems

### 1.2.1 Scattering in Ultra-Scaled Devices

Most applications in real-world experiments are affected by thermal fluctuations and other interactions with the environment. Additionally, there are device to device variations that must be accounted for in an accurate and quantitative predictive model. Below, I will give three examples and the effect that scattering has on them.

#### Logic Devices

The first example is a transistor or more specifically a tunneling field effect transistor. The state of the art logic devices have reached the nanometer length scale. The International Technology Road for Semiconductors (ITRS) predict sub-10 nm critical lengths in order to keep up with Moore's law. This means there will be a countable number of atoms in the active part of the device. Even variations of a few atoms will affect the device performance and must be accounted for.

In addition, as the devices scale down, the experiments become more expensive and complex. This further necessitates accurate and predictive modeling on the nanoscale. There are several sources of variations in transistors – any device imperfections such as surface roughness [9], [10], [11], random alloy distributions [12], and interactions with the lattice that manifest as phonons or quantized vibrations. Electron-phonon scattering decreases the on-current in nanowires [13], [14]. Additionally, scattering increases the off-current due to phonon-assisted tunneling and causes band-tails to form [15], [16]. These issues manifest themselves as a degraded subthreshold slope.

#### Optoelectronic Devices

Scattering is also important in photoelectronic devices where recombination rates are vital to accurate modeling. As discussed in any introductory semiconductor device

textbook, the recombination rates of electron and holes are composed of several mechanisms – band-to-band, trap-assisted, and Auger recombination [17]. A well-accepted model for these recombination mechanisms is the ABC model [18], [19], [20]. Given the electron and hole densities, this model is typically sufficient but for the details of the A, B, and C coefficients more sophisticated models including the appropriate scattering mechanisms is needed.

## **Biosensing Devices**

Researchers have shown interest in using semiconductors – quantum dots [21] and more recently two-dimensional materials such as single-layer MoS2 [22]. There are two important areas where scattering is vital. The first is the reliability of sensing devices. If these devices are to be used in biological applications it is critical that the devices are reliable under any interactions. Their degree of efficacy could mean life or death. The other important area is the sensitivity of the device. The sensitivity is directly related to the variability and both must be under control.

### **1.2.2 The important of non-local scattering**

Most scattering mechanisms are spatially non-local. Electron scattering on acoustic phonons are often treated as local. The locality of acoustic phonons manifests from approximations made in the derivation of the scattering. Under the assumption of high temperature, equilibrium, bulk phonons with a linear dispersion, acoustic phonons are local. In reality, any of these assumptions can break down and, in general, the scattering is non-local. Similarly non-polar optical phonon scattering is treated as local under the assumption of equilibrium with a flat dispersion. There are other scattering mechanisms that are inherently non-local. One such scattering mechanism that is important, in all materials and devices is roughness. Any variation at an interface can be treated as correlated roughness. Accurate models for the roughness profile have been developed [9], [23], [24]. All of these models include both

the average roughness profile and also the correlation. When a scattering self-energy is used [25] to model the roughness, correlations manifest themselves as non-locality.

A class of scattering mechanisms that are inherently nonlocal are any scattering that includes a Coulombic component. Coulomb potential effects are long-range so any scattering where that effect is included will be non-local. this includes electron-electron, ionized impurity and polar optical phonon scattering. Polar optical phonon scattering is an electron-phonon mechanism that is dominant in polar materials. It originates from a charge dipole plus the addition of optical phonon vibrations [26]. To understand how important the Coulombic potential scattering mechanisms are, the contributions of different scattering mechanisms are shown to the overall mobility for two materials. One is a single layer of Mos2 [27] shown in figure 1.2. The calculated total mobility is compared to experiment. The dominant scattering mechanism, especially at higher temperatures, is the polar optical phonon scattering. The second most dominant is the charged impurity.

The second material is a two-dimensional electron gas of GaAs [28]. As with the single layer of MoS2, the mobility is dominated by the Coulombic scattering mechanisms, polar optical phonon and ionized impurity. To model polar materials, non-local scattering must be included. Additonally, even if the device is non-polar but is doped (i.e. any transistor), the effect of ionized impurity must be included within an accurate model.

### **1.3 Motivation Part II: Towards NEGF in liquid systems**

#### **1.3.1 Modeling molecules in a liquid**

NEGF has already been shown to be excellent for modeling disorder such as roughness [29], alloy disorder [12], or other imperfections. The goal of the second half of the introduction is to motivate the usage of NEGF in a class of problems it was not previously used for. The reasons NEGF is ideal and ready to solve these class of problems will be discussed in future chapters. The first question, that can be asked, is what

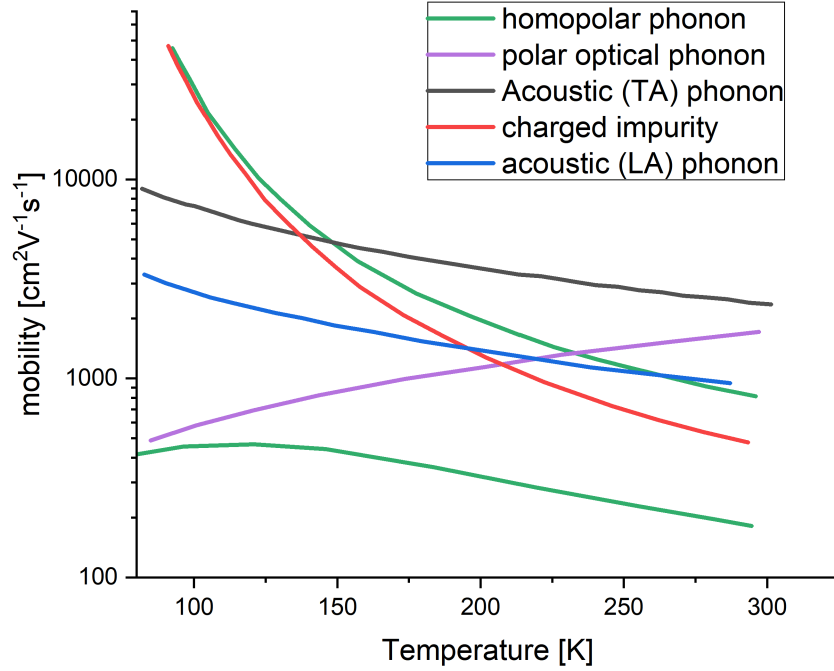


Fig. 1.1. Contribution of different scattering mechanisms to the mobility of a single layer MoS2 device for different temperatures. The data is obtained from [27].

does an NEGF treatment provide that is not already covered by other methods. The short answer is consistent modeling of an open system with a complicated boundary condition. The inclusion of an open system opens up a plethora of possibilities. The possibilities can be broken down into long term and short term components. In the long term, NEGF can model non-equilibrium processes important to chemists such as reactivity. The NEGF method has seen much success in modeling transistors. Transistors are inherently strongly out of equilibrium. The principal component of current flow relies on a non-equilibrium situation whether it be current of differences in Fermi level. In the long term, the modeling of reactivities with the NEGF can help improve the degree of predictive drug design [30]. NEGF can, in principle, handle



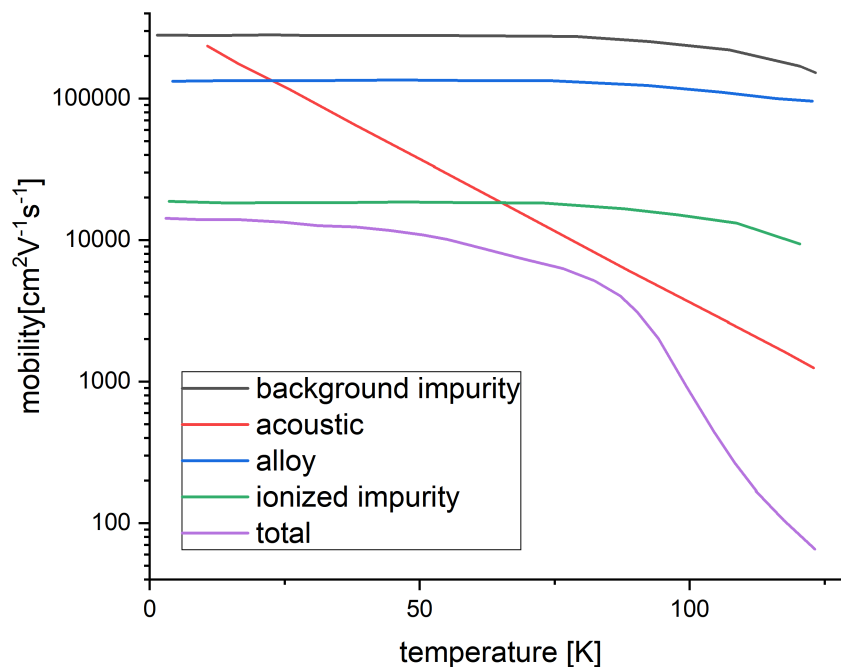


Fig. 1.2. Contribution of different scattering mechanisms to the mobility of a two-dimensional electron gas of GaAs. The data is obtained from [28].

time dependence and thus model the reactivity process fully quantum mechanically in an open system. In the short term and the topic of the second half of this thesis, NEGF can readily handle the question of solubility. Solubility is obviously an important measure when designing a drug or when developing a chemical product. Predicting the degree of solubility allows chemists pre-screening of active ingredient and solvent combinations. Due to the way this work treats the solvent, explicit and quantum-mechanically, the effort used to develop the solubility can be leveraged in order to develop a reactivity model. Snapshots can be taken during the reactivity process and the results can be studied in detail with the new methods.

As will be discussed in future chapters, there are several existing methods for modeling liquid systems. One example is a combination of density functional theory

(DFT) [31], [32] and an implicit solvent treatment [33], [34], [35]. There are many flavors in the details of how to treat the implicit solvent but the main commonality is a continuum electrostatic model for the solvent with a cavity carved out for where the solute would be. This method as the name implies does not treat the solvent explicitly and misses effects such as charge transfer and the repositioning of the solvent atoms due to the presence of the active ingredient. In addition to only modeling the solvent as a continuum, most DFT packages use a  $T = 0\text{K}$  theory and do not handle thermal fluctuations. NEGF, in contrast, includes temperature inherently in its formalism both through the population filling due to Fermi level of the contacts and the thermal fluctuations that can be included with scattering. There are some extensions to DFT for excited state [36] but these are much more expensive and as of this writing are not in most of the popular DFT packages such as VASP [37] and Quantum Espresso [38]. To model the breaking and creating of bonds needed for reactivity, more classical models are typically employed. One such example is Reactive Force Field (ReaxFF) which uses "a general relationship between bond distance and bond order on one hand and between bond order and bond energy on the other hand that leads to proper disassociation of bonds to separated atoms" [39].

## 2. PART I: STATE OF THE ART OF MODELING SCATTERING IN QUANTUM SYSTEMS

The majority of the introduction to NEGF and the algorithms for solving NEGF with local scattering have been published in [40].

The nonequilibrium Green's function theory first introduced by Schwinger (1961) [6], Kadanoff and Baym (1962) [7] and Fujita (1964) [8] has found applications in electronic transport [1], [2], thermal transport [41], [3], and optoelectronics [4], [5]. Scattering can be included in a consistent way as a perturbation [14] [42].

### 2.1 Dyson and Keldysh Equations

Starting from the steady state results of Dyson [43], the equation for the retarded Greens function,  $G^R(\alpha, \beta, E)$  can be written as:

$$[E - H(\alpha, \beta) - q\phi] G^R(\alpha, \beta, E) = \delta(\alpha - \beta) + \int d\gamma \Sigma^R(\alpha, \gamma, E) G^R(\gamma, \beta, E) \quad (2.1)$$

and then written in a more convenient form as :

$$\int d\gamma [E - H(\alpha, \beta) - q\phi - \Sigma^R(\alpha, \gamma, E)] G^R(\gamma, \beta, E) = \delta(\alpha - \beta) \quad (2.2)$$

where  $\alpha$  and  $\beta$  are general coordinates that can correspond to atomic orbitals and position.  $H(\alpha, \beta)$  is the Hamiltonian,  $E$  is the energy of the particle,  $q$  is the electronic charge,  $\phi$  is the electrostatic potential and  $\Sigma^R(\alpha, \beta, E)$  is the retarded self-energy which describes the interactions with the surrounding:

$$\Sigma^R(\alpha, \beta, E) = \Sigma_{lead}^R(\alpha, \beta, E) + \Sigma_{scattering}^R(\alpha, \beta, E) \quad (2.3)$$

Similar to the Dyson's equation, the Keldysh equation of motion [44] for  $G^<(\alpha, \beta, E)$  is:

$$[E - H(\alpha, \beta) - q\phi] G^<(\alpha, \beta, E) = \int d\gamma \Sigma(\alpha, \gamma, E) G^<(\gamma, \beta, E) + \int d\gamma \Sigma^<(\alpha, \gamma, E) G^A(\gamma, \beta, E) \quad (2.4)$$

and

$$\Sigma^<(\alpha, \beta, E) = \Sigma_{lead}^<(\alpha, \beta, E) + \Sigma_{scattering}^<(\alpha, \beta, E) \quad (2.5)$$

Using equation 2.2, the Keldysh equation can be written in a more convenient form:

$$G^<(\alpha, \beta, E) = \int d\alpha' d\beta' G^R(\alpha, \alpha', E) \Sigma^<(\alpha', \beta', E) G^R(\beta', \beta, E) \quad (2.6)$$

In the stationary case, which is utilized throughout this thesis:

$$G^A(\alpha, \beta, E) = [G^R(\alpha, \beta, E)]^\dagger \quad (2.7)$$

Additionally, another relation holds:

$$G^R(\alpha, \beta, E) - G^A(\alpha, \beta, E) = G^>(\alpha, \beta, E) - G^<(\alpha, \beta, E) \quad (2.8)$$

Note that due to this relation, only two of the four Green's function need calculated  $G^R(\alpha, \beta, E)$  and  $G^<(\alpha, \beta, E)$ . The other Green's function when needed can be calculated from equation 2.8.

Thus equations 2.2- 2.8 form coupled integro-differential equations. The scattering self-energies  $\Sigma_{scattering}^{R/<}(\alpha, \beta, E)$  depend on the Green's functions  $G^{R/<}(\alpha, \beta, E)$  These equations must be solved iteratively, and their solution will be discussed in the next section.

## 2.2 Local Electron-Phonon Scattering Self-energies

As mentioned in the previous section, the NEGF equations are coupled and must be solved iteratively. This iterative solution is the perturbation expansion of Feynmann diagrams describing the interaction of electrons and phonons [45] and is called

the self-consistent Born approximation. The most general expressions for the scattering self-energies are:

$$\Sigma_{scattering}^< = \int \frac{dE'}{2\pi} D^<(E') G^<(E - E') \quad (2.9)$$

$$\begin{aligned} \Sigma_{scattering}^R(E) = & \int \frac{dE'}{2\pi} \left[ D^R(E') G^R(E - E') + D^<(E') G^R(E - E') \right] \\ & + \int \frac{dE'}{2\pi} \left[ D^R(E') G^<(E - E') \right] \end{aligned} \quad (2.10)$$

Where  $D^{</R}$  is the phonon's Green function and  $G^{</R}$  is the electron's Green function.

A solution of these general expressions depend on a coupled transport solution of electrons and phonons. As is common in literature, e.g. ref. [45] and [46], the phonons will be assumed to be bulk and isotropic with equilibrium occupation described with the Bose distribution,  $n_q$ . Under the assumption of bulk the phonon lesser Green's function is written as

$$D^< = n_q (D^R - D^A) \quad (2.11)$$

Additionally from ref. [46],

$$\int \frac{dE'}{2\pi} G^R(E - E') D^R(E') = -i [G^R(E - \hbar\omega_q) - G^R(E + \hbar\omega_q)] \quad (2.12)$$

The retarded scattering self-energy  $\Sigma^R(\alpha, \beta, E)$  with these approximations and relations can be written as:

$$\begin{aligned} \Sigma^R(\alpha, \beta, E) = & \frac{1}{(2\pi)^3} \int d\vec{q} |U_q|^2 e^{i\vec{q} \cdot (\vec{x}_\alpha - \vec{x}_\beta)} [n_q G^R(\alpha, \beta, E - \hbar\omega_q) \\ & + (1 + n_q) G^R(\alpha, \beta, E + \hbar\omega_q) \\ & + \frac{1}{2} G^<(E - \hbar\omega_q) - \frac{1}{2} G^<(E + \hbar\omega_q) \\ & + i \int \frac{dE'}{\pi} G^<(E - E') \times \left( Pr \left\{ \frac{1}{E' - \hbar\omega_q} \right\} - Pr \left\{ \frac{1}{E' + \hbar\omega_q} \right\} \right) \end{aligned} \quad (2.13)$$

Also, the lesser scattering self-energy  $\Sigma^<_{\alpha,\beta,E}$  with these approximations and relations can be written as:

$$\Sigma^<(\alpha, \beta, E) = \frac{1}{(2\pi)^3} \int d\vec{q} |U_q|^2 e^{i\vec{q} \cdot (\vec{x}_\alpha - \vec{x}_\beta)} \quad (2.14)$$

$$\times [n_q G^<(\alpha, \beta, E - \hbar\omega_q) + (1 + n_q) G^<(\alpha, \beta, E + \hbar\omega_q)] \quad (2.15)$$

where  $q$  is the phonon wavevector,  $\omega_q$  is the phonon frequency,  $n_q$  is the Bose distribution,  $|U_q|$  is the electron-phonon perturbing potential,  $\vec{x}_\alpha$  and  $\vec{x}_\beta$  are the positions of the general coordinates  $\alpha$  and  $\beta$ , respectively.

With this general equation 2.15, the scattering self-energy for any phonon dispersion can in principle be solved under the assumptions discussed above. There are two main issues with this general equation. One issue is how to determine  $U_q$ .  $U_q$  is dependent on how the lattice affects the electron.

## Deformation Potential Theory

A well-recognized and understood theory is the deformation potential theory pioneered by Bardeen and Shockley [47]. This theory has found success in a wide range of semiconductors. The idea is that the perturbing Hamiltonian is in general a complicated expression of the position of the electron and of the lattice ion position. However for the long wavelength phonons, the change in, conduction band,  $E_c$  is proportional to strain i.e. displacement. In the next several sections, the derivation of different scattering mechanisms will be outlined.

## Local Deformation Potential Scattering Self-energy for Acoustic Phonons

For acoustic phonons, the perturbing potential is proportional to the strain of the phonons [48]. For the plane wave phonons discussed in the previous section:

$$H_{el-acoustic}(\vec{r}, t) = D_{ac} \nabla_{\vec{r}} u(\vec{r}, t) \quad (2.16)$$

where

$$u(\vec{r}, t) = A_q e^{i(\vec{q} \cdot \vec{r} - \omega_q t)} + A_q^\dagger e^{-i(\vec{q} \cdot \vec{r} - \omega_q t)} \quad (2.17)$$

$A_q$  is the phonon amplitude. In order to use these results, the displacement is Fourier transformed and the absolute value is squared. The result following [29] is

$$|H_{el-acoustic}(\vec{q})|^2 = \frac{\hbar D_{ac}^2}{2\rho\omega_q} q^2 \quad (2.18)$$

$\omega_q$  is the frequency for the  $q$  wavevector. Assuming long wavelength ( $|q| \rightarrow 0$ ), the phonon dispersion for the longitudinal acoustic (LA) branch can be approximated with a linear dispersion. The slope is determined by the longitudinal sound velocity.

$$\omega_q \approx v_s q \quad (2.19)$$

Additionally, the Bose distribution is approximated with the high temperature (equipartition) approximation. At high temperatures, the Bose distribution is expanded in a Taylor expansion and the result is

$$N_q \approx N_q + 1 \approx \frac{k_b T}{\hbar\omega_q} = \frac{k_b T}{\hbar v_s q} \quad (2.20)$$

Finally, the acoustic phonon is considered elastic. Note that with the elastic approximation 2.10 now only depends on the retarded Green's function and the principal value disappears. With this additional approximation and using equation 2.18 as  $|U_q|^2$

$$\Sigma^{</R}(\alpha, \beta, E) = \frac{k_b T D_{ac}^2}{\rho v_s^2} \int \frac{d\vec{q}}{(2\pi)^3} e^{i\vec{q} \cdot (\vec{x}_\alpha - \vec{x}_\beta)} G^{</R}(\alpha, \beta, E) \quad (2.21)$$

Performing the integration over  $\vec{q}$ , the self-energy now reads:

$$\Sigma^{</R}(\alpha, \beta, E) = \frac{k_b T D_{ac}^2}{\rho v_s^2} \delta(\vec{x}_\alpha - \vec{x}_\beta) G^{</R}(\alpha, \beta, E) \quad (2.22)$$

For the rest of this thesis, the elastic acoustic scattering self-energy will be approximated as diagonal:

$$\Sigma^{</R}(\alpha, \beta, E) = \frac{k_b T D_{ac}^2}{\rho v_s^2} \delta_{\alpha, \beta} G^{</R}(\alpha, \beta, E) \quad (2.23)$$

## Other Approximations for Deformation Potential Scattering Self-energy for Acoustic Phonons

Most of the thesis will include elastic acoustic phonons, but there are other approximations that have been used to include inelastic effects due to the acoustic phonons. One approach in reference [29], is to take the average over the Green's functions. The average is taken over a Debye energy. This is the maximum energy in which the Debye (linear) approximation still holds. This is a modification of equation 2.23:

$$G^{</R}(\alpha, \beta, E) \rightarrow \frac{1}{2E_D} \int_{E-E_D}^{E+E_D} dE' G^{</R}(\alpha, \beta, E') \quad (2.24)$$

The effect of this modification is that there is continuous energy dissipation around a Debye energy,  $E_D$ .

## Local Deformation Potential Scattering Self-energy for Nonpolar Optical Phonons

For optical phonons, the perturbing potential is proportional to the displacement

$$H_{el-optical}(\vec{r}, t) = D_{op} u(\vec{r}, t) \quad (2.25)$$

where

$$u(\vec{r}, t) = A_q e^{i(\vec{q} \cdot \vec{r} - \omega_q t)} + A_q^\dagger e^{-i(\vec{q} \cdot \vec{r} - \omega_q t)} \quad (2.26)$$

In the derivation the following is assumed: long wavelength ( $|q| \rightarrow 0$ ), isotropic phonon bandstructure, and that the longitudinal optical (LO) phonon branch is flat and  $\omega_q \approx \omega_0$ , the perturbing potential can be solved analytically. Thus, the Bose distribution is also a constant and can be taken out of the integral over  $q$ . Similar to the acoustic optical case, equation 2.25 can be Fourier transformed, squared and taken the magnitude and the result after applying the aforementioned approximations [29] is

$$|H_{el-optical}(\vec{q})|^2 = D_{op}^2 \frac{\hbar}{2\rho\omega_0} \quad (2.27)$$



Note that the dependence on  $q$  is removed with the assumption that the LO phonon has a constant frequency equal to  $\omega_0$ . In this case, the high temperature approximation cannot be taken and emission and absorption processes must be considered separately. Thus, the lesser scattering self-energy is written as

$$\begin{aligned} \Sigma^<(\alpha, \beta, E) &= \frac{\hbar D_{op}^2 k_B T}{2\rho\omega_0} \delta_{\alpha, \beta} \\ &\times [n_0 G^<(\alpha, \beta, E - \hbar\omega_0)) + (1 + n_0) G^<(\alpha, \beta, E + \hbar\omega_0)] \end{aligned} \quad (2.28)$$

And the retarded self-energy

$$\begin{aligned} \Sigma^R(\alpha, \beta, E) &= \frac{\hbar D_{op}^2 k_B T}{2\rho\omega_0} \delta_{\alpha, \beta} \\ &\times [(1 + n_0) G^R(\alpha, \beta, E - \hbar\omega_0) + n_0 G^R(\alpha, \beta, E + \hbar\omega_0) \\ &\quad + \frac{1}{2} G^<(\alpha, \beta, E - \hbar\omega_0) - \frac{1}{2} G^<(\alpha, \beta, E + \hbar\omega_0)] \\ &+ iP \int \frac{dE'}{2\pi} \left[ \frac{G^<(\alpha, \beta, E - E')}{E' - \hbar\omega_0} - \frac{G^<(\alpha, \beta, E - E')}{E' + \hbar\omega_0} \right] \end{aligned} \quad (2.29)$$

Note that the principal value integral in equation 2.29 can be safely ignored as discussed in reference [13]. Another approach common in literature is to write

$$\begin{aligned} \Sigma^R(\alpha, \beta, E) &= \frac{1}{2} (\Sigma^>(\alpha, \beta, E) - \Sigma^<(\alpha, \beta, E)) \\ &\quad + iP \int \frac{dE'}{2\pi} \times \left[ \frac{\Sigma^>(\alpha, \beta, E') - \Sigma^<(\alpha, \beta, E')}{E - E'} \right] \end{aligned} \quad (2.30)$$

and to neglect the principal value integral [49]. However, this approximation will underestimate the  $I_{\text{off}}$  current in MOSFETs [13].

## Nonlocal Scattering Self-energy for Polar Optical Phonons

The scattering self-energy for polar optical phonons has a momentum dependent prefactor. This means that for different geometries (nanowire, ultra-thin body and quasi-1D) the scattering self-energy has a different shape. The equations for the

scattering self-energies are written here for completeness. Their derivations were done in [50].

### 1. Scattering self-energies for nanowires

for  $\vec{x}_3 \neq \vec{x}_4$

$$\begin{aligned}
& \Sigma^<(\vec{x}_3, \vec{x}_4, E) \\
&= \frac{e^2 e^{-|\vec{x}_3 - \vec{x}_4|/\xi}}{8\pi} \frac{E_0}{2\varepsilon_0} \left( \frac{2}{|\vec{x}_3 - \vec{x}_4|} - \frac{1}{\xi} \right) \left( \frac{1}{\varepsilon_\infty} - \frac{1}{\varepsilon_s} \right) \\
&\quad \times [n_0 G^<(\vec{x}_3, \vec{x}_4, E - E_0) + (1 + n_0) G^<(\vec{x}_3, \vec{x}_4, E + E_0)], \\
& \\
& \Sigma^R(\vec{x}_3, \vec{x}_4, E) \\
&= \frac{e^2 e^{-|\vec{x}_3 - \vec{x}_4|/\xi}}{8\pi} \frac{E_0}{2\varepsilon_0} \left( \frac{2}{|\vec{x}_3 - \vec{x}_4|} - \frac{1}{\xi} \right) \left( \frac{1}{\varepsilon_\infty} - \frac{1}{\varepsilon_s} \right) \\
&\quad \times [(1 + n_0) G^R(\vec{x}_3, \vec{x}_4, E - E_0) + n_0 G^R(\vec{x}_3, \vec{x}_4, E + E_0) \\
&\quad + \frac{1}{2} G^<(\vec{x}_3, \vec{x}_4, E - E_0) - \frac{1}{2} G^<(\vec{x}_3, \vec{x}_4, E + E_0) \\
&\quad + i \int \frac{d\tilde{E}}{2\pi} G^<(\vec{x}_3, \vec{x}_4, \tilde{E}) \left( \text{Pr} \frac{1}{E - \tilde{E} - E_0} - \text{Pr} \frac{1}{E - \tilde{E} + E_0} \right)] \quad (2.31)
\end{aligned}$$

and for the case  $\vec{x}_3 = \vec{x}_4$

$$\begin{aligned}
& \Sigma^<(\vec{x}_3, \vec{x}_3, E) \\
&= \frac{e^2 E_0}{2\varepsilon_0 (2\pi)^3} \left( \frac{1}{\varepsilon_\infty} - \frac{1}{\varepsilon_s} \right) \left( \frac{6\pi^2}{a} - \frac{6\pi}{\xi} \arctan(\pi\xi/a) - \frac{2\xi^2\pi^4}{a(\pi^2\xi^2 + a^2)} \right) \\
&\quad \times [n_0 G^<(\vec{x}_3, \vec{x}_3, E - E_0) + (1 + n_0) G^<(\vec{x}_3, \vec{x}_3, E + E_0)], \quad (2.32)
\end{aligned}$$

$$\begin{aligned}
& \Sigma^R(\vec{x}_3, \vec{x}_3, E) \\
&= \frac{e^2 E_0}{2\varepsilon_0 (2\pi)^3} \left( \frac{1}{\varepsilon_\infty} - \frac{1}{\varepsilon_s} \right) \left( \frac{6\pi^2}{a} - \frac{6\pi}{\xi} \arctan(\pi\xi/a) - \frac{2\xi^2\pi^4}{a(\pi^2\xi^2 + a^2)} \right) \\
&\quad \times [(1 + n_0) G^R(\vec{x}_3, \vec{x}_3, E - E_0) + n_0 G^R(\vec{x}_3, \vec{x}_3, E + E_0) \\
&\quad + \frac{1}{2} G^<(\vec{x}_3, \vec{x}_3, E - E_0) - \frac{1}{2} G^<(\vec{x}_3, \vec{x}_3, E + E_0) \\
&\quad + i \int \frac{d\tilde{E}}{2\pi} G^<(\vec{x}_3, \vec{x}_3, \tilde{E}) \left( \text{Pr} \frac{1}{E - \tilde{E} - E_0} - \text{Pr} \frac{1}{E - \tilde{E} + E_0} \right)] \quad (2.33)
\end{aligned}$$

## 2. Scattering self-energies for ultra-thin bodies

$$\begin{aligned}
& \Sigma^<(\vec{x}_{\parallel,3}, \vec{x}_{\parallel,4}, k, E) \\
&= \frac{e^2}{(2\pi)^3} \left( \frac{1}{\varepsilon_\infty} - \frac{1}{\varepsilon_s} \right) \frac{E_0}{2\varepsilon_0} \int_0^\infty dq_{\parallel} \int_0^{2\pi} d\theta \\
&\quad \times \int dl \frac{q_{\parallel} \left( q_{\parallel}^2 + (k-l)^2 \right) \exp(iq_{\parallel} |\vec{x}_{\parallel,3} - \vec{x}_{\parallel,4}| \cos \theta)}{\left( q_{\parallel}^2 + (k-l)^2 + \xi^{-2} \right)^2} \\
&\quad \times [n_0 G^<(\vec{x}_{\parallel,3}, \vec{x}_{\parallel,4}, l, E - E_0) + (1 + n_0) G^<(\vec{x}_{\parallel,3}, \vec{x}_{\parallel,4}, l, E + E_0)] \\
&= \frac{e^2}{(2\pi)^3} \left( \frac{1}{\varepsilon_\infty} - \frac{1}{\varepsilon_s} \right) \frac{E_0}{2\varepsilon_0} \int dl F(|\vec{x}_{\parallel,3} - \vec{x}_{\parallel,4}|, |k-l|, \xi) \\
&\quad \times [n_0 G^<(\vec{x}_{\parallel,3}, \vec{x}_{\parallel,4}, l, E - E_0) + (1 + n_0) G^<(\vec{x}_{\parallel,3}, \vec{x}_{\parallel,4}, l, E + E_0)] \quad (2.34)
\end{aligned}$$

with

$$\begin{aligned}
& F(r, q, \xi) \\
&= \frac{\xi \pi}{[q^2 \xi^2 + 1]^{3/2} |r|^3} \left[ 8\xi^2 G\left([1/2, ], [[3/2, 3/2], [3/2]], \frac{1}{4\xi^2} |r|^2 [q^2 \xi^2 + 1]\right) \right. \\
&\quad \left. + |r|^4 q^4 \xi^2 K_1\left(\frac{|r|}{\xi} \sqrt{q^2 \xi^2 + 1}\right) + |r|^4 (k-l)^2 K_1\left(\frac{|r|}{\xi} \sqrt{q^2 \xi^2 + 1}\right) \right] \quad (2.35)
\end{aligned}$$

the Meijer G function

$$G([1/2, ], [[3/2, 3/2], [3/2]], z) = \frac{1}{2\pi i} \oint_L \frac{\Gamma(0.5 + y) \Gamma(1.5 - y)^2}{\Gamma(-0.5 + y)} z^y dy \quad (2.36)$$

and the modified Bessel function of second kind and first order  $K_1$ . Similarly, we get for the retarded self-energy

$$\begin{aligned}
& \Sigma^R(\vec{x}_{\parallel,3}, \vec{x}_{\parallel,4}, k, E) \\
&= \frac{e^2}{(2\pi)^3} \left( \frac{1}{\varepsilon_\infty} - \frac{1}{\varepsilon_s} \right) \frac{E_0}{2\varepsilon_0} \int dl F(|\vec{x}_{\parallel,3} - \vec{x}_{\parallel,4}|, k-l, \xi) \\
&\quad \times [(1 + n_0) G^R(\vec{x}_{\parallel,3}, \vec{x}_{\parallel,4}, l, E - E_0) + n_0 G^R(\vec{x}_{\parallel,3}, \vec{x}_{\parallel,4}, l, E + E_0) \\
&\quad + \frac{1}{2} G^<(\vec{x}_{\parallel,3}, \vec{x}_{\parallel,4}, l, E - E_0) - \frac{1}{2} G^<(\vec{x}_{\parallel,3}, \vec{x}_{\parallel,4}, l, E + E_0) \\
&\quad + i \int \frac{d\tilde{E}}{2\pi} G^<(\vec{x}_{\parallel,3}, \vec{x}_{\parallel,4}, l, \tilde{E}) \left( \text{Pr} \frac{1}{E - \tilde{E} - E_0} - \text{Pr} \frac{1}{E - \tilde{E} + E_0} \right)] \quad (2.37)
\end{aligned}$$

### 3. Scattering self-energies for quasi-1D

$$\begin{aligned}
& \Sigma^< (z_3, z_4, k_{\parallel}, E) \\
&= \frac{\gamma\pi}{(2\pi)^3} \int d\vec{l}_{\parallel} \frac{e^{-\sqrt{q_{\parallel}^2 + \xi^{-2}}|z_3 - z_4|}}{\sqrt{q_{\parallel}^2 + \xi^{-2}}} \left( 1 - \frac{\xi^{-2}|z_3 - z_4|}{2\sqrt{q_{\parallel}^2 + \xi^{-2}}} - \frac{\xi^{-2}}{2(q_{\parallel}^2 + \xi^{-2})} \right) \\
& \quad [n_0 G^< (z_3, z_4, l_{\parallel}, E - E_0) + (1 + n_0) G^< (z_3, z_4, l_{\parallel}, E + E_0)] . \quad (2.38)
\end{aligned}$$

$$\begin{aligned}
& \Sigma^R (z_3, z_4, k_{\parallel}, E) \\
&= \frac{\gamma\pi}{(2\pi)^3} \int d\vec{l}_{\parallel} \frac{e^{-\sqrt{q_{\parallel}^2 + \xi^{-2}}|z_3 - z_4|}}{\sqrt{q_{\parallel}^2 + \xi^{-2}}} \left( 1 - \frac{\xi^{-2}|z_3 - z_4|}{2\sqrt{q_{\parallel}^2 + \xi^{-2}}} - \frac{\xi^{-2}}{2(q_{\parallel}^2 + \xi^{-2})} \right) \\
& \quad \times [(1 + n_0) G^R (z_3, z_4, l_{\parallel}, E - E_0) + n_0 G^R (z_3, z_4, l_{\parallel}, E + E_0) \\
& \quad + \frac{1}{2} G^< (z_3, z_4, l_{\parallel}, E - E_0) - \frac{1}{2} G^< (z_3, z_4, l_{\parallel}, E + E_0) \\
& \quad + i \int \frac{d\tilde{E}}{2\pi} G^< (z_3, z_4, l_{\parallel}, \tilde{E}) \left( \text{Pr} \frac{1}{E - \tilde{E} - E_0} - \text{Pr} \frac{1}{E - \tilde{E} + E_0} \right)] . \quad (2.39)
\end{aligned}$$

Note that  $q_{\parallel}$  is depending on the electronic momenta

$$q_{\parallel} = \sqrt{k_{\parallel}^2 + l_{\parallel}^2 - 2k_{\parallel}l_{\parallel} \cos \theta},$$

with  $\theta$  the angle between  $\vec{k}_{\parallel}$  and  $\vec{l}_{\parallel}$  which is part of the 2D integral of the last equations.

#### 2.2.1 Electron Density and Current

Once the Green's functions are solved, the observables such as density and current can be calculated. For density:

$$\begin{aligned}
n(\vec{x}) &= \int n(\vec{x}, E) dE \\
&= \frac{1}{2\pi} \int \Im \{ \text{diag} [\text{trace} (G^< (\alpha, \beta, E))] \} dE \quad (2.40)
\end{aligned}$$

where the trace is over orbitals.

The current between layers  $i$  and  $i+1$  is calculated as:

$$J_{i \rightarrow i+1}(E) = \frac{q}{\hbar} \int \frac{dE}{2\pi} \times 2\Re \left\{ \text{trace} \left[ H_{i,i+1} G_{i+1,i}^<(E) \right] \right\} \quad (2.41)$$

Where the trace is over all orbitals and atoms in the layer  $i$ .  $G_{i+1,i}^<(E)$  is the off-diagonal block of the lesser Green's function corresponding to the coupling of  $i$  and  $i+1$ . For convergence of the iterative solutions of Green's functions, self-energies and Poisson potential, the spatial variation of local current and the variation of local charge between iterations serve as convergence measures.

### 2.2.2 Algorithm Flow

Since the different components of the NEGF equations have been developed in the previous sections, the overall program flow is shown in figure 2.1. The scattering self-energies and the Green's functions are solved self-consistently until convergence. This self-consistent approach preserves conservation laws and is used throughout this work [45]. All previously-mentioned self-energy approximations conserve current if the iterations of Green's functions and self-energies are converged.

## 2.3 How to solve the Keldysh and Dyson Equations?

As can be seen in equation 2.2, the solution of the Dyson equation involves an inversion. There are two accepted methods for solving the inversion. The first is to fully invert the matrices. This has the advantage of including all nonlocal information since all matrix elements are solved. However, the complexity of the inversion is  $O(n^3)$  in both time and memory. To give a concrete example, we can look at the memory needed for a InAs nanowire. For a given device of a circular nanowire with diameter 2nm and a length of 25nm, the number of atoms are about 5500. In a

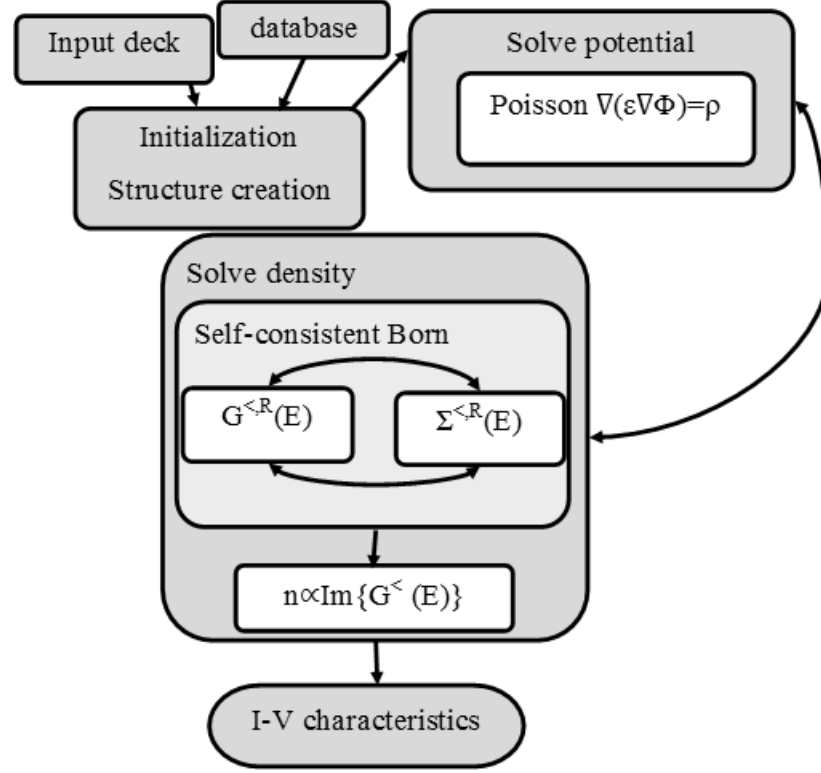


Fig. 2.1. Overview of the Poisson and Self-consistent Born approximation iterative approach used

10 band  $sp^3d^5s^*$  basis, the memory required is about 50 GB. To include spin-orbit coupling, an important effect in III-V devices, the memory required quadruples to about 200 GB. This is not feasible on today's machines. The other method is A highly successful algorithm for the solution of the inversion of the diagonal is described in reference [51]. This so-called recursive Green's function will be outlined in the next section. However, since it only inverts the diagonal, only local scattering is possible. The memory required for the 10 band  $sp^3d^5s^*$  is 0.3 GB and with spin orbit coupling is 1.2 GB. However, as discussed above most scattering is non-local and this recursive algorithm is not compatible with non-local scattering. Details of the local recursive Green's function algorithm is given in the next section

### 2.3.1 Traditional Recursive Green's Function Algorithm

The recursive Green's function (RGF) is an efficient algorithm for calculating the necessary elements of the Green's function in order to calculate the density and current. RGF divides the device into layers and employs two main steps. The first step is the "forward" step in which the one-sided Dyson's and Keldysh equation are solved for  $g_R$  and  $g_L$ , respectively. It is called one-sided because the left contact (if going from left to right of the device) surface Green's function is used and the Green's function are recursively calculated moving toward the right contact. When the iterations reach the right contact, the surface Green's function of the right contact is used to solve the next step of the recursive algorithm. The second step is the "backward" step in which the exact Green's functions are calculated after connecting the one-sided Green's functions to the right contact and iterating back towards the left contact. An overview of the algorithm is shown in 2.2.

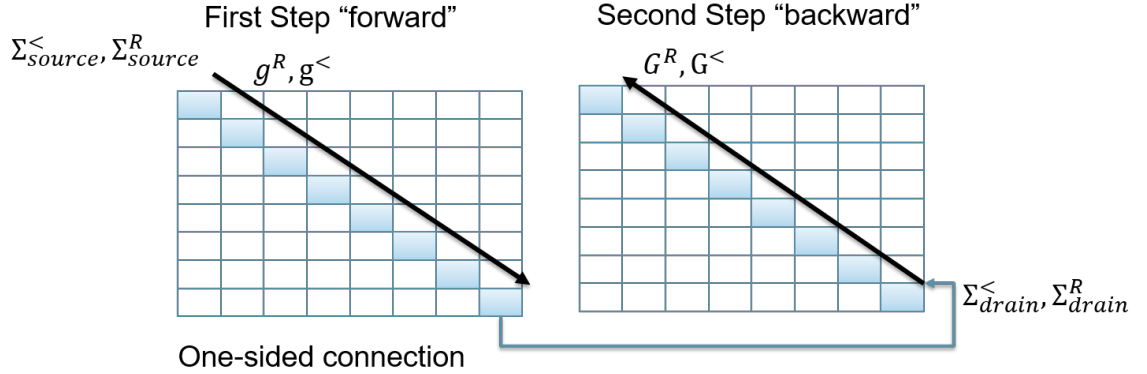


Fig. 2.2. Recursive Green's function Algorithm Overview

### Block Tri-Diagonal Formalism

Following reference [52], the algorithm for calculating  $G^R(E)$  can be written in block matrix notation (dropping the energy dependence for clarity and using  $i$  as the

layer index) as follows. Defining  $A_{i,i} = (E - H - \Sigma_{i,i}^R)^{-1}$  for convenience.  $H_{i,i+1}$  is the coupling Hamiltonian between layer  $i$  and layer  $i + 1$ . For the "forward" step  $g^R$ : The first layer is :

$$g_{1,1}^R = (A_{1,1})^{-1} \quad (2.42)$$

The next layers

$$g_{i,i}^R = (A_{i,i} + H_{i,i-1}g_{i-1,i}^R H_{i-1,i})^{-1} \quad (2.43)$$

Once the forward iterations are completed. The last layer  $G_{N,N}^R$  where  $N$  is the total number of layers is

$$G_{N,N}^R = g_{N,N}^R \quad (2.44)$$

The next  $N - 1$  to 1 layers "backward" steps for  $G^R$  are:

$$G_{i,i}^R = g_{i,i}^R + g_{i,i}^R (H_{i,i+1}G_{i+1,i+1}^R H_{i+1,i}) g_{i,i}^R \quad (2.45)$$

The sub-diagonal and super-diagonal block of  $G^R$  can also be calculated for later use in  $G^<$  calculation.

$$G_{i+1,i}^R = -G_{i+1,i+1}^R H_{i+1,i} g_{i,i}^R \quad (2.46)$$

$$G_{i,i+1}^R = -g_{i,i}^R H_{i,i+1} G_{i+1,i+1}^R \quad (2.47)$$

Similarly,  $G^<$  can also be calculated recursively. For the "forward" step  $g^<$ : The first layer is :

$$g_{1,1}^< = g_{1,1}^R \Sigma_{1,1}^< g_{1,1}^A \quad (2.48)$$

The next layers

$$\begin{aligned} g_{i,i}^< = g_{i,i}^R & \left[ \Sigma_{i,i}^< + A_{i,i-1} g_{i-1,i-1}^< A_{i-1,i}^\dagger + \Sigma_{i,i-1}^< g_{i-1,i-1}^A A_{i-1,i}^\dagger \right. \\ & \left. + A_{i,i-1} g_{i-1,i-1}^R \Sigma_{i-1,i}^< \right] g_{i,i}^A \end{aligned} \quad (2.49)$$

Once the forward iterations are completed. The last layer  $G_{N,N}^<$  where  $N$  is the total number of layers is

$$G_{N,N}^< = g_{N,N}^< \quad (2.50)$$



The next  $N - 1$  to 1 layers "backward" steps for  $G^<$  are:

$$\begin{aligned}
 G_{i,i}^< &= g_{i,i}^< + g_{i,i}^< A_{i,i+1}^\dagger G_{i+1,i}^A + g_{i,i}^R \Sigma_{i,i+1}^< g_{i+1,i+1}^A A_{i+1,i}^\dagger G_{i,i}^A \\
 &+ g_{i,i}^R A_{i,i+1} G_{i+1,i}^<
 \end{aligned} \tag{2.51}$$

The sub-diagonal and super-diagonal block of  $G^<$  can also be calculated if needed.

$$\begin{aligned}
 G_{i+1,i}^< &= g_{i+1,i}^R \Sigma_{i+1,i}^< g_{i,i}^A + G_{i+1,i}^R A_{i,i+1} g_{i+1,i}^R \Sigma_{i+1,i}^< g_{i,i}^A \\
 &+ G_{i+1,i+1}^R A_{i+1,i} g_{i,i}^< + G_{i,i+1}^A A_{i,i+1}^\dagger g_{i,i}^A
 \end{aligned} \tag{2.52}$$

### 3. LOCAL SCATTERING RESULTS

#### 3.1 Silicon TFET

The majority of the results and discussion here have been published in [16]. As discussed in the previous chapter, the efficient solution of the Green's functions using the recursive algorithm only allows calculation of local scattering. For this reason, the first application was a silicon TFET in which the dominant electron-phonon scattering mechanisms are acoustic phonon and non-polar optical phonon.

The transfer characteristics of this device is shown in figure 3.2. Compared to the pure coherent transport (i.e. ballistic), the current of a scattered transport calculation is higher for all gate voltages. This is due to the phonon-assisted tunneling that plays a major role in TFET devices. The Ion current for the scattered case is 0.459 nA compared 0.099 nA when treated ballistically. Except for the lowest simulated gate voltage,  $V_{gs} = 0.0V$ , the ratio of scattered to ballistic current increases monotonically with the gate voltage. This behavior is due a better alignment of the valence band and conduction band and a higher tunneling probability. When scattering is included the SS is improved from 139.5 mV/dec to 113.7 mV/dec. Figure 3.2 compares scattered transport results with self-energies following Eqs. (2.13-2.14) and with self-energies of only the imaginary part of Eqs. (2.13-2.14). The effect of using only the imaginary part of Eqs. (2.13-2.14) is an underestimation of the scattering assisted tunneling - especially at lower  $V_{gs}$ . In the same way, the SS gets overestimated with this approximation the SS is 113.7 mV/dec; with the imaginary part of the equations in question it is 120.53 mV/dec). To further illustrate, the effect that scattering has on the tunneling the DOS is shown in figure 3.3. The DOS of a scattered NEGF calculation is shifted to lower energies and spread out further than the ballistic results. This increase of the band tail due to scattering increases the tunneling current.

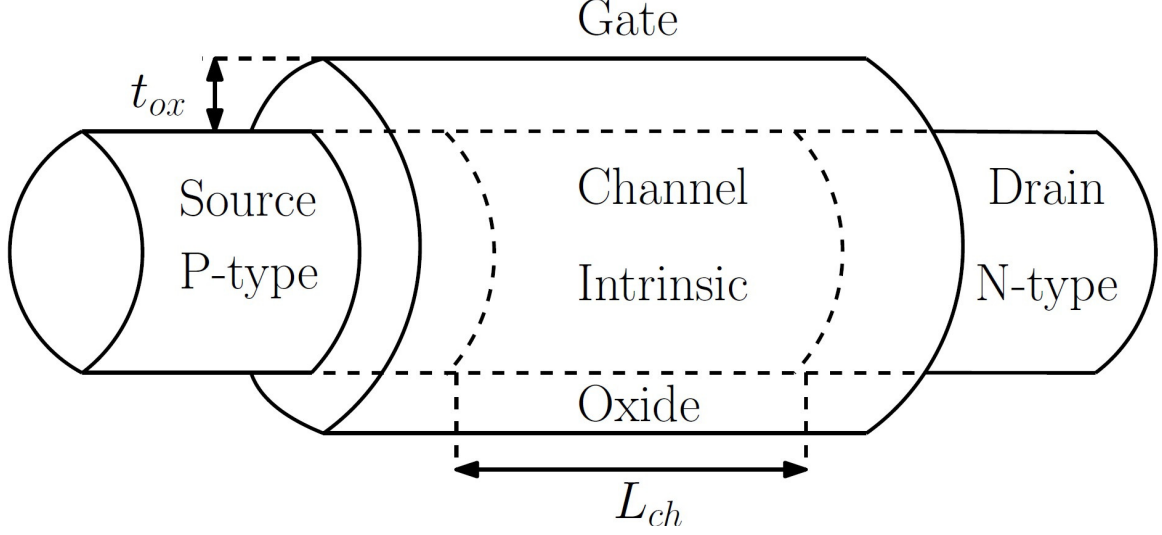


Fig. 3.1. Schematic of a PIN circular nanowire TFET that is simulated.

### 3.2 Resonance TFET

A resonance TFET was simulated with non-polar optical phonon scattering with scattering strengths from 0-220 eV/nm. The device considered is in fig. 3.4. Both acoustic and non-polar optical phonon is considered. The ballistic case is also shown for comparison. Optical C is used the Silicon non-polar deformation constant value of 110 eV/nm. Optical B is approximately two times this value and Optical A is four times optical C. As can be seen in figure 3.5, ballistic gives the lowest subthreshold slope and highest on-current. As the scattering strength is increased, the subthreshold slope increases. Scattering increases the tunneling current due to phonon-assisted tunneling increases. The device starts to turn at lower voltages. The cut-off for the off-current is not as abrupt and the result is the subthreshold slope increases. When the device is completely on, the scattering reduction, similar to traditional MOSFETS, can be seen. The resonance TFET performance is strongly dependent on scattering and an accurate model is necessary for proper performance comparisons.

In order to quantify the effect of scattering on the subthreshold slope, the subthreshold slope for the different configurations are compared in figure 3.6

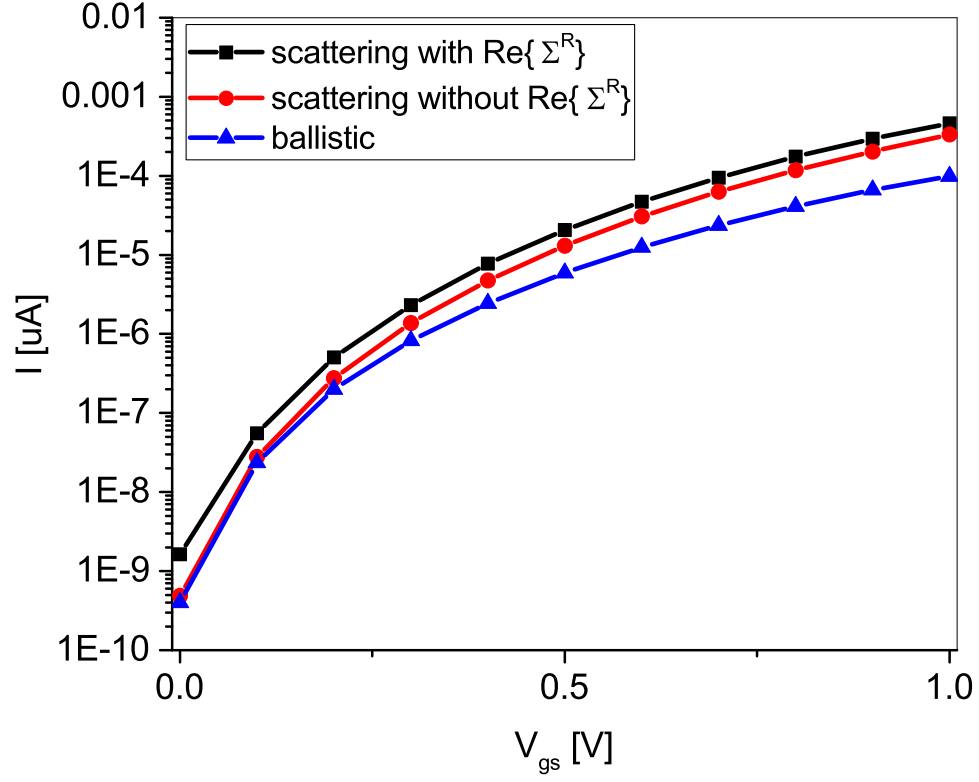


Fig. 3.2. Comparison of scattered to ballistic transfer characteristics for a 3nm circular nanowire TFET with a  $V_{ds} = 1.0\text{V}$ . Two scattered cases are shown. With and without energy renormalization. Including energy renormalization increases the phonon-assisted tunneling and thus increases current.

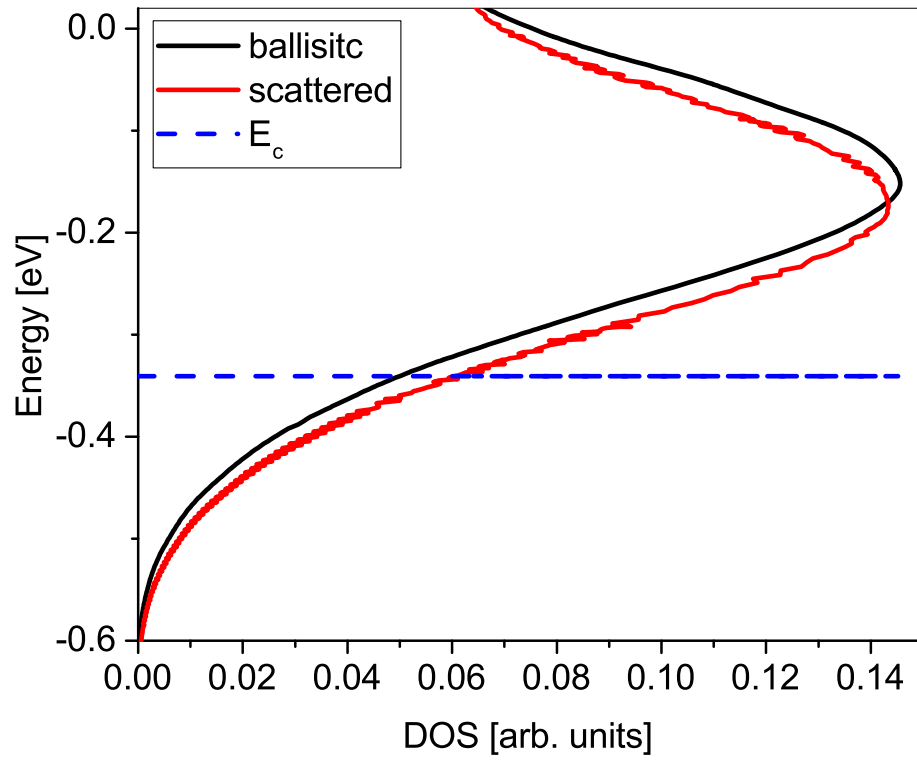


Fig. 3.3. Comparison of scattered to ballistic DOS near the transition region at  $x = 8$  nm for the IV in figure 5 at  $V_{gs} = 0.6$  V. The energy shift between scattered and ballistic is about 16 meV.

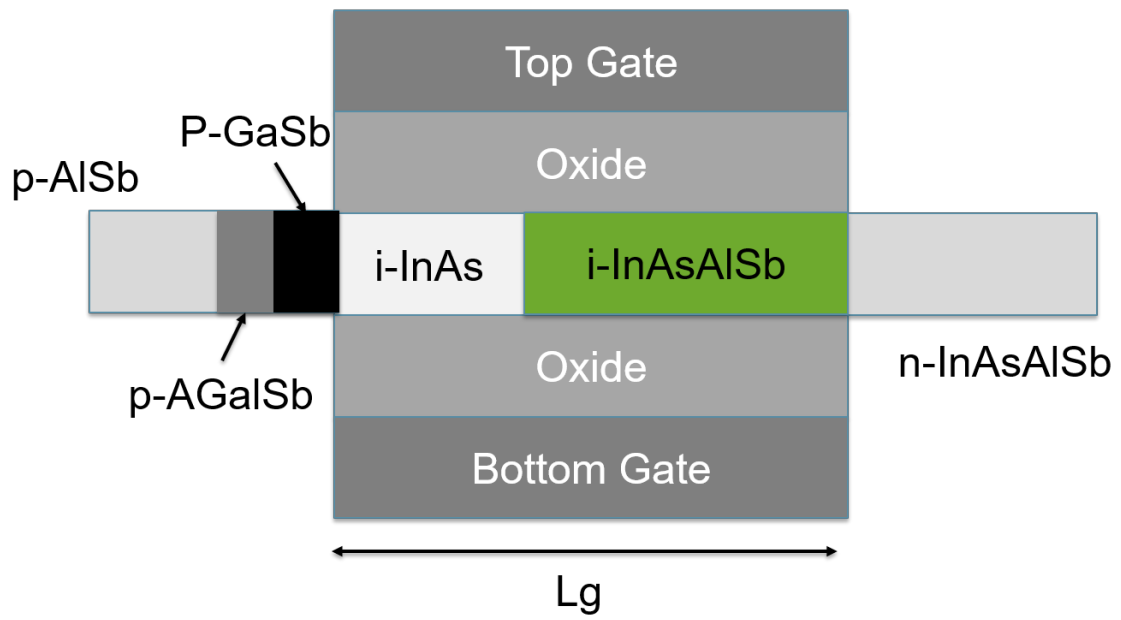


Fig. 3.4. Cross-sectional schematics of a triple-HJ TFET. Schematic design obtained from [53].

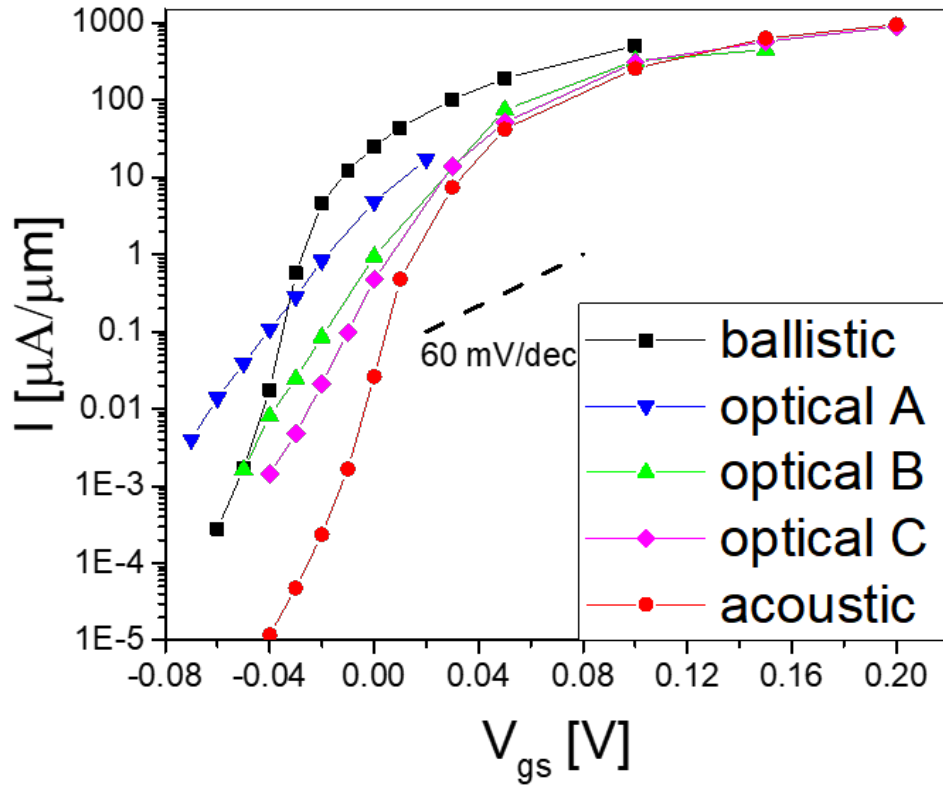


Fig. 3.5. IV Characteristics for the Resonance TFET comparison ballistic to local scattering with different scattering strengths. Optical C is used the Silicon non-polar deformation constant value of 110 eV/nm. Optical B is approximately two times this value and Optical A is four times optical C.

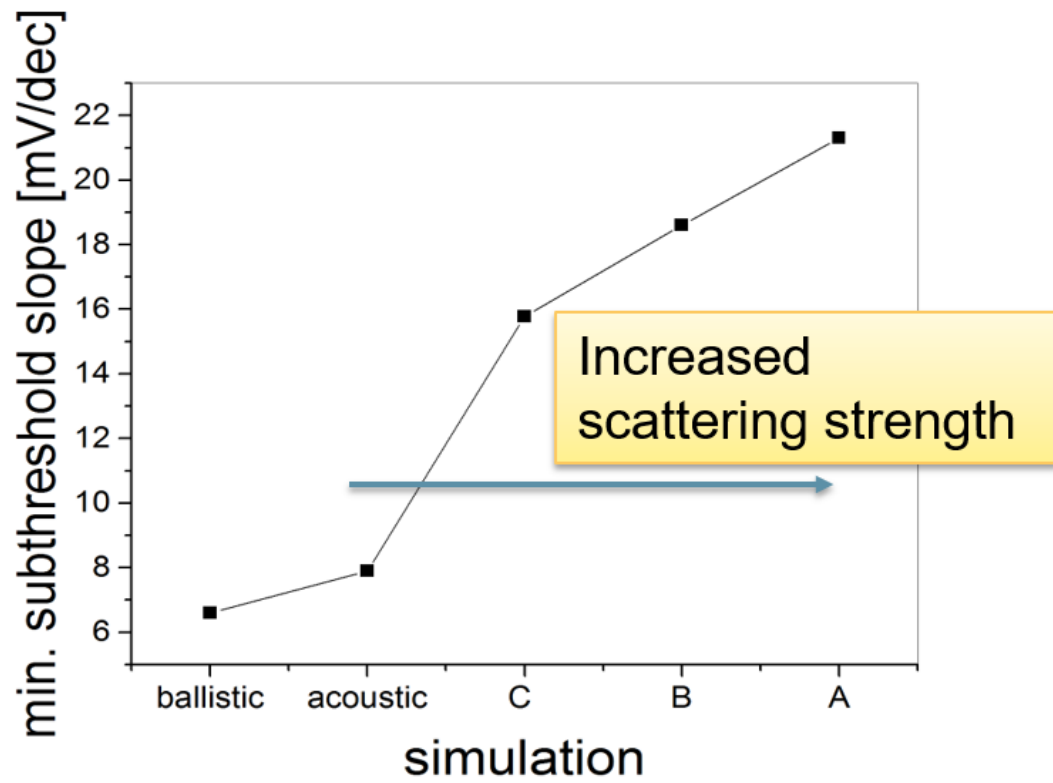


Fig. 3.6. Subthreshold Slope comparison for the different configurations. Optical C is used the Silicon non-polar deformation constant value of 110 eV/nm. Optical B is approximately two times this value and Optical A is four times optical C. [53].



## 4. NEW NONLOCAL RECURSIVE GREEN'S FUNCTION ALGORITHM

### 4.1 Validation : Nonlocal Recursive Green's Function Algorithm

This section the nonlocal recursive Green's (NL-RGF) function will be validated against traditional recursive Green's function algorithm (RGF) in the ballistic case and also against a full inversion for both a simple proportional to the Green's functions scattering and polar optical phonon scattering.

Using the device of ref. [54], a resonance TFET ultra-thin body as shown in fig. 3.4, the ballistic current is calculated using the two different methods. The results for different gate voltages are shown in fig. 3.4. NL-RGF matches the traditional RGF exactly.

The next comparison is a numerical comparison of  $G^R$  to full inversion when NL-RGF is used to calculate all off-diagonal elements. A bulk (quasi-1D) Silicon device in an  $sp^3d^5s^*$  10 band basis is simulated. A simple scattering mechanism where the scattering self-energies are proportional to the Green's function, i.e.  $\Sigma^{</R} = \lambda G^{</R}$  with  $\lambda$  being the scattering strength is used. Both the real and imaginary parts of  $G^R$  are compared. The results are shown in fig. 4.2.

The previous scattering mechanism used was artificial but was a good test as a validation. A more physical scattering mechanism is polar optical phonon. For this test, a bulk GaAs in effective mass is calculated. In polar optical phonon scattering, the nonlocality is a function of the screening length. For this reason, the device is calculated with different screening lengths varying from 5 to 40 nm. Since the scattering self-energy is a matrix, the anti-diagonal can be plotted to show the non-locality extent. This can be seen in figure 4.3. The lines are the full inversion and for comparison the symbols are NL-RGF.

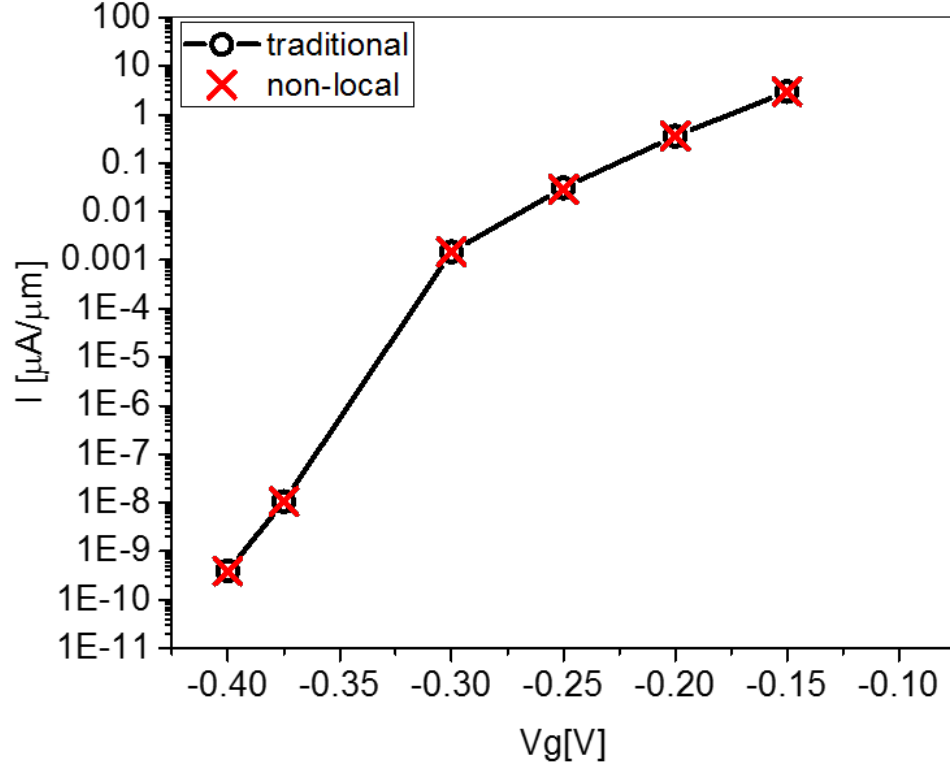


Fig. 4.1. Current-voltage comparison for traditional RGF and nonlocal RGF.

The timing and memory performance of NL-RGF is also calculated. For this case, a device is used larger than full inversion can handle on today's machines. If full inversion was used, 150 GB would be needed for a single inversion. To understand the expense of NL-RGF, it is compared against traditional RGF. For the largest non-locality used of about 2 nm in the transport direction, non-local RGF takes about 150 times more and uses 8 times more memory. The details are shown in figure 4.4 and 4.5. For contrast, a single full inversion would take 150 GB of memory and is therefore not feasible on today's machines.

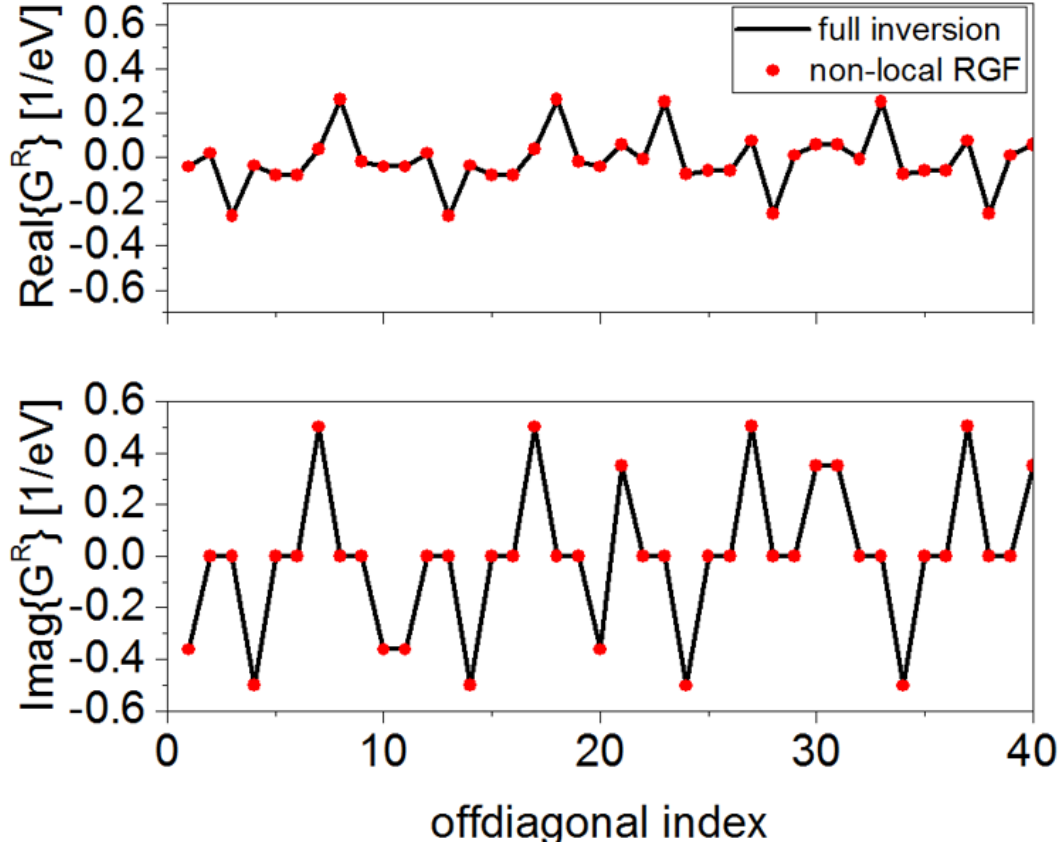


Fig. 4.2. Numerical comparison of  $G^R$  calculated with non-local RGF and with full inversion. Note: Same atom orbitals are summed for clarity.

In order to further understand the timing and memory of NL-RGF for different configurations, the NL-RGF algorithm was ran with different slab sizes in the transport direction. The default is to use the thinnest possible layer. In atomistic, first nearest-neighbor, the thinnest layer corresponds to an atomic thin layer. The slab was increased to two times and four times this value. The results are shown in figure 4.6 and 4.7. To help guide the eye, a horizontal line at a ratio between non-local and local time of 150 is shown along with the amount of nonlocality that can be covered. For an atomic layer a non-locality range of 2.7 nm is coverable. For the case with two times an atomic layer, the nonlocality is more than triple with 6.5nm. The last

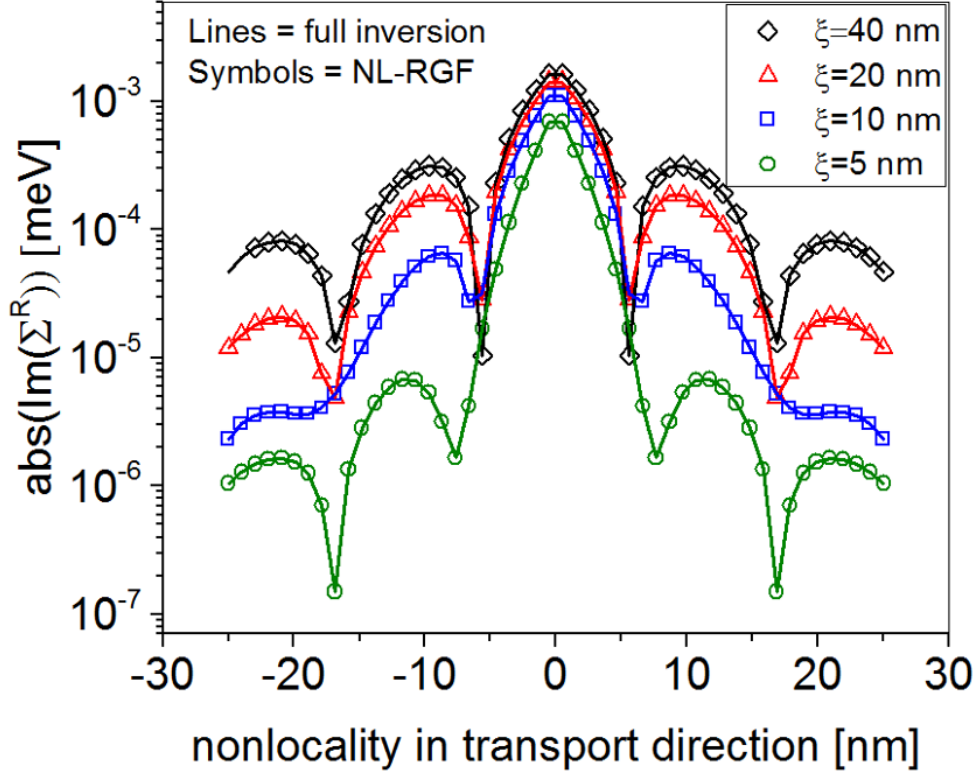


Fig. 4.3. The anti-diagonal of  $\Sigma_{POP}^R$  comparison of full inversion and NL-RGF for different screening lengths. The lines are full-inversion and the symbols are NL-RGF.

case, 4 times an atomic layer, shows the maximum non-locality range as 8.7 nm. As expected the memory increases linearly as a function of non-locality range for all three cases. These figures show the trade-off between time and memory. The takeaway is that if the goal is to include more non-locality and the memory limitations permit, it is advantageous to increase the block size.

The previous results are the results from simulation time. Overhead and non-optimal programming can cause the results to deviate from the theoretical limits. To further understand the NL-RGF algorithm, the NL-RGF algorithm complexity can be compared to the full inversion complexity. The NL-RGF complexity is calculated

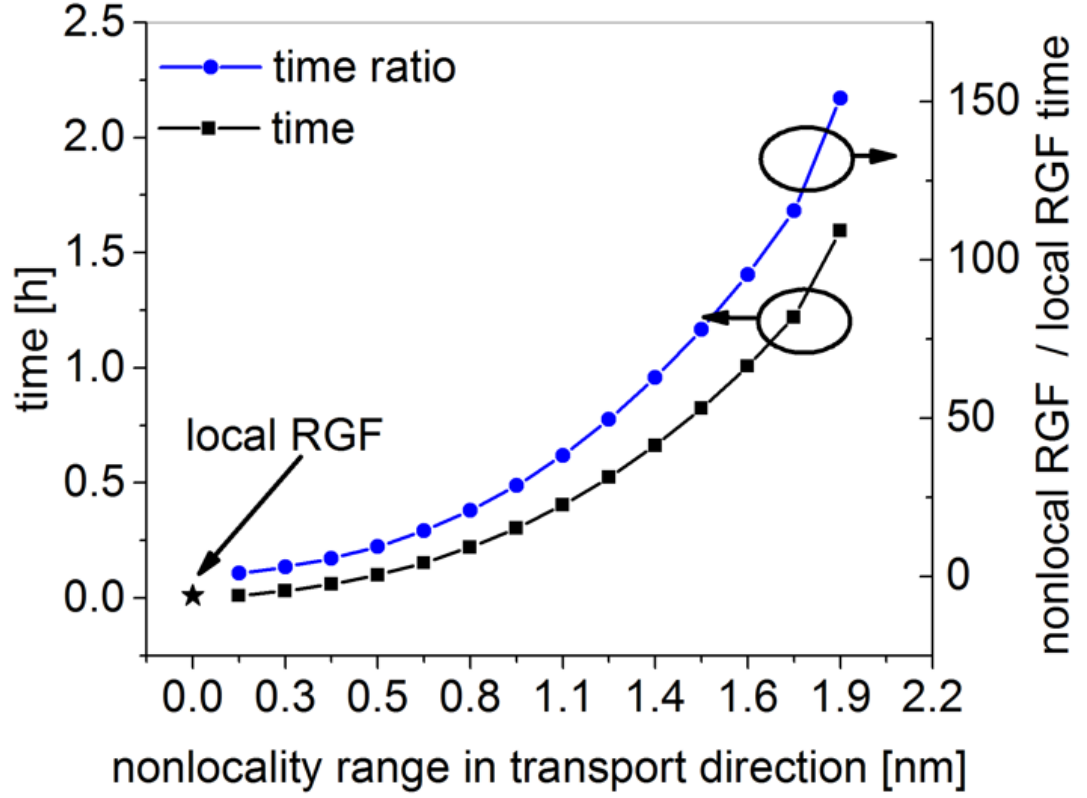


Fig. 4.4. Timing for NL-RGF as a function of non-locality in the transport direction. For comparison, the timing is plotted against the traditional (local) RGF.

as the number of multiplications and inversions needed multiplied by the complexity for a given slab. For this comparison, the slab sizes are all considered to be the same. The complexity of the full inversion is  $3N^3$  where  $N$  is the total size of the device matrix. 3 is included for  $G^R$  inversion and the calculation of  $G^<$  which includes two multiplications:

$$factor = \frac{NL - RGF}{fullinversion} = \frac{(\#mult. + \#inv.)n^3}{3N^3} \quad (4.1)$$

It is illustrative to calculate the point at which the NL-RGF and full-inversion has the same unit time. The results are shown in figure 4.8. Fitting the result to a

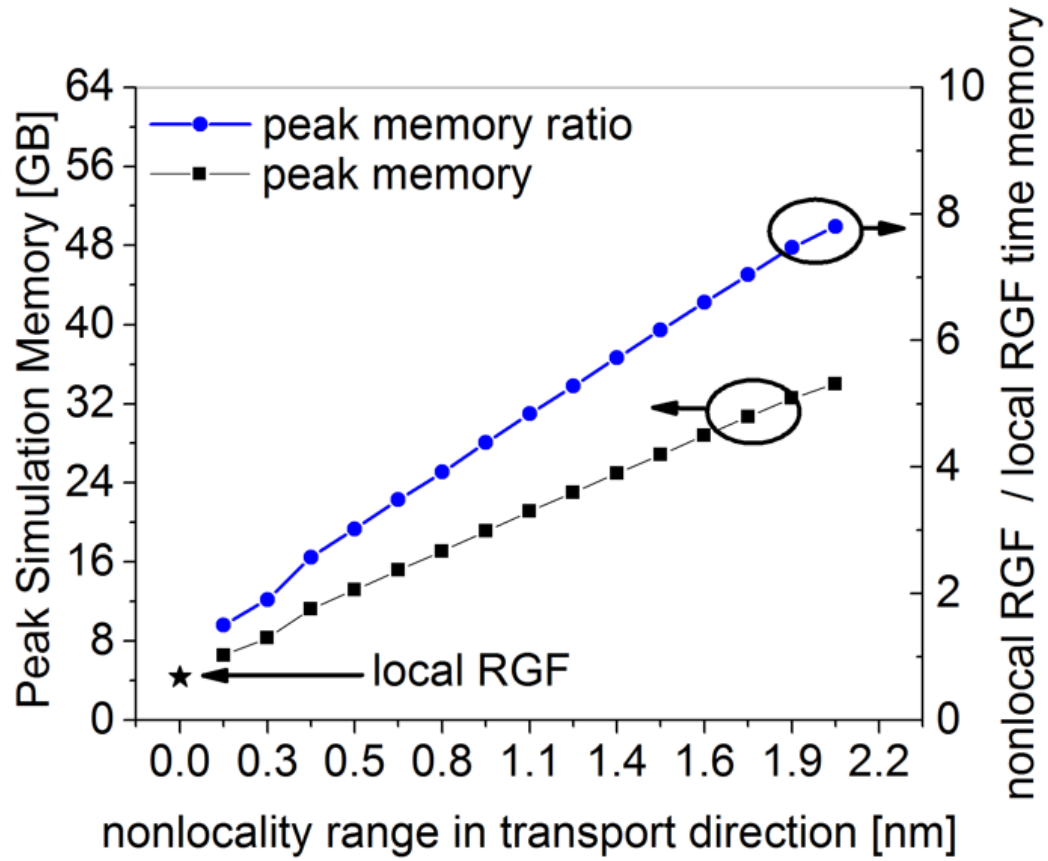


Fig. 4.5. Memory for NL-RGF as a function of non-locality in the transport direction. For comparison, the memory is plotted against the traditional (local) RGF.

power, the NL-RGF algorithm has a complexity, with respect to off-diagonality on the order of 2.2. These results show that the NL-RGF algorithm is advantageous for time up to 40 off-diagonal blocks. For typical atomic layer thicknesses, around .125 nm, this corresponds to including 5 nm of off-diagonality.

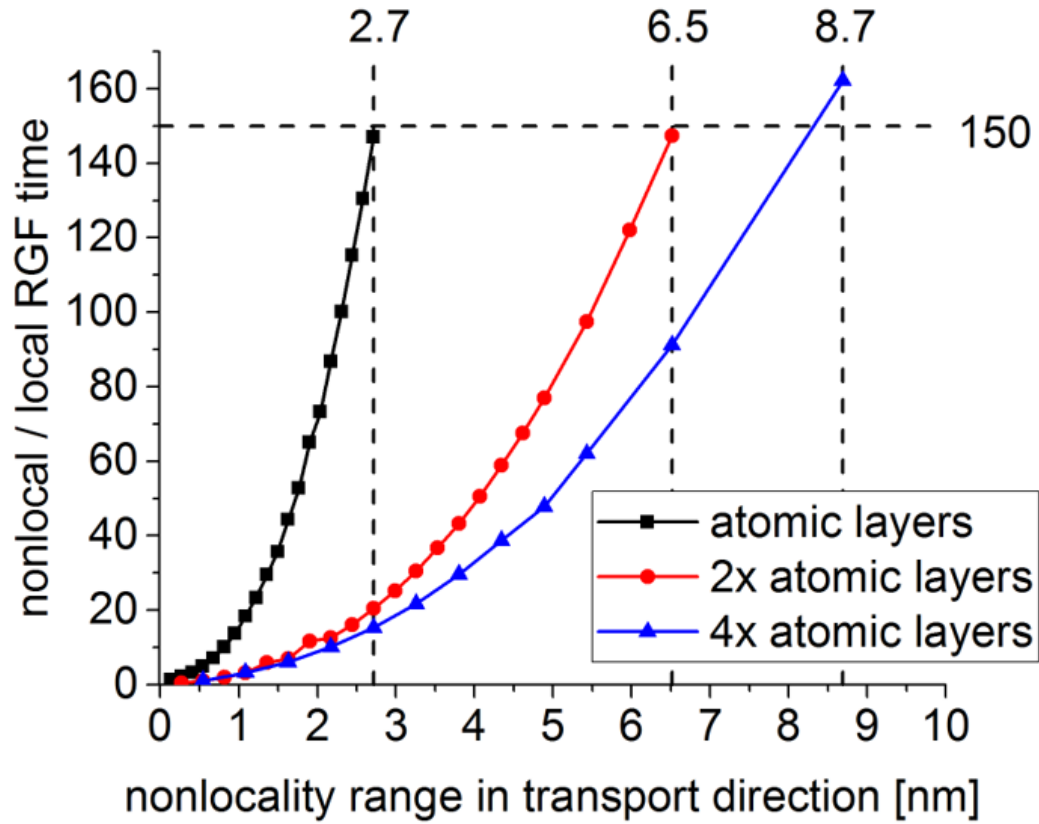


Fig. 4.6. Timing for NL-RGF as a function of non-locality in the transport direction for three different sizes of slabs. A horizontal line at the ratio of non-local to local time of 150 is added to guide the eye.

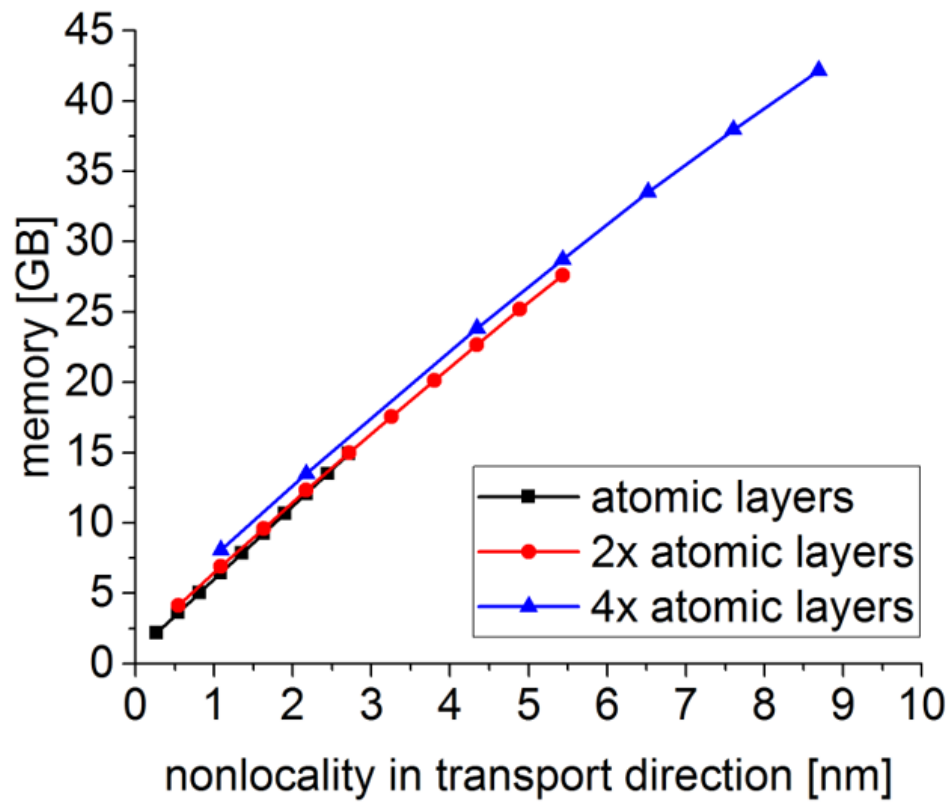


Fig. 4.7. Memory for NL-RGF as a function of non-locality in the transport direction for three different sizes of slabs.



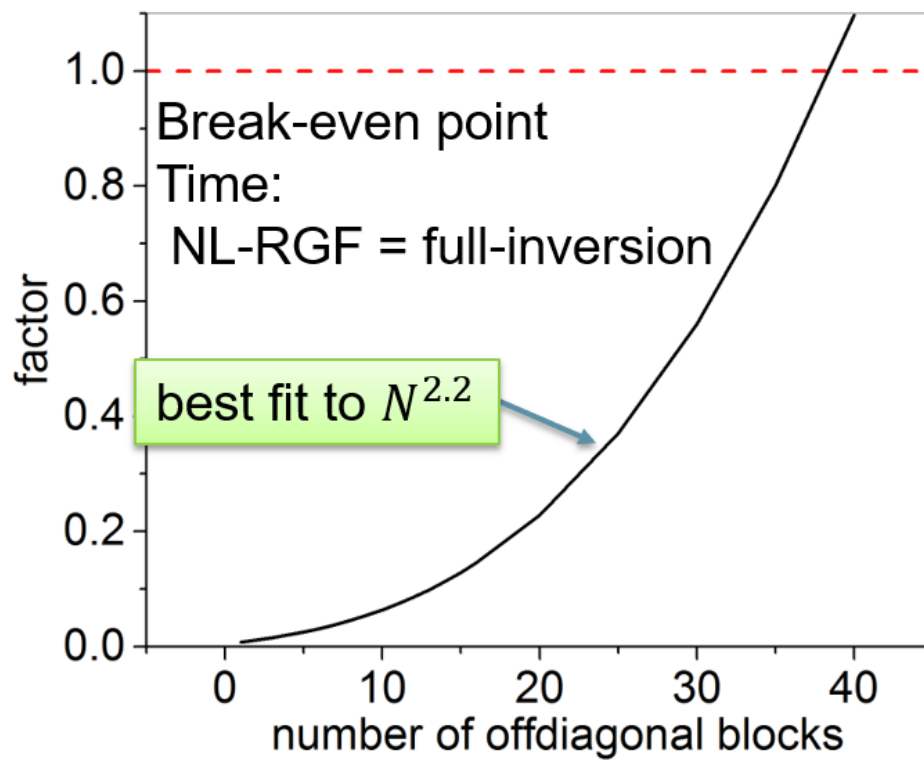


Fig. 4.8. The theoretical comparison of complexity of NL-RGF to full inversion. The break even point is marked with a red dashed line to guide the eye.

## 4.2 Nonlocal Recursive Green's Function Derivation and Details

### 4.2.1 General concept for the retarded Green's function

The recursive Green's function algorithm foots on a block  $LDL^T$  decomposition:

$$\begin{aligned}
 (\mathbf{G}^R)^{-1} &= LDL^T \\
 &= \begin{pmatrix} \ddots & & & \\ & \ddots & & \\ & & 1 & 0 & 0 \\ & & L_{q-1,q-2} & 1 & 0 & \ddots \\ & & 0 & L_{q,q-1} & 1 & \ddots \\ & & & \ddots & \ddots & \ddots \end{pmatrix} \begin{pmatrix} \ddots & & & \\ & \ddots & & \\ & & D_{q-1,q-1} & 0 \\ & & 0 & D_{q,q} & 0 \\ & & & 0 & D_{q+1,q+1} & \ddots \\ & & & \ddots & \ddots & \ddots \end{pmatrix} \\
 &\quad \begin{pmatrix} \ddots & \ddots & & \\ & \ddots & 1 & (L_{q-1,q-2})^T & 0 \\ & & 0 & 1 & (L_{q,q-1})^T & \ddots \\ & & & 0 & 1 & \ddots \\ & & & & \ddots & \ddots \end{pmatrix}, \tag{4.2}
 \end{aligned}$$

with  $T$  denoting the transpose of a matrix. The generator functions of the last equation are given by

$$D_{q,q} = (G^R)_{q,q}^{-1} - \sum_{k=0}^{q-1} L_{q,k} D_{k,k} (L_{q,k})^T, \tag{4.3}$$

$$L_{q,j} = \left[ (G^R)_{q,j}^{-1} - \sum_{k=0}^{j-1} L_{q,k} D_{k,k} (L_{j,k})^T \right] D_{j,j}^{-1}. \tag{4.4}$$

It is worth the mention the result in the case of a tri-diagonal  $G^{R-1}$  (e.g. in a ballistic 1st nearest neighbor tight binding situation)

$$G_{q,q}^R = (G^R)_{q,q}^{-1} - L_{q,q-1} D_{q-1,q-1} (L_{q,q-1})^T, \tag{4.5}$$

$$L_{q,q-1} = (G^R)_{q,q-1}^{-1} D_{q-1,q-1}^{-1}. \tag{4.6}$$

## 4.2.2 Recursive Green's Function Algorithm Overview

### Introduction

The recursive Green's function is based off of two separate steps: The first step is the forward recursive Green's function where the algorithm starts from the left hand side of the device connected to the left lead. The algorithm is then calculated recursively, marching through the device towards the right hand side. Once the algorithm reaches the right hand side of the device and connects to the right lead, the backward step is then conducted to get the exact Green's functions. Details of both of these steps are below.

### 4.2.3 Forward recursive Green's function

The goal of this step is to solve the so-called left connected forward recursive Green's functions  $g^R$  and  $g^<$ .

#### Standard Tridiagonal forward $g^R$

We can deduce the standard tridiagonal forward RGF formula from Eqs. (4.5) and (4.6). The diagonal blocks of the inverse forward retarded Green's function  $(g^R)^{-1}$  contain only the energy  $E$ , the diagonal block Hamiltonian  $H$  and the scattering self-energy  $\Sigma^R$

$$g_{q,q}^R = E - H_{q,q} - \Sigma_{q,q}^R - H_{q,q-1}g_{q-1,q-1}^R H_{q-1,q} \text{ (tridiagonal)}. \quad (4.7)$$

Note that the initial block of  $(g^R)^{-1}$  also contains a contact self-energy.

### Nonlocal scattering in $g^R$

In the following the Eq. (4.4) is applied on the forward retarded Green's function (i.e.  $D = (g^R)^{-1}$ ). In order to avoid terms with  $(g^R)^{-1}$  in the formula for  $(g^R)^{-1}$ , we substitute Eq. (4.4) into Eq. (4.3)

$$\begin{aligned}
& (g_{q,q}^R)^{-1} \\
&= (G^R)_{q,q}^{-1} - \sum_{k=q-1-N}^{q-1} \left[ (G^R)_{q,k}^{-1} - \sum_{k'=k-1-N}^{k-1} L_{q,k'} (g_{k',k'}^R)^{-1} (L_{k,k'})^T \right] g_{k,k}^R (g_{k,k}^R)^{-1} \\
&\times \left\{ \left[ (G^R)_{q,k}^{-1} - \sum_{k'=0}^{k-1} L_{q,k'} (g_{k',k'}^R)^{-1} (L_{k,k'})^T \right] g_{k,k}^R \right\}^T \\
&= (G^R)_{q,q}^{-1} - \sum_{k=q-1-N}^{q-1} \left[ (G^R)_{q,k}^{-1} - \sum_{k'=k-1-N}^{k-1} L_{q,k'} (g_{k',k'}^R)^{-1} (L_{k,k'})^T \right] (g_{k,k}^R)^T \\
&\times \left[ (G^R)_{q,k}^{-1} - \sum_{k'=k-1-N}^{k-1} L_{q,k'} (g_{k',k'}^R)^{-1} (L_{k,k'})^T \right]^T. \tag{4.8}
\end{aligned}$$

Here,  $N$  is the number of rows of offdiagonal blocks of  $(G^R)^{-1}$ . Note that the inverse  $(g_{0,0}^R)^{-1}$  is given by construction

$$(g_{0,0}^R)^{-1} = (G^R)_{0,0}^{-1} = E - H_{0,0} - \Sigma_{0,0}^R. \tag{4.9}$$

For the  $q = 1$  case, the equation holds

$$\begin{aligned}
(g_{1,1}^R)^{-1} &= (G^R)_{1,1}^{-1} - (G^R)_{1,0}^{-1} g_{0,0}^R \left[ (G^R)_{1,0}^{-1} \right]^T \\
L_{1,0} &= (G^R)_{1,0}^{-1} g_{0,0}^R. \tag{4.10}
\end{aligned}$$

For the  $q = 2$  case, the equation holds

$$\begin{aligned}
(g_{2,2}^R)^{-1} &= (G^R)_{2,2}^{-1} - \left[ (G^R)_{2,0}^{-1} \right] (g_{0,0}^R)^T \left[ (G^R)_{2,0}^{-1} \right]^T \\
&\quad - \left[ (G^R)_{2,1}^{-1} - L_{2,0} (g_{0,0}^R)^{-1} (L_{1,0})^T \right] (g_{1,1}^R)^T \\
&\quad \times \left[ (G^R)_{2,1}^{-1} - L_{2,0} (g_{0,0}^R)^{-1} (L_{1,0})^T \right]^T \tag{4.11}
\end{aligned}$$

$$L_{2,0} = (G^R)_{2,0}^{-1} g_{0,0}^R \tag{4.12}$$

Substituting the  $L_{1,0}$  and  $L_{2,0}$  into the  $(g_{2,2}^R)^{-1}$  gives

$$\begin{aligned}
& (g_{2,2}^R)^{-1} \\
&= (G^R)_{2,2}^{-1} - (G^R)_{2,0}^{-1} (g_{0,0}^R)^T \left[ (G^R)_{2,0}^{-1} \right]^T \\
&- \left[ (G^R)_{2,1}^{-1} - (G^R)_{2,0}^{-1} g_{0,0}^R D_{0,0} \left( (G^R)_{1,0}^{-1} g_{0,0}^R \right)^T \right] (g_{1,1}^R)^T \\
&\times \left[ (G^R)_{2,1}^{-1} - (G^R)_{2,0}^{-1} g_{0,0}^R D_{0,0} \left( (G^R)_{1,0}^{-1} g_{0,0}^R \right)^T \right]^T \\
&= (G^R)_{2,2}^{-1} - \left[ (G^R)_{2,0}^{-1} \right] (g_{0,0}^R)^T \left[ (G^R)_{2,0}^{-1} \right]^T \\
&- \left\{ (G^R)_{2,1}^{-1} - (G^R)_{2,0}^{-1} (g_{0,0}^R)^T \left[ (G^R)_{1,0}^{-1} \right]^T \right\} (g_{1,1}^R)^T \\
&\times \left\{ (G^R)_{2,1}^{-1} - (G^R)_{2,0}^{-1} (g_{0,0}^R)^T \left[ (G^R)_{1,0}^{-1} \right]^T \right\}. \tag{4.13}
\end{aligned}$$

We simplify this equation further using  $(g_{0,0}^R)^T = g_{0,0}^R$

$$\begin{aligned}
& (g_{2,2}^R)^{-1} \\
&= (G^R)_{2,2}^{-1} - \left[ (G^R)_{2,0}^{-1} \right] g_{0,0}^R \left[ (G^R)_{2,0}^{-1} \right]^T \\
&- \left\{ (G^R)_{2,1}^{-1} - (G^R)_{2,0}^{-1} g_{0,0}^R \left[ (G^R)_{1,0}^{-1} \right]^T \right\} g_{1,1}^R \\
&\times \left\{ (G^R)_{2,1}^{-1} - (G^R)_{2,0}^{-1} g_{0,0}^R \left[ (G^R)_{1,0}^{-1} \right]^T \right\}. \tag{4.14}
\end{aligned}$$

To ease the coming equations, we define

$$\tilde{L}_{q,k} \equiv (G^R)_{q,k}^{-1} - \sum_{k'=q-1-N}^{k-1} \tilde{L}_{q,k'} g_{k',k}^R \left( \tilde{L}_{k,k'} \right)^T, \tag{4.15}$$

which gives for the forward retarded Green's function  $g^R$

$$g_{q,q}^R = \left[ (G^R)_{q,q}^{-1} - \sum_{k=q-1-N}^{q-1} \tilde{L}_{q,k} g_{k,k}^R \left( \tilde{L}_{q,k} \right)^T \right]^{-1}. \tag{4.16}$$

We note that in literature [55] some variables for the diagonal blocks of matrix  $G^R$  are defined extra

$$G^R = A^{-1}, \tag{4.17}$$

$$g^{R0} = \begin{pmatrix} (A_{1:q,1:q})^{-1} & 0 \\ 0 & (A_{q+1,q+1})^{-1} \end{pmatrix} = \begin{pmatrix} g_{1:q,1:q}^{R0} & 0 \\ 0 & g_{q+1,q+1}^{R0} \end{pmatrix} \tag{4.18}$$

The  $L_{q,k}$  and  $\tilde{L}_{q,k}$  differ in the inverse of the respective central matrix in the product of the sum and in the extra multiplication of  $g^R$  in the case of  $L_{q,k}$ . This way, however, the  $(g^R)^{-1}$ 's do not depend on  $(g^R)^{-1}$ , but on  $g^R$  instead. For later reference, we reformulate Eq. (4.16) using the definition of  $A$  and the final result of this section

$$g_{q,q}^R = \left[ A_{q,q} - \sum_{k=q-1-N}^{q-1} \tilde{L}_{q,k} g_{k,k}^R \left( \tilde{L}_{q,k} \right)^T \right]^{-1}, \quad (4.19)$$

with

$$\tilde{L}_{q,k} = A_{q,k} - \sum_{k'=q-1-N}^{k-1} \tilde{L}_{q,k'} g_{k',k'}^R \left( \tilde{L}_{k,k'} \right)^T. \quad (4.20)$$

### Nonlocal scattering in $g^<$

Using the  $LDL^T$  decomposition, the nonlocal  $g^R$ , and the decomposition

Starting from the  $LDL^\dagger$  decomposition that was used for  $g^R/G^R$ :

$$A = (E - H - \Sigma_{scatt} - \Sigma_{contact}) = LDL^\dagger \quad (4.21)$$

To avoid extra inversions it is more convenient to use  $\tilde{L}_{i,j}$ , where  $i$  and  $j$  are layer indices. To convert between  $L_{i,j}$  and  $\tilde{L}_{i,j}$

$$\tilde{L}_{i,j} = L_{i,j} g_{j,j}^R \quad (4.22)$$

The Keldysh equation for  $g^<$  is

$$A g^< = \Sigma^< (g^R)^\dagger \quad (4.23)$$

$$LDL^\dagger g^< = \Sigma^< (g^R)^\dagger \quad (4.24)$$

$$g^< = (L^{-1})^\dagger D^{-1} L^{-1} \Sigma^< (g^R)^\dagger \quad (4.25)$$

Replace  $L$  with  $-L$  for below:

**off-diagonal**  $g_{i,j}^<$  with  $i > j$

$$g_{i,j}^< = g_{i,i}^R \sum_{k=i-n}^{i-1} \tilde{L}_{i,k} g_{k,j}^< + g_{i,i}^R \sum_{k=i-n}^{j-1} \Sigma_{i,k}^< g_{k,j}^A + g_{i,i}^R \Sigma_{i,j}^< g_{j,j}^A \quad (4.26)$$

**diagonal**  $g_{i,i}^<$

$$g_{i,i}^< = g_{i,i}^R \sum_{k=i-n}^{i-1} \tilde{L}_{i,k} \left( -g_{i,k}^< \right)^\dagger + g_{i,i}^R \sum_{k=i-n}^{i-1} \Sigma_{i,k}^< \sum_{l=k}^{i-1} g_{k,l}^A \tilde{L}_{l,i} g_{i,i}^A + g_{i,i}^R \Sigma_{i,i}^< g_{i,i}^A \quad (4.27)$$

#### 4.2.4 Backward recursive Green's function

To get the exact Green's functions, the backward step is used along with the previously calculated  $g^R$  and  $g^<$ .

##### Standard Tridiagonal forward $G^R$

The backward recursive Green's function  $G^R$  in the case of a “standard” tridiagonal  $(G^R)^{-1}$  reads

$$G_{q,q}^R = g_{q,q}^R - g_{q,q}^R H_{q,q+1} G_{q+1,q}^R \text{ (tridiagonal)}. \quad (4.28)$$

##### Nonlocal scattering in $G^R$

It is plausible that the offdiagonal block of the Hamiltonian matrix  $H_{q,q+1}$  gets augmented by all remaining offdiagonal matrix blocks of  $(G^R)^{-1}$  in a more general situation

$$G_{q,q}^R = g_{q,q}^R - g_{q,q}^R \sum_{j=q+1}^{q+1+N} \tilde{L}_{q,j} G_{j,q}^R \quad (4.29)$$

The same plausibility holds for the offdiagonal blocks of  $G^R$

$$G_{q,k}^R = -g_{q,q}^R \sum_{j=q+1}^{q+1+N} \tilde{L}_{q,j} G_{j,k}^R \quad (4.30)$$

### Nonlocal scattering in $G^<$

The Keldysh equation for  $G^<$  can be written as:

$$G^< = (I - L^T) G^< + g^< (L^T)^{-\dagger} \quad (4.31)$$

Replace L with -L for below:

**off-diagonal**  $G_{i,j}^<$  with  $i < j$

$$G_{i,j}^< = g_{i,j}^< + \sum_{k=i+1}^{i+1+n} g_{i,k}^< L_{k,j}^\dagger g_{j,j}^A + g_{i,i}^R \sum_{k=i+1}^{i+1+n} L_{i,k}^T G_{k,j}^< \quad (4.32)$$

**diagonal**  $G_{i,i}^<$

$$G_{i,i}^< = g_{i,i}^< + \sum_{k=i+1}^{i+1+n} g_{i,k}^< L_{k,i}^\dagger g_{i,i}^A + g_{i,i}^R \sum_{k=i+1}^{i+1+n} L_{i,k}^T G_{k,i}^< \quad (4.33)$$

But these equations have an issue mainly that they couple far-off diagonal elements. To remove this another recursive relation is found so far not exploited above to give us the final result of this section.

$$G_{i,i}^< = g_{i,i}^< + g_{i,i}^R \sum_{k=i+1}^{i+1+n} L_{i,k}^T G_{k,i}^< + \sum_{k=i+1}^{i+1+n} g_{i,k}^< \sum_{l=i+1}^{i+1+n} L_{k,l}^\dagger G_{l,i}^A + \sum_{k=i+1}^{i+1+n} g_{i,k}^R \sum_{l=k+1}^{k+1+n} \Sigma_{k,l}^< G_{l,i}^A \quad (4.34)$$

And with  $i < j$

$$G_{i,j}^< = g_{i,j}^< + g_{i,i}^R \sum_{k=i+1}^{i+1+n} L_{i,k}^T G_{k,j}^< + \sum_{k=i-n}^j g_{i,k}^< \sum_{l=j+1}^{j+1+n} L_{k,l}^\dagger G_{l,i}^A + \sum_{k=i-n}^i g_{i,k}^R \sum_{l=j+1}^{j+1+n} \Sigma_{k,l}^< G_{l,i}^A \quad (4.35)$$

### 4.3 Non-local Recursive Green's Function Results

Using the algorithm described above, first results are shown for an InGaAs wire with a 2nm diameter in effective mass. The device is 40 nm long. Polar optical phonon scattering is included with a screening length of 100 nm. Additionally, acoustic phonon scattering is included. The scattering is compared to ballistic in figure 4.9.



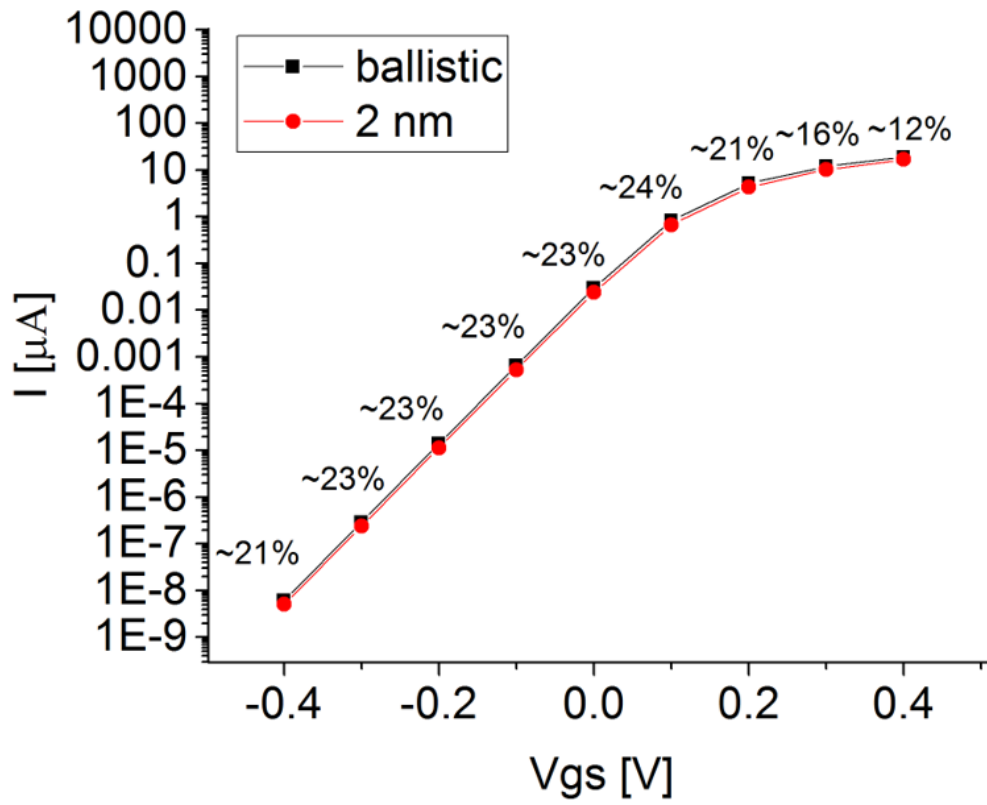


Fig. 4.9. IV characteristics for a 2nm diameter InGaAs wire in effective mass. The ballistic result is also shown for comparison.

## 5. PART II: OVERVIEW OF THE STATE OF THE ART OF MODELING CHEMICAL SYSTEMS IN LIQUIDS

This section will discuss in more detail the modeling efforts that exist for modeling molecules in an environment. The three main topics that will be outlined are density functional theory (DFT) with a continuum, implicit solvent model and some results for liquid systems. Also briefly discussed but not a major component of this thesis is the so-called molecular electronics where an a molecule is placed between two contacts and transport properties are measured/calculated. Molecular electronics is mentioned to discuss the commonalities and similarities between it and the method developed here. In the process of explaining, the state of the art of these methods, the pros and cons will also be assessed.

### 5.1 Overview of Density Functional Theory and its Applications

For an introduction to DFT, refs. [32] and [56] are good places to start. DFT has been used for a wide range of applications such as formation energies [57], structure relaxation [58], magnetic properties [59], bandstructures [60], and vibrational spectra [61] to name a few. In the context of liquids, DFT has been used for adsorption [62], properties of water [63] such as structure, forces, and electronic structure , and surface tensions such as in ref. [64]. It's obvious that DFT's application space has grown rapidly since its initial uses.

Even though DFT has a wide range of applications, only a small subsection mentioned above, there are several drawbacks to DFT. The first of which is at its core, it is absolute zero temperature theory. Additionally, DFT mathematical theory only promises the ground state of a system. The applications above stretch these two tenants to even include band gaps which is obviously an excited state property. Fun-

damental DFT does not get the bandgaps correctly but there are empirical fitting parameters included to help ease this issue [60]. Besides empirical fitting parameters to account for the absolute zero and ground state calculations, there are also attempts to augment DFT. The second drawback that is especially important in modeling liquid systems is that the DFT approach is predominantly limited to either ordered, crystalline systems or completely isolated. An open system is not covered in DFT and is a main advantage of the NEGF method.

### 5.1.1 Thermal and Excited State Density Functional Theory

#### Thermal Density Functional Theory

As discussed in the previous section, there are research efforts in order to include thermal in DFT. All DFT is based on minimization of the ground state and practical DFT relies on density functionals. The exact density function is chosen based on experience and the given application. In order to include finite temperature in DFT, the ground state energy minimization must be replaced by a statistical mechanical parallel. A particularly important operator is the entropy operator which is zero in the absolute temperature extreme. Details of the derivation of the statistical description functional is in ref. [65]. The idea of thermal DFT is not a new one. In actuality, a finite temperature generalization of the Hohenberg-Kohn theorem was published in 1965 by Mermin [66]. This begs the question why is thermal DFT not an everyday tool like zero temperature DFT? There are many popular, large-scale codes for zero temperature (e.g. Quantum Espresso [38] and VASP [37]). One reason is discussed in ref. [67]. They mention that for practical calculations a finite temperature exchange-correlation functional must be developed. These are more difficult to develop because with increasing temperature the number of basis sets needed increases rapidly. The conclusion of the discussion in ref [67], is that the "stage is set for their [finite T XC-functionals] implementation in practical DFT." Only time will tell if finite temperature DFT is practical.

## Excited State Density Functional Theory

In fundamental DFT theory, only the ground state is guaranteed with the variational principal. Efforts to include excited state information in DFT, usually lead to a time dependent formulation of DFT [68]. As is the usual prescription for DFT, a suitable functional is found. A thorough benchmark of 24 different time-dependent density functional methods is given in ref. [69]. One interesting application is the application of time-dependent (excited state DFT) to the design of dyes [70]. This review article also explains some of the drawbacks and pitfalls when trying to use TD-DFT. One drawback is the assumption of vertical transitions which might not always be true. Secondly, TD-DFT can yield substantial error for charge transfer excited states [71]. The last drawback and limits TD-DFT to small systems is the scaling of complexity. The time for a TD-DFT calculation scales to the 4th power with the number of atoms  $O(N_{atoms}^4)$ . This method is simply not feasible for calculation of disordered systems where easily 100s of atoms are needed for a proper description.

### 5.1.2 Density Functional Theory Applied to Water

One of the most important liquids for numerous chemical and biological applications is water. As has already been alluded to in previous sections, one of the key elements of a DFT calculation is a proper choice of the exchange-correlation functionals. A logical question is how do the functionals compare for water and which is the best. This turns out in fact to be a difficult question. Luckily, a recent review article has explored this question [72] in significant detail. They explore water monomers, dimers, complicated clusters, and ice. The final and most complicated system of question is water as a liquid.

Different properties such as H-bond energies, polarizability, and binding energy are compared for different functionals and scored. It comes as no surprise that depending on the property different functionals perform better than others. The worst performing is low density approximation (LDA) which is one the simplest XC-functionals.

Another observation is that one of the highest performing (highest average score of different properties and gives a reasonable liquid structure) has too large of a binding energy in ice. The conclusion is that none of the functionals catches all important properties well and care must be taken when choosing a functional for a given application. It is also important to note the time cost for the functionals. Two main classes are discussed (generalized gradient)GGA methods, and hybrid functionals. Hybrid functionals generally are an order of magnitude more expensive than GGA.

### 5.1.3 Implicit Solvent Models

Due mainly to the limitation of DFT to relatively small systems, the solvent is most often not modeled quantum-mechanically and explicitly. The solvent is treated in a classical continuum as an electrostatic boundary condition provided by the solvent. The active ingredient DFT results are then post-processed using this electrostatic boundary condition and the role of the solvent is approximated. This method misses important ingredients such as charge transfer between the active ingredient and the solvent and repositioning of the solvent atoms due to the presence of the active ingredient. Implicit solvent methods are parametrized agnostic to the active ingredient in question [33], [34], [35]. These implicit solvent methods are then used to assess the solubility using approximations to the Gibbs free energy of hydration [73] which gives the energy for the system to transition from the gas phase to the solution phase. Also sometimes needed in drug design is the Gibbs free energy of sublimation [74], [75] which gives the energy for the system to break crystalline form and become a gas. Due to the importance and wide usage of the implicit solvent models, the next chapter will be devoted to discussing details and explaining some of the methods widely employed.

## 5.2 Molecular Electronics

This section will explore the applications of molecular electronics and what part Nonequilibrium Green's functions play. The main motivation for this section is to explain what most researchers typically mean when they say molecular electronics and what the differences are between this and what is discussed in later sections. Molecular electronics typically implies a molecule in contact with two metallic contacts that act as heat and charge reservoirs. Electron transport properties are then simulated/measured through the molecule. A typical device is shown in figure 5.1. Two copper contacts are in contact with a C60 fullerene molecule. Their results show that there is a large charge transfer from the metallic contacts to the molecule and the IV curves obtained with NEGF+DFT show a strong metallic behavior. Their conclusion is that the metallic contacts dominate the transport. Another molecular electronic result shows that the coupling strength of the molecule to the contact strongly affects the transport [76]. The contacts play the role of modifying the density of states and thus the density in the system. Attaching contacts leads to both a shift and broadening of the isolated states of the molecule. This is not unlike what a solvent does to a molecule in solution. The solvent acts like a contact, albeit dynamic, that shifts and broadens the density of states of the molecule. The reason for this comparison will come to light in chapter 9.

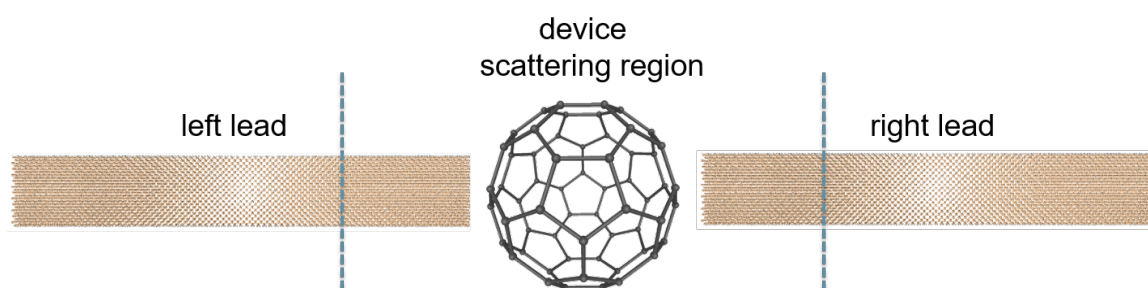


Fig. 5.1. Typical molecular electronic simulation setup. The molecule is placed between two ideal copper contacts. The delineation between the device and the infinite, ideal, and equilibrium leads is shown with a vertical dashed line on both sides.

## 6. IMPLICIT, EXPLICIT AND HYBRID SOLVENT METHODS

### 6.1 General Ingredients for Implicit Solvent Methods

In order to make predictions of the degree of solubility of an active ingredient in a solvent, a model must be created for the solvent. A lot of effort has been made in the field of chemistry to create an approximate continuum model for the solvent with varying degrees of approximations [77]. This section will be a summary of the major portions in ref. [77]. The majority of these models include the solvent in a continuum with an electrostatic boundary condition. When calculating the solubility, the Gibbs free energy of hydration and sublimation is often used. These two energies measures the change in energy when an active ingredients goes from the gas phase to a solution phase and from crystal to gas phase, respectively.

The goal of any implicit, continuum solvent model is to reduce the number of variables included to a tractable number. It is unfeasible in the most sophisticated DFT methods to include all of the solvent atoms. In the way DFT is formulated, this would introduce a larger number of solvent atoms explicitly included. In creating a continuum solvent model, the interactions with the solvent are approximated and an effective Hamiltonian is created. The interactions with the solvent are usually superimposed as a potential. A general expression for the Hamiltonian (omitting degree of freedom variables) is then:

$$H_{eff.} = H_{solute} + H_{int.} \quad (6.1)$$

where  $H_{int}$  is the component of the Hamiltonian due to the active ingredient's interaction with the solvent. Approximating this interaction is where the majority of the effort is spent when developing an implicit solvent method. A common ap-



proximation is that the interactions are local and contribute a scalar potential to the effective Hamiltonian. The permittivity of the solvent thus becomes an essential component where either the material permittivity can be used or a parametrized one.

In the simple model for implicit solvents several approximations are made and outlined below [77]

- only electrostatic interactions between solvent and solute
- very dilute solution
- solvent is isotropic and at equilibrium
- only consider the ground state of the solute
- no dynamic effects

Using these approximations,  $H_{int}$  can be written component wise:

$$H_{int.} = V_{int.} = V_{cavity} + V_{electrostatic} + V_{dispersion} + V_{repulsion} \quad (6.2)$$

where  $V_{cavity}$  is the energy needed to form the cavity  $V_{electrostatic}$  is the polarization of the active ingredient and the solvent  $V_{dispersion}$  is the band energy  $V_{repulsion}$  the quantum mechanical exchange repulsion term

## Defining the Cavity

In order to include the active ingredient in the solvent a cavity must be formed. In defining the implicit solvent model, a cavity is also formed. The cavity, in the most widely used method, is formed using the van der Waal's radii for the atoms of the active ingredient [78]. This is approximately the radius of interaction for the atoms. In practice, the radius is expanded by a small factor [79], [80], [81] in order to ensure that the strongest variation of the active ingredient has died out. The overall shape of the cavity is then formed Using the van der Waal's radii for each of the constituent atoms of the active ingredient. However, when the union of each of the van der

Waal's radii is formed, the formed shape can have kinks. This is an issue because the electric field is infinity at the kinks. An additional constraint must be added that the overall shape must be concave. Additional spheres are added at the kinks in order to smooth out the shape and have a constituent concave shape. Figure 6.1 shows the different components of the implicit solvent model. The active ingredient is treated atomistically, typically, with quantum mechanical rigor. However, since the solvent is implicit the cavity must be shaped. The cloud around the active ingredient shows the cavity. The active ingredient is solved in a vacuum. The last component is the dielectric continuum that surrounds the active ingredient and the cavity. In this example, the dielectric is a material parameter with no spatial dependence. More sophisticated methods exist but all are based on this idea. The surface charge density on the cavity is formed from dielectric continuum and is solved with Gauss' law.

There are also more sophisticated methods for calculating the cavity based off of physical requirements. One such definition is an isodensity surface [82], i.e. variations due to the active ingredient have decayed and the interface with the solvent is physically expected. In this method, the electron density is checked iteratively changing the size of the cavity until the threshold is reached. A more expensive method is based off of calculating the interaction energy between an inert gas probe atom and the active ingredient. This probe, like the isodensity method, is used to find the interface between the active ingredient and the solvent [83]. The results of this thesis use the van der Waal's radii to form the cavity but unlike the implicit solvation model, the kinks at these spheres are not a problem as will be explained in detail in later chapters.

## Basics of the electrostatic Problem

In the majority of implicit solvent models, the interactions between the solvent and the active ingredient are purely electrostatic in nature. The density and thus the potential of the active ingredient can be solved quantum mechanically such as with

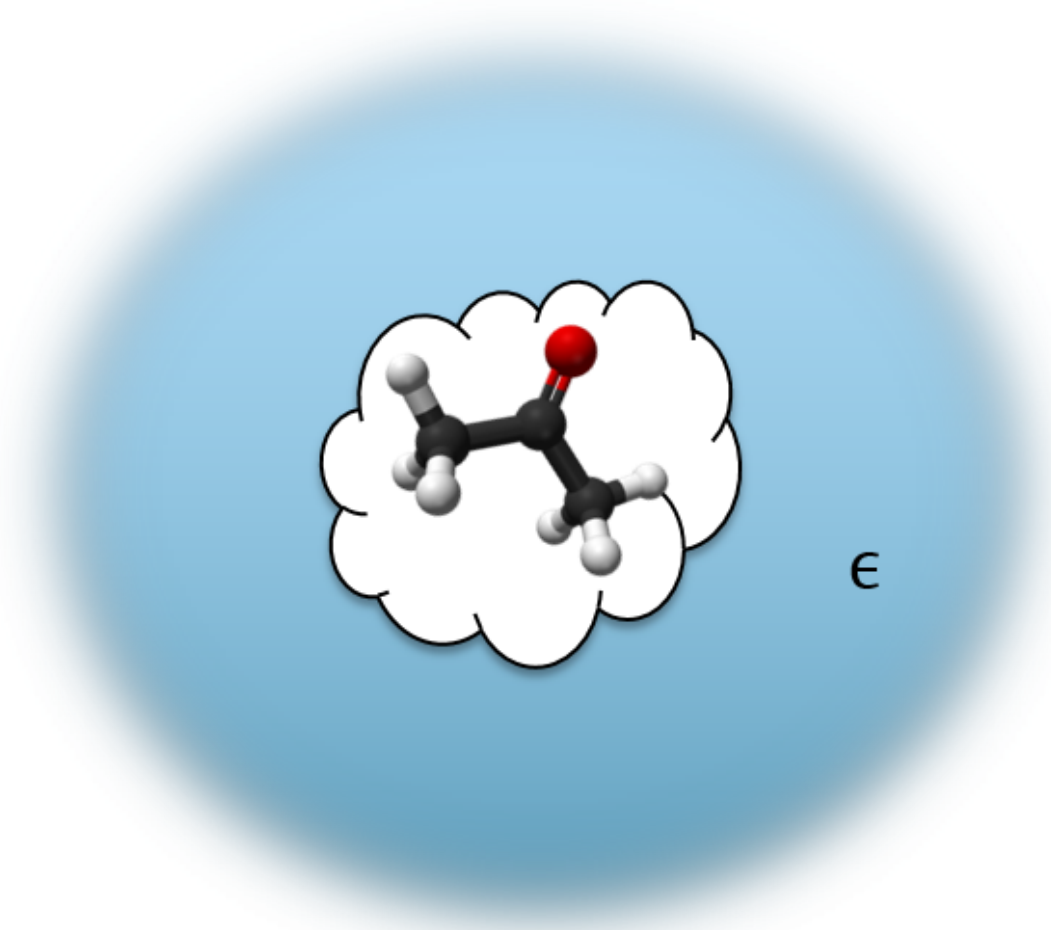


Fig. 6.1. A schematic of the different components that makeup the implicit solvent method.

DFT or similar quantum chemistry methods. The cavity's shape is formed possibly using one of the methods discussed above. Since the interaction is purely electrostatic in nature, the implicit solvent model is a classical model. The solvent is modeled as a dielectric medium in continuum. The charge density of the active ingredient,  $\rho_{active}$ , interacts electrostatically with the solvent thus polarizing the dielectric medium. This polarization of the solvent dielectric medium will then polarize the active ingredient. Computationally, this lends to a self-consistent procedure of the Poisson's equation

describing the interaction between the solvent and the active ingredient. Assuming spatial variations in the potential, density, and the dielectric constant. The Poisson equation is written generally as:

$$\vec{\nabla} \epsilon(\vec{r}) \nabla V(\vec{r}) = 4\pi \rho(\vec{r})_{active} \quad (6.3)$$

When solving this equation, an important simplification and assumption is made. The charge density outside of the cavity is zero. This assumption quickly breaks down for ionic solutions where the charge distribution in the bulk is important. For other solvents where this assumption can be used, an effective charge density is used at the surface of the cavity. The exact definition of the surface charge density can be broken down into two distinct camps. The first assumes that the solvent continuum is polarizable (a dielectric) (Polarizable Continuum Model). The other definition stems from assuming that the solvent continuum is a conductor (with  $\epsilon \rightarrow \infty$ ) (Conductor-like Screening Model). For completeness, details of the methods will be summarized below.

### **Polarizable Continuum Model**

To simplify the equations, the Polarizable Continuum Model (PCM) [84] typically assumes an isotropic and homogenous solvent. This isn't surprising since the spatial variations would not be included in an implicit model. With this assumption, the dielectric constant in the Poisson equation is simplified to be equal to 1 when inside the cavity and equal to  $\epsilon_{solvent}$  outside the cavity. The problem can now be re-cast into a potential:

$$V(\vec{r}) = V_{active}(\vec{r}) + V_{surface}(\vec{r}) \quad (6.4)$$

$V_{surface}$  is the potential generated from the surface charge assumed on the cavity due to the interaction with the solvent. Explicitly written:

$$V_{surface}(\vec{r}) = \int_{cavity} \frac{\sigma(\vec{t})}{|\vec{r} - \vec{t}|} d^2 \vec{t} \quad (6.5)$$

Since the expression for the dielectric constant is known and homogenous. It is trivial to write the surface charge density now in terms of the the potentials and the dielectric constants.

$$\sigma(\vec{r}) = \frac{\epsilon - 1}{4\pi\epsilon} \frac{\partial}{\partial n} (V_{active} + V_{surface}) \quad (6.6)$$

Once  $\sigma$  is known the problem is solved. Details of the numerical implementation can be found in [84].

### Conductor-like Screening Model

As mentioned above the conductor-like Screening Model (COSMO) sets  $\epsilon \leftarrow \infty$  as would be the case in a ideal conductor [85]. However unlike an ideal conductor the electric potential on the surface of the cavity does not disappear. The effect surface charge can then be calculated approximately for the dielectric solvent as a scaled factor of the ideal conductor charge.

$$\sigma = f(\epsilon) \sigma^* \quad (6.7)$$

Where  $f(\epsilon)$  is a scaling function as a function of  $\epsilon$ .

$$f(\epsilon) = \frac{\epsilon - 1}{\epsilon + x} \quad (6.8)$$

$x$  depends on the charge of the solvent. For charged molecules such as ions, this should be set to 0 and for neutral solvent molecules, set to 0.5. The values are derived from analytical electrostatic problems. If the cavity is assumed spherical and the multipole has an order  $l$ , the result is  $x = \frac{l}{l+1}$  [86].

Any other energy-related terms are also scaled by the same expression. This is the basic underlying theory of the COSMO model. Improvements and alternatives exist and can be found in the original paper [87] and follow-up papers [88], [89], [90].

It is worth noting that in practice all of these implicit solvent methods use empirical corrections and thus calculation of complicated substances often fails to give the same accuracy as the simpler compounds [91].

## 6.2 General Ingredients for Explicit Solvent Methods

In order to include more physics, explicit solvent methods with periodic boundary conditions have also been developed. These methods typically are solved with classical molecular dynamics. The active ingredient is solved and relaxed with ab-initio methods such as DFT and then placed in a periodic solvent box. The size of periodic box is chosen such that images of the active ingredient do not interact. The results strongly depend on the size of the cell due to the long-ranged Coulomb potential. The Coulomb-interaction, solved with Ewald summations for periodic calculations, leads to this strong dependence. In explicit methods, it is important to span the configurational space to get an accurate and reliable result. One way to do this is through the so-called thermodynamic integration method. In which a variational parameter,  $\lambda$  is used to modify some parameter in the simulation. This parameter modified should somehow relate to the physical property of interest. In the context of solvation energies, one choice is that  $\lambda$  varies the coupling strength between the active ingredient and the solvent. In classical MD, the two potentials that are most interest is the Lennard-Jones dispersion potential and the Coulomb potential. The Lennard-Jones dispersion potential approximates the interaction between neutral atoms. An example Lennard-jones with the contribution from the two different terms is shown in 6.2 They have the form:

$$U(r_{ij}) = \frac{q_i q_j}{r_{ij}} + 4\epsilon_{ij} \left[ \left( \frac{\sigma_{ij}}{r_{ij}} \right)^{12} - \left( \frac{\sigma_{ij}}{r_{ij}} \right)^6 \right] \quad (6.9)$$

Due to numerical considerations, this equation typically has an alternative form in order to soften the variations. It takes several forms but they all have something in common. There is a cut-off radius in order to avoid singularities. It is easy to see that the denominator in both the Coulomb potential (first term) and the Lennard-Jones potential (2nd term) tends towards  $\infty$ .

The parameter  $\lambda$  is used to scale both these potentials and help span the configurational space. Figure 6.3 shows the structure. The active ingredient is surrounded

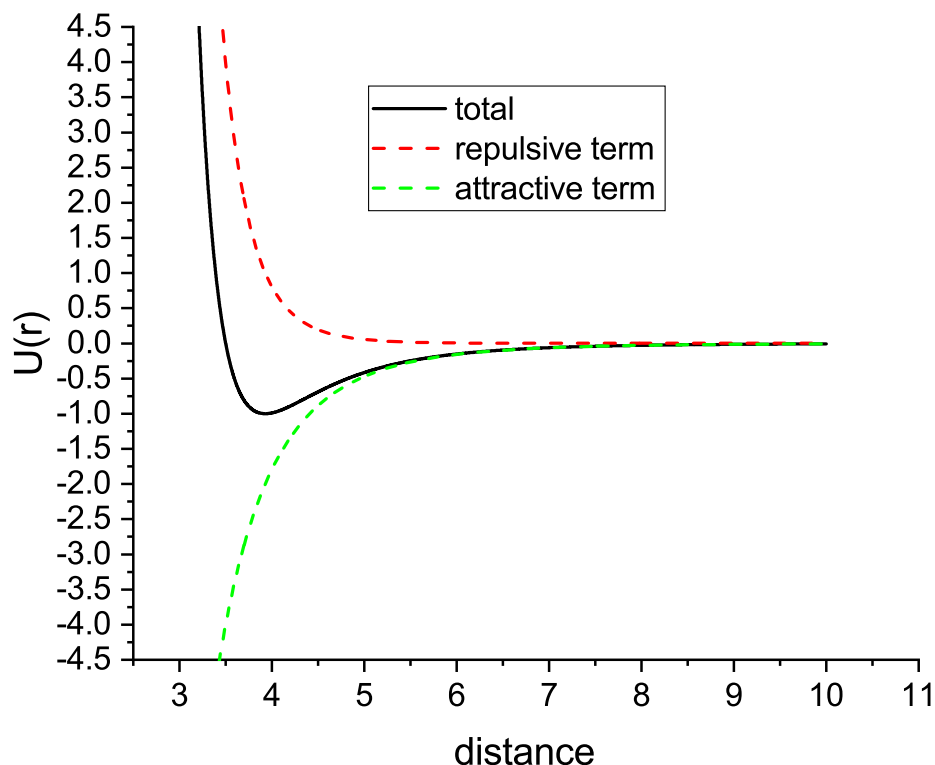


Fig. 6.2. Example of Lennard Jones Potential including the different contributions.

by explicit solvent atoms. Typically in literature, the boundary condition, notated by the dashed lines is periodic.  $\lambda$  is the coupling parameter and is a combination of the Coulomb and Lennard-Jones potential. The structure will also change due to the change in  $\lambda$ .

### 6.3 Hybrid Methods

As the name implies hybrid methods combine implicit and explicit methods in order to improve the quality of the result. The explicit system includes the active

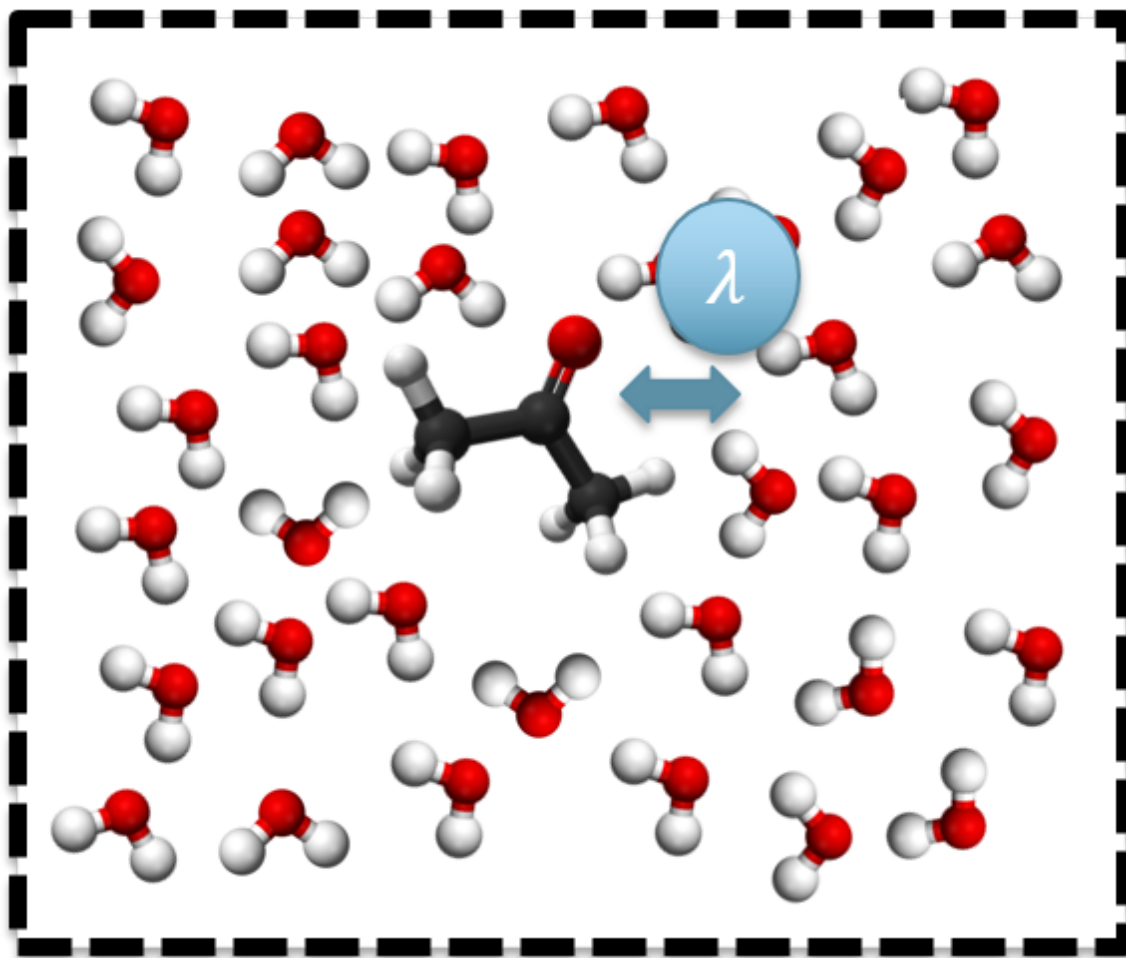


Fig. 6.3. A schematic of the structure in the explicit solvent method. Acetone is surrounded by water. The dashed line represents the mathematical boundary conditions.

ingredient and a small solvation shell. The rest of the solvation is included either implicitly or with a lower level of rigor.

### QM/MM

This method uses a quantum mechanical calculation for the active ingredient and perhaps a few solvent molecules and more classical methods such as molecule me-



chanics / dynamics for the solvent molecules further away from the active ingredient. Lastly, the outermost layer is considered implicit if considered at all. As done in the implicit solvent methods, the potential energy is decomposed in to different components.

$$V_{total} = V_{classical} + V_{quantum} + V_{interaction} \quad (6.10)$$

The first term  $V_{classical}$  can be solved with molecular dynamics as is routinely done and includes stretching, torsion, angle, and bonding terms. Also, the second term  $V_{quantum}$  is solved straightforwardly using quantum mechanical methods such as DFT. The third term  $V_{interaction}$  is the potential energy that couples the quantum mechanical domain to the classical domain and deserves some discussion. This interaction terms gives the contribution of the classical (point-like) charges on to the quantum mechanical charges. The derivation for the first interaction model can be found in the original paper for QM/MM [92].

There are two main ideas for how to handle the interaction between the quantum mechanical atoms and the classical atoms: the subtractive QM/MM and the additive QM/MM [93].

The first method, the subtractive QM/MM, the first method ONIOM (our own n-layered integrated molecular orbital and molecular mechanics) has a simple intuitive reasoning. The interaction energy between the QM and the MM region is composed of the calculation of the QM region with QM method, the calculation of the full system with the MM method, and the calculation of the QM region with the MM method. However, this method has some drawbacks. One drawback is that charge transfer between the MM and the QM is not accurate due to the absense of polarization. Polarization is absent because the two regions do not see each other if they are calculate separately.

The second method, the additive QM/MM, avoids these drawbacks by including both the QM and the MM region when calculating the potential between two. An

explicit coupling is included between the two regions at different levels of theory. An overview of different approaches, can be found in [94].

## 7. HAMILTONIAN - DESCRIPTION OF THE SYSTEM

### 7.1 Overview of Different Tight-Binding Theories

Semiconductor and crystalline materials have seen much success with empirical tight-binding methods. Even first nearest-neighbor orthogonal tight-binding has shown to be useful in many applications. Chapter 3 shows results using orthogonal tight-binding theory. However in these calculations, charge transfer is not captured and its utility is limited by this constraint. Additionally, tight-binding parametrization is an optimization process, therefore targets are needed. These targets can be anything that describe the system accurately. Typically, the target for parametrization is a higher level of theory such as density functional theory. An example result from an optimization procedure is shown in 7.1. The system is copper with the Fermi level denoted with a solid red line. Since this is a metallic system, the bands near the Fermi level and below should be captured accurately. The tight-binding method of Hegde and co-workers is used as in ref. [95]. For semiconductor systems, the bands around the Fermi level are most important. These characteristics can be reflected in the optimization routine with using a fitting function with different weights for different bands.

For the systems of interest in this work – active ingredients in a liquid systems, a better description of the charge transfer is necessary. Empirical Tight-binding parameters are typically calculated for homogeneous systems, i.e. the active ingredient and the liquid system treated separately. A more accurate empirical tight-binding model would include both the active ingredient and the liquid system combined in the parametrization. There are several methods that could be used. One method that has seen some success that promises more transferability is the Extended Huckel Tight-Binding method developed first by [96]. The extended Huckel method is described

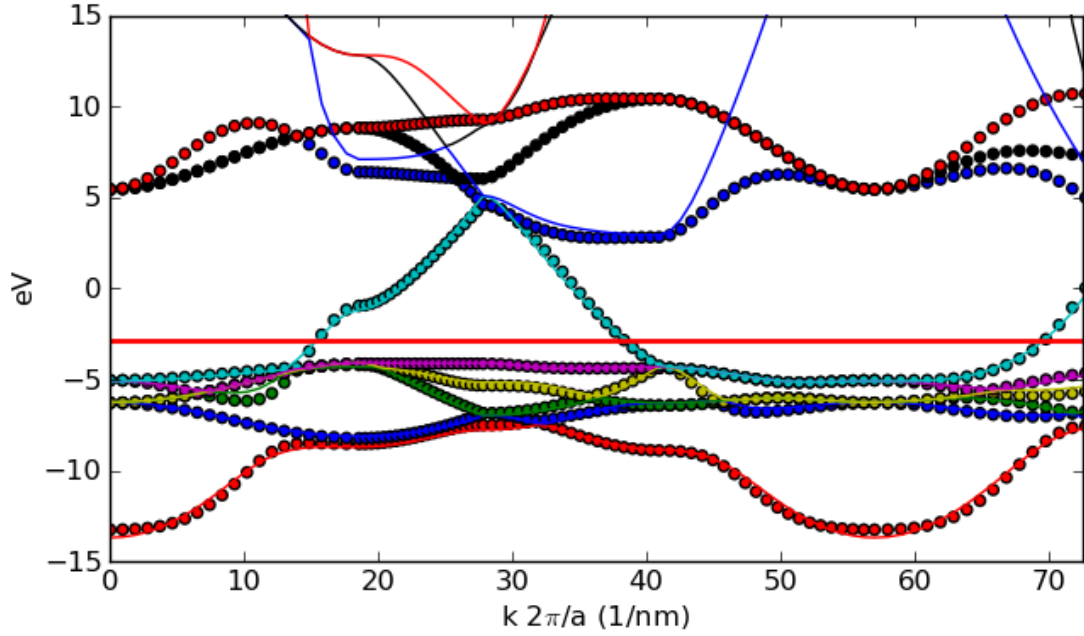


Fig. 7.1. Comparison between density functional theory (solid lines) and tight-binding (open circles) for bulk Copper. The Fermi level is denoted with a solid red line. The bands are each colored with a different color to guide the eye.

an a nonorthogonal basis. The onsite elements of the Hamiltonian are parametrized and have a physical meaning. They are the difference between the ionization potential and the affinity of the electron. The off-diagonal element is calculated as an average between the on-site Hamiltonian elements weighted by the calculated overlap elements. An additional parameter is included in the off-diagonal element calculation but typically  $K_{EHT}$  is set to 1.75 and is not adjusted.

$$H_{ij} = \frac{1}{2} K_{EHT} S_{ij} (H_{ii} + H_{jj}) \quad (7.1)$$

The overlap is calculated based off a parameterized Slater-type orbital. The radial and the angular part  $R$  and  $Y$ , respectively. The radial part is described:

with parameters  $C_1$ ,  $C_2$ , and  $\eta_1$  and  $\eta_2$ .

$$R_{nl}(r) = \frac{r^{n-1}}{\sqrt{(2n)!}} \left[ C_1 (2\eta_1)^{n+\frac{1}{2}} e^{-\eta_1 r} + C_2 (2\eta_2)^{n+\frac{1}{2}} e^{-\eta_2 r} \right] \quad (7.2)$$

The overlap can then be calculated as:

$$S_{ij} = \int \phi_i^*(\vec{r}) \phi_j(\vec{r}) d^3\vec{r} \quad (7.3)$$

The above equations make up the core of the Extended Huckel theory. This work does not focus on Extended Huckel so more details are not included but only a brief introduction to showcase the different choices available.

On the other side of the spectrum, density functional theory (DFT) has only a few parameters and a parametrization routine is not necessary. But, the transferability of DFT comes with downsides. DFT is orders of magnitude more expensive to calculate relative to orthogonal tight-binding and extended Huckel depending on the functional and basis used. In order to facilitate calculations with larger number of atoms, a density functional tight-binding (DFTB) was created and has been successful in many biological and chemical applications.

### 7.1.1 Density Functional Tight-Binding

For completeness, the derivation of density functional theory tight as outlined in ref. [97] is included. The starting point for any DFTB theory is the Taylor series expansion of the functional around a reference density  $\rho_0$ . In order to facilitate later discussions, the expansion is carried out to third order:

$$E^{3^{rd}}[\rho_0 + \delta\rho] = \frac{1}{2} \sum_{\alpha\beta} \frac{Z_\alpha Z_\beta}{R_{\alpha\beta}} - \frac{1}{2} \iint \frac{\rho(\vec{r}) \rho_0(\vec{r}')}{|\vec{r} - \vec{r}'|} d\vec{r} d\vec{r}' - \int V^{XC}[\rho_0] \rho_0 d\vec{r} + E^{XC}[\rho_0] \quad (7.4)$$

$$+ \sum_i n_i \langle \psi_i^* | \hat{H}[\rho_0] | \psi_i \rangle \quad (7.5)$$

$$+ \frac{1}{2} \iint \left( \frac{1}{|\vec{r} - \vec{r}'|} + \frac{\delta^2 E^{XC}[\rho]}{\delta\rho(\vec{r}) \delta\rho(\vec{r}')} \Big|_{\rho_0} \right) \delta\rho(\vec{r}) \delta\rho(\vec{r}') d\vec{r} d\vec{r}' \quad (7.6)$$

$$+ \frac{1}{6} \iiint \left( \frac{\delta^3 E^{XC}[\rho]}{\delta\rho(\vec{r}) \delta\rho(\vec{r}') \delta\rho(\vec{r}'')} \Big|_{\rho_0} \right) \delta\rho(\vec{r}) \delta\rho(\vec{r}') \delta\rho(\vec{r}'') d\vec{r} d\vec{r}' d\vec{r}'' \quad (7.7)$$

$$= E^0[\rho_0] + E^1[\rho_0, \delta\rho] + E^2[\rho_0, (\delta\rho)^2] + E^3[\rho_0, (\delta\rho)^3] \quad (7.8)$$

A typical basis for the DFTB method is a linear combination of atomic orbitals :

$$\psi_i = \sum_j c_{ji} \phi_j \quad (7.9)$$

In this basis, the general eigenvalue problem becomes:

$$\sum_k c_{ki} (H_{jk}^0 - \epsilon_i S_{jk}) = 0 \quad (7.10)$$

Any of the terms in equation (7.8) that only depend on the reference density  $\rho_0$ , the 0<sup>th</sup> order approximation, can be parametrized. This approximation is a sum of the pair potentials and is given the name repulsive energy.

$$E^0[\rho_0] \approx E_{rep} = \frac{1}{2} \sum_{ab} V_{ab}^{rep} \quad (7.11)$$

The repulsive energy can be parametrized and the target is typically more sophisticated DFT or empirical. This parametrization of the reference density,  $\rho_0$ , leads to transferable parameters that can be read-in and used for different systems.

The additional term that makes up the DFTB1 theory in equation (7.8) is

$$\sum_i n_i \langle \psi_i^* | \hat{H}[\rho_0] | \psi_i \rangle = \sum_i n_i \epsilon_i \quad (7.12)$$

i.e. the eigenvalues of the Hamiltonian weighted by the occupancy factors. Combining the two terms leads to:

$$E^{DFTB1} = E^0[\rho_0] + E^1[\rho_0, \delta\rho] = \frac{1}{2} \sum_{ab} V_{ab}^{rep} + \sum_i n_i \epsilon_i \quad (7.13)$$

From equation (7.13), we can see that the DFTB1 theory is non-self-consistent. Without the self-consistency charge transfer is not captured properly and DFTB1 is not appropriate for systems where the charge transfer is important.

As mentioned above DFTB1 is not appropriate when charge transfer is necessary for an accurate description. To overcome this, the DFTB1 theory foundation was built upon. The density fluctuations for the total system are linear combinations of the density fluctuations on each atom.

Also, in order to prepare for useful parametrizations, the density fluctuations are written as:

$$\delta\rho_a = \Delta q_a \frac{\tau_a^3}{8\pi} e^{-\tau_a |\vec{r} - \vec{R}_a|} \quad (7.14)$$

The 2<sup>nd</sup> order contributions are:

$$\frac{1}{2} \iint \left( \frac{1}{|\vec{r} - \vec{r}'|} + \frac{\delta^2 E^{XC}[\rho]}{\delta\rho(\vec{r}) \delta\rho(\vec{r}')} \Big|_{\rho_0} \right) \delta\rho(\vec{r}) \delta\rho(\vec{r}') d\vec{r} d\vec{r}' \quad (7.15)$$

The first term by inserting equation (7.14) becomes

$$\frac{1}{2} \sum_{ab} \left( \frac{1}{|\vec{r} - \vec{r}'|} \right) \Delta q_a \frac{\tau_a^3}{8\pi} e^{-\tau_a |\vec{r} - \vec{R}_a|} \Delta q_b \frac{\tau_b^3}{8\pi} e^{-\tau_b |\vec{r}' - \vec{R}_b|} d\vec{r} d\vec{r}' \quad (7.16)$$

Collecting all terms with  $\tau_a$ ,  $\tau_b$ , and  $R_{ab}$  into a function

$$\gamma_{ab}(\tau_a, \tau_b, R_{ab}) \quad (7.17)$$

The 2<sup>nd</sup> order contribution is then written as

$$E^2(\tau_a, \tau_b, R_{ab}) = \frac{1}{2} \sum_{ab} \Delta q_a \Delta q_b \gamma_{ab}(\tau_a, \tau_b, R_{ab}) \quad (7.18)$$

The  $\gamma$  term at short distances describes the exchange-correlation terms and the electron-electron interaction terms. At longer distances (not intra-atom) the  $\gamma$  term describes the Coulomb-potential. The parameters  $\tau_a$  and  $\tau_b$  are chosen to describe the parametrized Hubbard term, i.e. the chemical hardness. This chemical hardness has physical intuition and can be calculated from DFT. Modified forms of  $\gamma$  also exist that better describe the interaction between hydrogen and another atom.

For the  $3^{rd}$  order DFTB (DFTB3) additional parameters are added. One such parameter is the derivative of the chemical hardness. Similar to what was done for DFTB2 with the  $\gamma$  function the delta charge is given the same form. The derivative of the delta charge is then functionalized with the  $\Gamma$  function. In summary the  $3^{rd}$  order DFTB (DFTB3) is written, with  $a$  and  $b$  as the atom indices and  $i, j, k$  as the orbital indices.

$$E^{DFTB3} = \sum_{iab} \sum_j \sum_k n_i c_{ji} c_{ki} H_{jk}^0 + \frac{1}{2} \sum_{ab} \Delta q_a \Delta q_b \gamma_{ab} + \frac{1}{3} \sum_{ab} \Delta q_a^2 \Delta q_b \Gamma_{ab} + \frac{1}{2} \sum_{ab} V_{ab}^{rep} \quad (7.19)$$

The total energy now depends on the density and the density depends on the energies. Thus the  $2^{nd}$  and  $3^{rd}$  order DFTB theories are solved self-consistently. Unless otherwise noted, the results in thesis use the software DFTB+ [98] with DFTB3 [99]. As commonly done in DFT, the energy is minimized by relaxing the atomic structure. In order to do that, the forces for each atom must also be calculated. The forces is calculated as the derivative of the total energy with respect to the atomic coordinates  $R$ . A detailed derivation can be found in the supporting information of [99]. For



reference, the result is shown here. The atom index is  $k$  and the Cartesian coordinate is  $x$  corresponding to Cartesian  $x, y, z$ .

$$\begin{aligned}
F_{kx} = & - \sum_{a \neq k} \sum_{\mu \in a} \sum_{\nu \in b} n_i c_{\mu i} c_{\nu i} \left( 2 \frac{\partial H_{\mu\nu}^0}{\partial R_{kx}} - 2 \epsilon_i \frac{\partial S_{\mu\nu}}{\partial R_{kx}} + \frac{\partial S_{\mu\nu}}{\partial R_{kx}} \left( \sum_c \Delta q_c \left( \gamma_{ac} + \gamma_{kc} + \frac{1}{3} (2 \Delta q_a \Gamma_{ac} \right. \right. \right. \\
& \left. \left. \left. + 2 \Delta q_k \Gamma_{kc} + \Delta q_c \Gamma_{ck} \right) \right) \right) - \Delta q_k \sum_{a \neq k} \Delta q_a \frac{\partial \gamma_{ak}}{\partial R_{kx}} \\
& - \frac{1}{3} \Delta q_k \sum_{a \neq k} \Delta q_a \left( \Delta q_a \frac{\partial \Gamma_{ak}}{\partial R_{kx}} + \Delta q_k \frac{\partial \Gamma_{ka}}{\partial R_{kx}} \right) - \frac{\partial E^{rep}}{\partial R_{kx}} \tag{7.20}
\end{aligned}$$

## 7.2 DFTB Bandstructure and Density of States

This section shows results from a DFTB calculation using DFTB+ [98] and the mio parameters of ref. [97]. The system is bulk crystalline TiO. The bandstructure is shown in fig. 7.2 and the density of states are shown in fig. 7.3. The partial density of states shows that the valence band is mostly made of P-type orbitals of the oxygen whereas the conduction band is mostly made up of the D-type orbitals of the titanium.

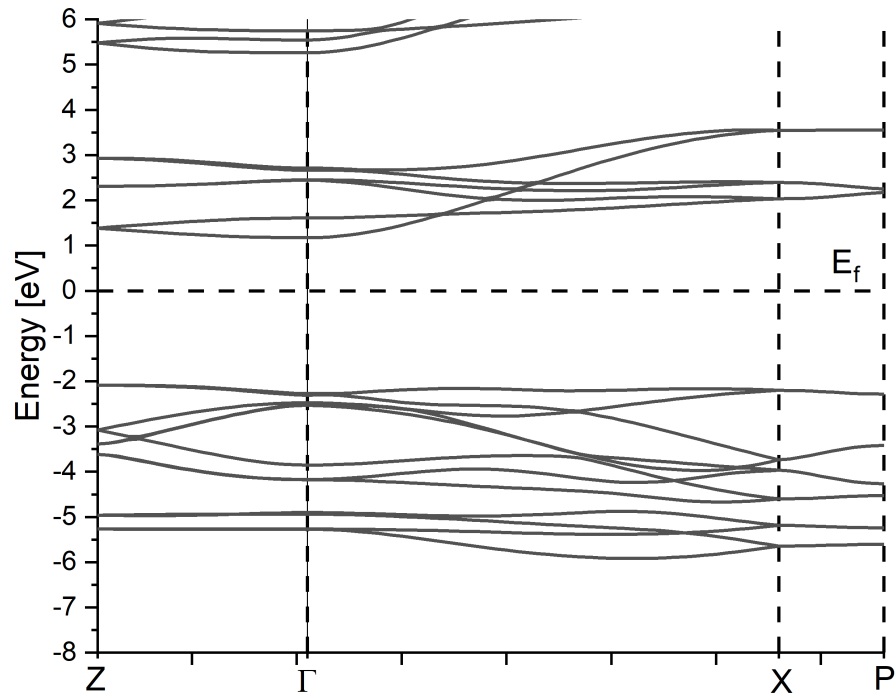


Fig. 7.2. Bulk bandstructure of TiO. The fermi level is marked with a horizontal dash line and the points of high symmetry are marked with vertical dashed lines.

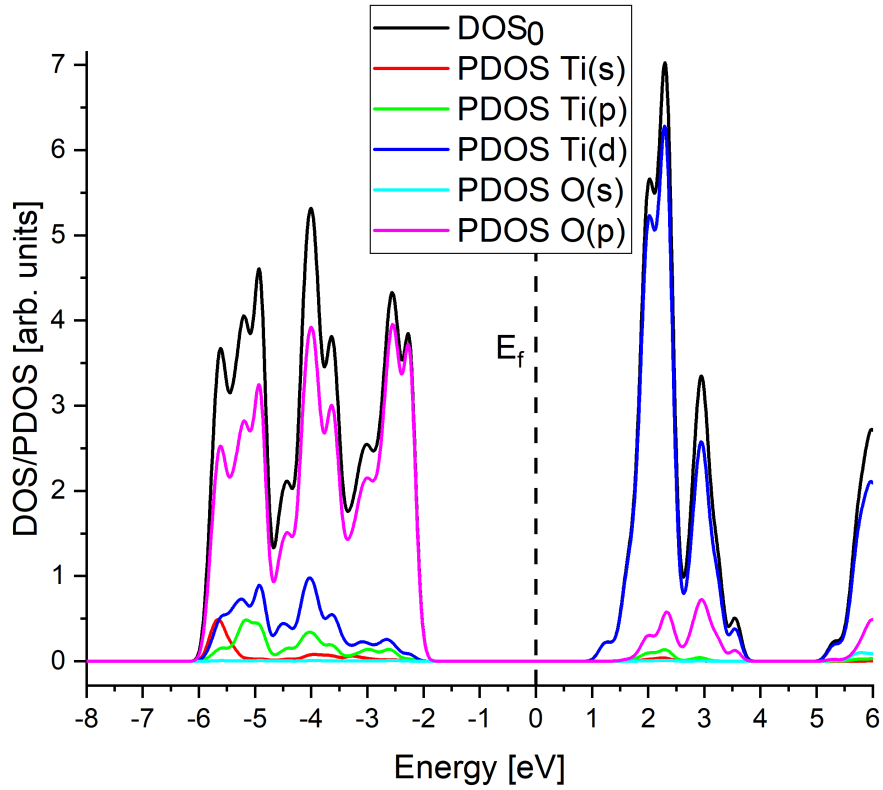


Fig. 7.3. The Density of States of TiO. The fermi level is marked with a horizontal dash line. The local density of states on each atom for each orbital is also shown.

## 8. NON-EQUILIBRIUM GREEN'S FUNCTION OPEN BOUNDARY CONDITION SOLUTION METHODS

### Introduction

In this section different numerical methods for calculating the open boundary conditions of the NEGF equation will be introduced. A unique and quite powerful property of NEGF is a consistent description of the open boundaries. Additionally the limitations of each of the methods will be discussed in order to set up for later chapters.

#### 8.1 Sancho Rubio

The Sancho Rubio method [100] is an iterative approach to solve for the surface Green's function and ultimately the Self-energy that is inserted into the device NEGF equations. Any iterative approach starts with the direct solution of the equations:

$$g_i^R = (E - H - \Sigma_i^R)^{-1} \quad (8.1)$$

$$\Sigma_i^R = H_{i,i-1} g_{i-1,i-1} H_{i-i,i} \quad (8.2)$$

A direction solution of these equations has a problem though. If these equations are solved iteratively as they are, they converge to the solution linearly. It would take many iterations in order to have a converged solution. Sancho and Rubio noticed this and reformulated the problem in order that the solution can be reached exponentially. In effect,  $i$  iterations represents  $2^i$  layers. The main equations that encompass this idea are:

$$\alpha_i = \alpha_{i-1} (ES - \epsilon_{i-1})^{-1} \alpha_{i-1} \quad (8.3)$$

$$\beta_i = \beta_{i-1} (ES - \epsilon_{i-1})^{-1} \beta_{i-1} \quad (8.4)$$

$$\epsilon_i = \epsilon_{i-1} + \alpha_{i-1} (ES - \epsilon_{i-1})^{-1} \beta_{i-1} + \beta_{i-1} (ES - \epsilon_{i-1})^{-1} \alpha_{i-1} \quad (8.5)$$

The derivation of the equations can be found in the original paper [100]. The main idea is to insert the explicit form of  $g^R$  for the  $i^{th}$  iteration. With this explicit insertion. The first  $i^{th} - 1$  iterations can be skipped. The convergence criterion is when the terms  $\alpha$  and  $\beta$  tend towards zero matrices. Once this criterion is met, the surface Green's function can be calculated as:

$$g_{surface}^R = \left( E - \epsilon_i^{surface} \right)^{-1} \quad (8.6)$$

$$\epsilon_i^{surface} = \epsilon_{i-1}^{surface} + \alpha_{i-1} (E - \epsilon_{i-1})^{-1} \beta_{i-1} \quad (8.7)$$

Since 8.7 depends on previous iterations it must also be calculated iteratively. The surface Green's function is then calculated with eq. 8.6 and the open boundary condition problem is solved. For stability and to avoid singularities, an imaginary part  $i\eta$  is often added to the recursive equations. The Sancho-Rubio recursive algorithm assumes that the leads are ideal and infinite. From the equations, it is easy to see that each of the layers need to be the same size. When these assumptions are met, the Sancho-Rubio is obviously more efficient than an iterative calculation of equations 8.1 and 8.2.

## 8.2 Transfer Matrix

Another choice for the calculation of the open-boundary condition stems from scattering matrix theory [101], the infinite, ideal wire is rooted in the assumptions.

The starting point is the scattering wavefunction and the solution of the band structure for an ideal infinite nanowire.

$$(E - H_{i,i} + H_{i,i+1}e^{ik_n(E)\Delta} + H_{i,i-1}e^{-ik_n(E)\Delta}) \phi_{i,n}(R_S, E) = 0 \quad (8.8)$$

where  $R_S$  is the position,  $E$  is the energy, and  $\Delta$  is the slab width. Note that if the wire was not infinite, the right hand side would not be 0. Also note, that energy  $E$  is an input in the open boundary condition problem and  $k_n$  is the sought-after value. This is different than a normal band structure calculation in which the eigenvalues are calculated at given wavevectors  $k$ .

Typical calculations reformulates eq. 8.8 into a generalized eigenvalue problem.

$$\begin{bmatrix} E - H_{ii} & H_{i,i+1} \\ 1 & 0 \end{bmatrix} \begin{bmatrix} \phi_i \\ \phi_{i+1} \end{bmatrix} = e^{ik\Delta} \begin{bmatrix} -H_{i,i-1} & 0 \\ 0 & 1 \end{bmatrix} \begin{bmatrix} \phi_i \\ \phi_{i+1} \end{bmatrix} \quad (8.9)$$

A more efficient method is found in [101] which transforms the generalized eigenvalue problem into a normal eigenvalue problem. Additionally with this transformation, the problem can be reduced from a unit cell basis to an atomic basis. For the [100] crystal direction this means a reduction of the number of atoms by 1/4. To prepare for the transformation into the normal eigenvalue problem, the band structure problem of equation 8.8 is written atomic layer component wise. The result is a normal eigenvalue problem of the form:

$$M\phi = \lambda\phi \quad (8.10)$$

where M is defined as:

$$M = (H - P)^{-1} P \quad (8.11)$$

H and P is

$$H = \begin{bmatrix} E - H_{00} & H_{01} & 0 & 0 \\ 0 & E - H_{11} & H_{12} & 0 \\ 0 & 0 & E - H_{22} & H_{23} \\ -H_{-10} & 0 & 0 & 0 \end{bmatrix} \quad (8.12)$$

$$P = - \begin{bmatrix} 0 & 0 & 0 & T_{0-1} \\ 0 & 0 & 0 & 0 \\ 0 & 0 & 0 & 0 \\ 0 & 0 & H_{32} & E - H_{33} \end{bmatrix} \quad (8.13)$$

In order to prepare for the next steps,  $M$  is written with atomic layer indices.

$$M = \begin{bmatrix} 0 & 0 & M_{02} & M_{03} \\ 0 & 0 & M_{12} & M_{13} \\ 0 & 0 & M_{22} & M_{23} \\ 0 & 0 & M_{32} & M_{33} \end{bmatrix} \quad (8.14)$$

The eigenvectors for the  $2^{nd}$  and  $3^{rd}$  layer can be found from

$$\begin{bmatrix} M_{22} & M_{23} \\ M_{32} & M_{33} \end{bmatrix} \begin{bmatrix} \phi_2 \\ \phi_3 \end{bmatrix} = \frac{1}{(e^{-ik\Delta} - 1)} \begin{bmatrix} \phi_2 \\ \phi_3 \end{bmatrix} \quad (8.15)$$

Once the eigenvectors for the  $2^{nd}$  and  $3^{rd}$  layers are found, the eigenvectors that give the surface Green's function can be calculated straightforwardly

$$\begin{bmatrix} M_{02} & M_{03} \\ M_{12} & M_{12} \end{bmatrix} \begin{bmatrix} \phi_2 \\ \phi_3 \end{bmatrix} = -\frac{1}{(e^{-ik\Delta} - 1)} \begin{bmatrix} \phi_0 \\ \phi_1 \end{bmatrix} \quad (8.16)$$

The surface Green's function and self-energy can now be calculated from the eigenmodes  $\Phi = \{\phi_0, \phi_1\}^\dagger$ :

$$g_{surface}^R = (\Phi^\dagger (E - H_{00}) \Phi + \Phi^\dagger H_{0-1} \Phi e^{-ik\Delta})^{-1} \quad (8.17)$$

$$\Sigma^R = H_{10} g_{surface}^R H_{01} \quad (8.18)$$

The normal eigenvalue problem has the advantage of being faster and using less memory than the generalized eigenvalue problem. As with the Sancho-Rubio method, the transfer matrix method depends on the assumption that the leads are ideal and infinite.

### 8.3 Scattering in the Leads

To avoid artificial reflections at the device/lead interface, the scattering from the device is propagated into the lead. Only then, the electron density in a homogeneous device in equilibrium stays constant through the device. Figure 8.2 confirms this finding for a simple silicon wire in  $sp^3d^5s^*$  tight-binding basis. Ignoring scattering in the lead yields unphysical bowing of the density across the device in the transport direction. The algorithm used to propagate the scattering in the device into the lead is summarized in figure 8.1.

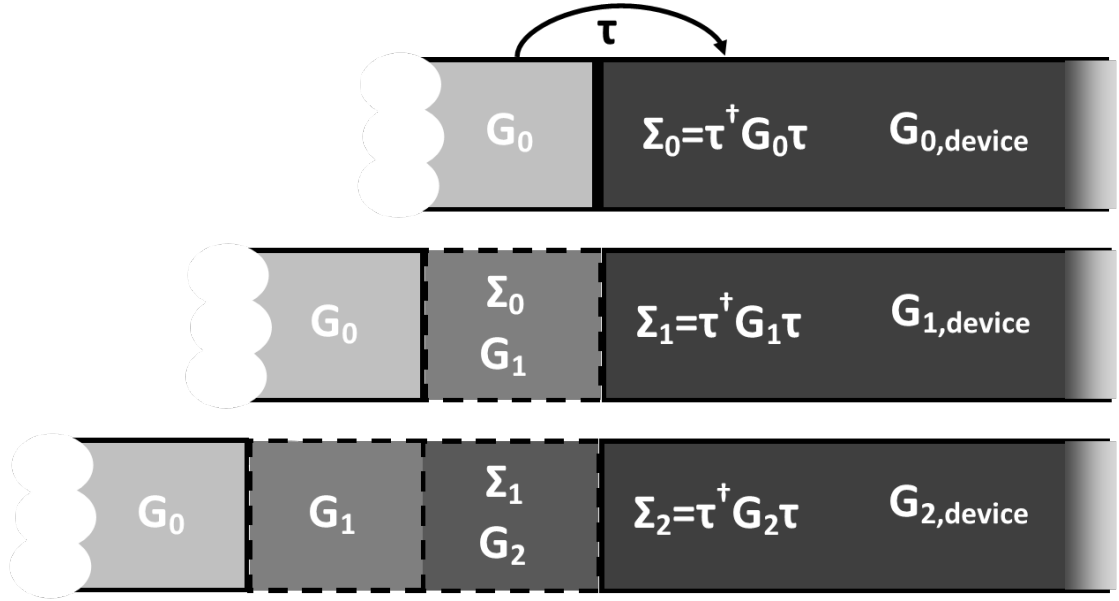


Fig. 8.1. Scattering in the leads algorithm used in all subsequent scattering calculations.

### 8.4 General Leads

The previous two methods, Sancho-Rubio and transfer matrix are derived with the assumptions that the leads are ideal and infinite. In experiment, devices have imperfections, geometrical variations, alloys etc. To include these variations as part



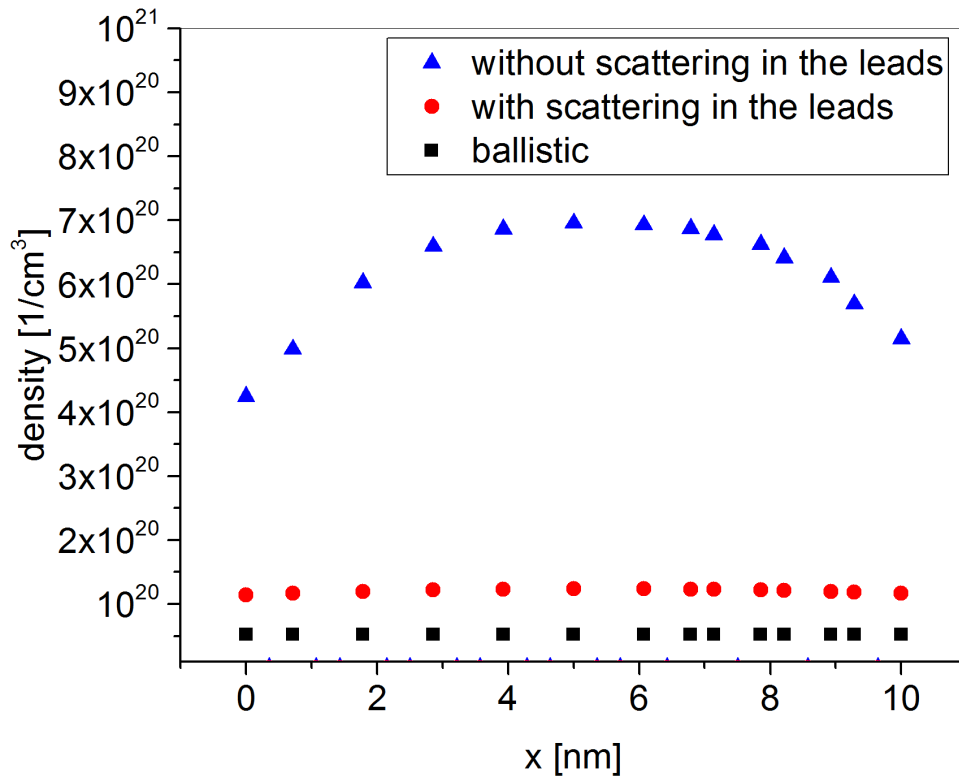


Fig. 8.2. Electron density projected along the transport direction for a simple homogeneous Silicon nanowire of length 10nm and cross section 2nm. Without scattering in the leads, the density is not constant even though the device is effectively infinite. This is caused by artificial reflections due a discontinuous DOS between the lead and device interface.

of the device would easily give devices much too large for modern day computers to solve. Even if they could be included, there would still be an artificial interference wherever the device/lead interface is delineated. The eq. 8.1 and 8.2 could in principle be used but would require too many iterations. The Sancho-Rubio iterations typically take at least 25 iterations. Sancho-Rubio takes advantage of the form of the recursive equations so that each  $i^{th}$  iteration covers  $2^{i^{th}}$  iterations. So if 25 iterations were needed for Sancho-Rubio, an untractable number, 33554432 would be needed. To

avoid this unreasonable number of iterations Yu He and coworkers developed the General Leads Algorithm [102]. The eq. 8.1 and 8.2 are modified with an additional parameter  $i\eta$ . The equations are now solved recursively:

$$g_i = (E + i\eta_i - H_{i,i} - \Sigma_{i,i})^{-1} \quad (8.19)$$

$$\eta_i = \eta_0 e^{-\lambda(i-1)} \quad (8.20)$$

$$\Sigma_{i,i} = H_{i,i-1} g_{i-1,i-1}^R H_{i-1,i} \quad (8.21)$$

The amount of iterations is drastically reduced using this formulation. The  $i\eta$  addition to the calculation of  $g^R$  allows less iterations. Once the iterations are closer to the device the  $i\eta$  dies down and tends towards 0. In practice, approximately 150 atomic layers is enough for convergence of the surface Green's functions. Figure 8.3 shows a result from [103] where general leads is used to solve an InGaAs nanowire with explicit random alloy. This example exemplifies what happens with artificial interferences at the device/lead interface for different device lengths. The device length should not effect the transmission if the device is infinite with alloy everywhere. With the alloy only in the device with only 6nm length, the transmission is significantly higher than when it is 18 nm. When the alloy is everywhere the discrepancy is much lower.

The general leads algorithm will be extended in the next chapter so that the system of interest – an active ingredient surrounded by an infinite solvent can be calculated.

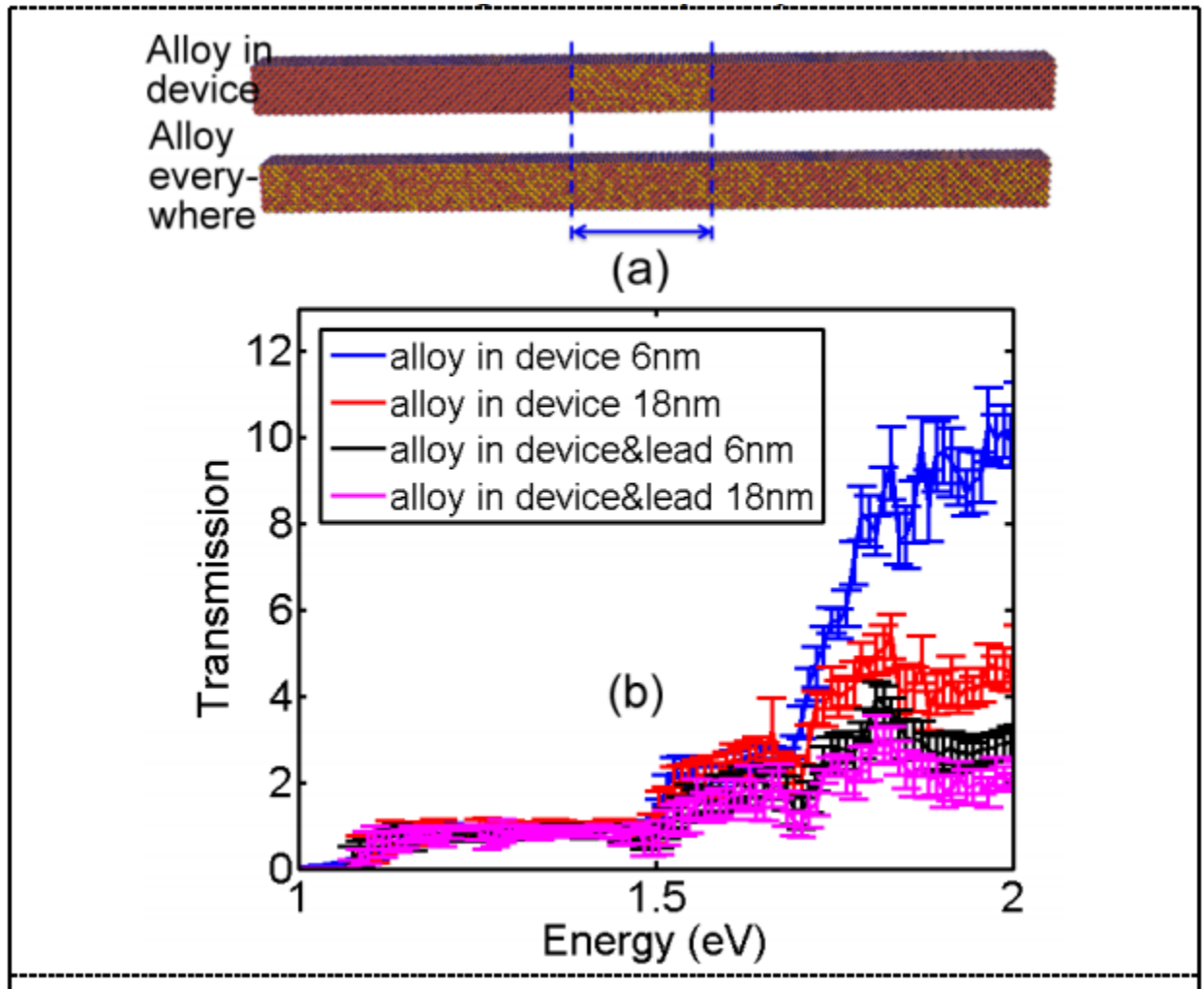


Fig. 8.3. Comparison of ideal leads, InAs, and alloy in the device region and alloy everywhere for an InGaAs nanowire. Figure is obtained from [103].

## 9. EXTENSION OF NON-EQUILIBRIUM GREEN’S FUNCTION FOR ARBITRARY THREE-DIMENSIONAL LIQUID LEADS

### Introduction

In this chapter, the Non-equilibrium Green’s function will be extended for arbitrary three-dimensional leads. Using the work of ref. [102] as a starting point, the active ingredient and solvent system is partitioned into a device and lead. The device includes both the active ingredient and some solvent molecules. The lead includes only the solvent molecules and models the open, infinite system. The device/lead delineation is shown in fig. 9.1.

### 9.1 Verification

Similar to the standard general leads, the dephasing is largest furthest away from the device and is damped exponentially until it tends to zero near the device. As with any new model, careful verification is paramount. In order to verify the extension to arbitrary leads, a simple system of bulk crystalline Silicon is taken. Traditionally, bulk crystalline is solved with periodic boundary conditions in all three directions. For verification, a large sphere of Silicon is taken with a device/lead interface chosen as shown in fig. 9.2. The size of the device does not matter in this case since the system is completely homogeneous. In the next results, the active device is chosen with a 4nm sphere. The environment is infinite Silicon in equilibrium. The first result is the case where the lead calculated is made purposefully too small. As can be seen in fig. 9.3 the 3D Density of States there are large variations of the DOS in the device. This is unphysical and a result of not treating the leads correctly. In

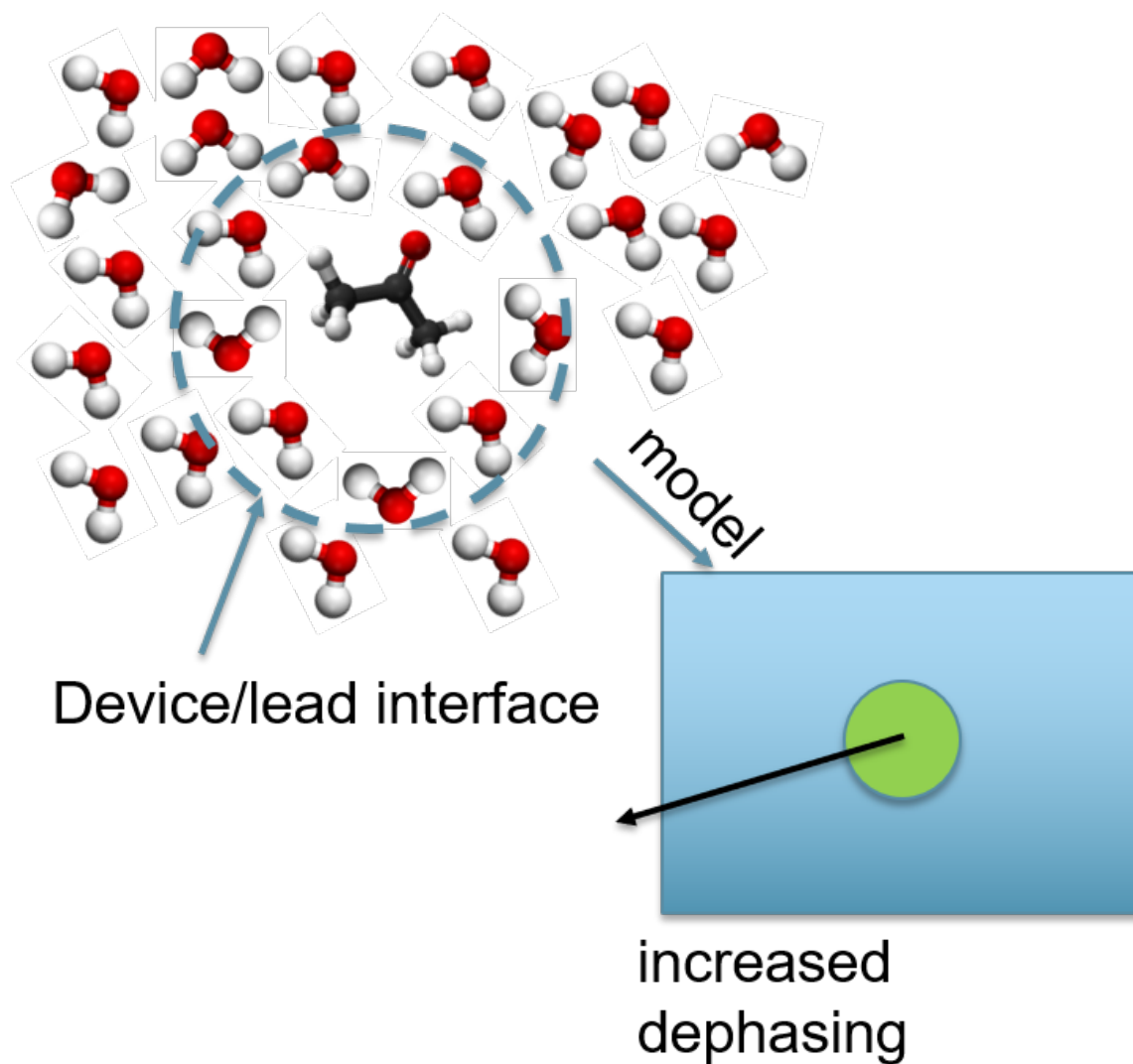


Fig. 9.1. Schematic of the model. The device/lead interface needed for the NEGF algorithm is shown on the left. The model abstraction is shown on the right.

fig. 9.4, the leads are made large enough to minimize variations in the device. The DOS fluctuations in the device are drastically reduced. With an even larger lead, the fluctuations would reduce more but due to memory restrictions, the lead cannot be made larger. Algorithm improvements in order to remove this restriction is the topic of future work. Using the largest lead size that is currently possible, material

properties such as band gap are also calculated from the projected density of states and compared to bulk band structure of Silicon. The band gap in both cases is approximately 1.1 eV.

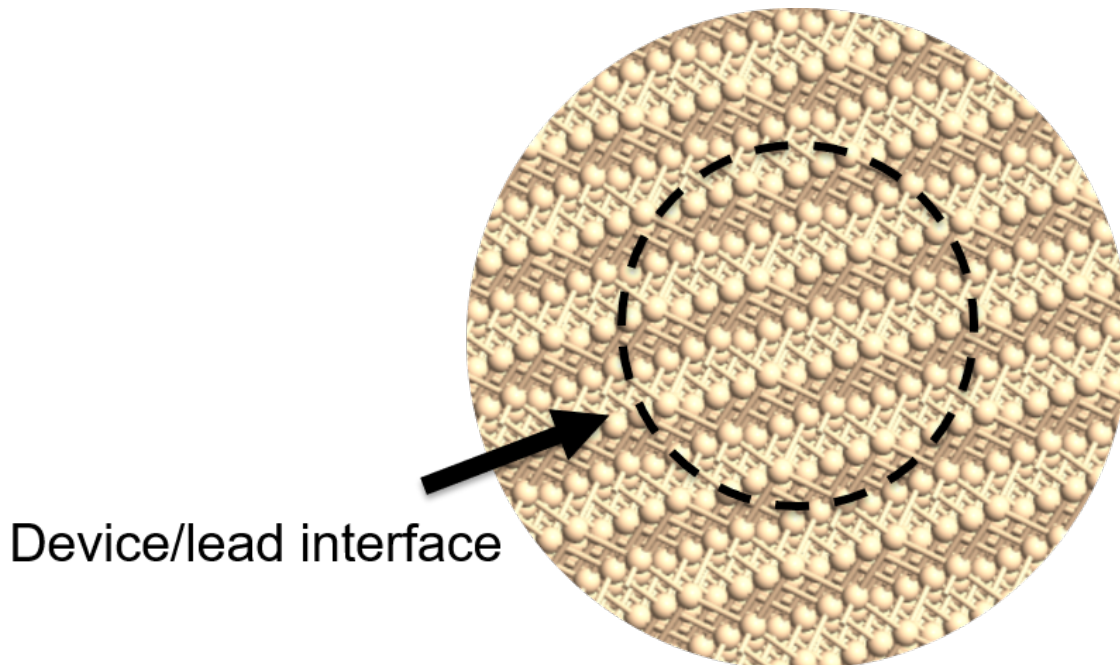


Fig. 9.2. Schematic of the system for verification. A large sphere of Silicon is taken with a device/lead interface chosen.

## 9.2 Nonequilibrium Green's Function with Crystalline Lead Results

The next step after verification is to work towards the system of interest. The end-goal is an active ingredient in a liquid solution. An intermediate step is to treat the solvent as crystalline. Although, a crystalline solvent is not reality when wanting to calculate room temperature solvation energies and solubility, it is a good starting point for testing the method. The first step is to create a box of solvent molecules. Unless otherwise specified, the solvent considered in this work is water. In crystalline form, the majority of ice is crystallized in the ice 1H structure. Thus, the box of ice

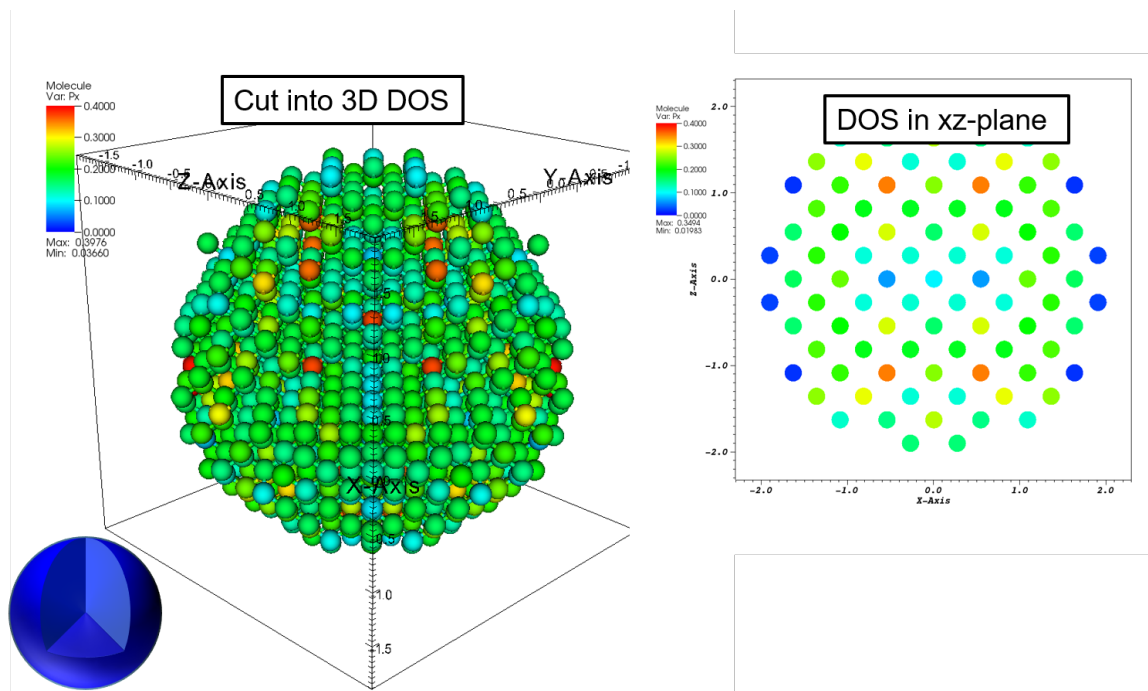


Fig. 9.3. Position-resolved density of states of a sphere of Silicon when the lead is purposefully made too small.

is created using this crystal structure. Once the box of ice is created, the next step is to include the active ingredient. In order to accommodate the insertion of the active ingredient, a cavity, like in the implicit method, is created. A cavity was chosen such that no solvent molecule is closer than 2 angstroms to the active ingredient. This distance was chosen as approximately the van der Waal radii of the constituent atoms.

Once the structure is created, the electronic Hamiltonian, an input to the Non-equilibrium Green's Function, is needed. Density functional theory was chosen to describe the electronic properties. The GGA PBE [104] functional was chosen using Quantum Espresso [38]. Once the DFT problem is solved, a Hamiltonian is created. The Hamiltonian is created using the Wannier localization procedure of ref. [105]. The main constraint is to localize the Hamiltonian onto atoms. This is important for

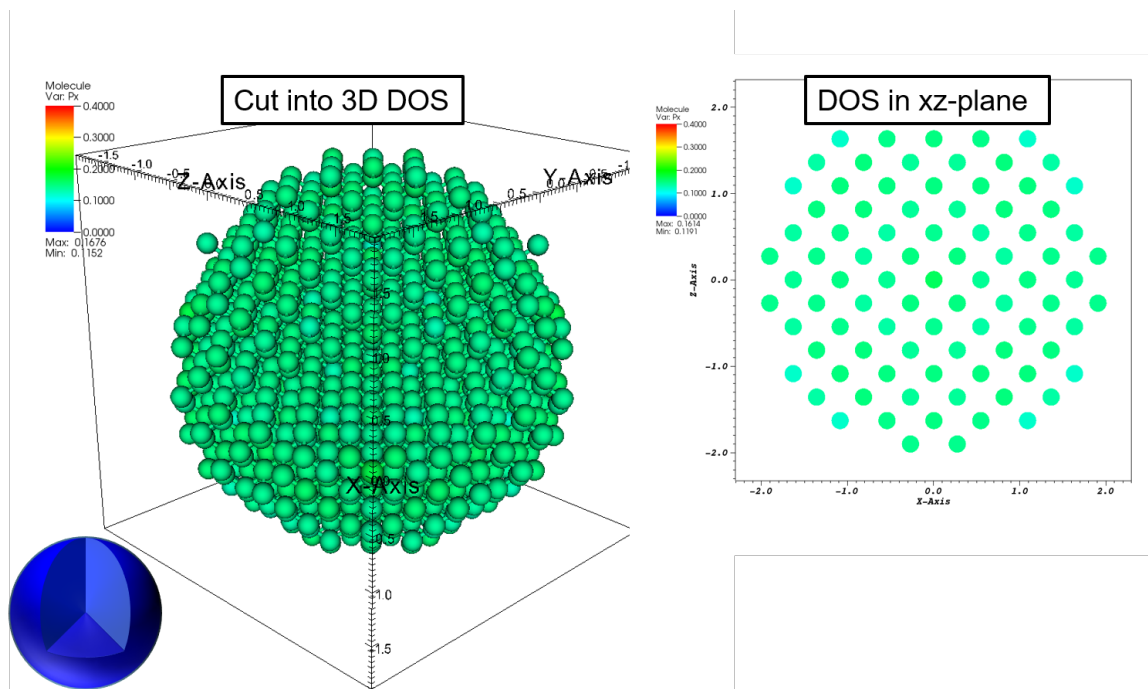


Fig. 9.4. Position-resolved density of states of a sphere of Silicon when the lead is made large enough to reduce variations in the DOS.

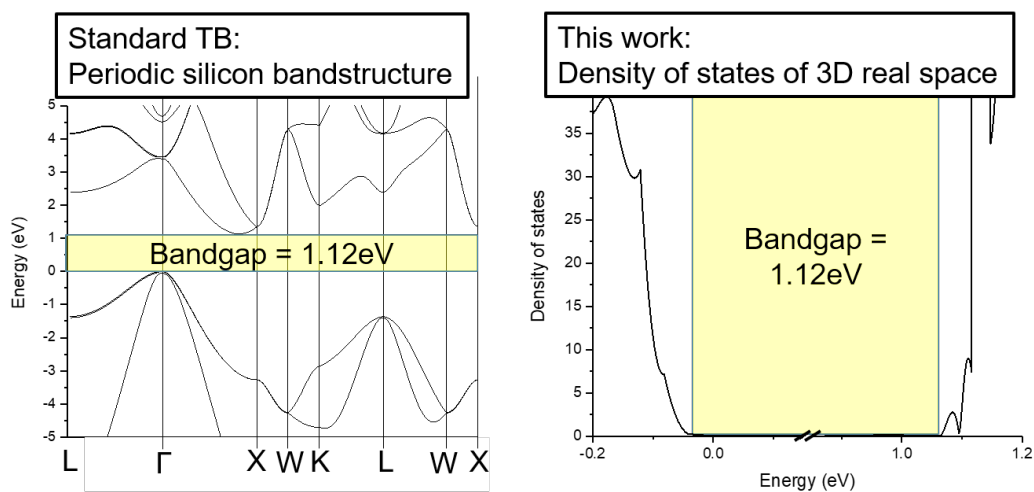


Fig. 9.5. Comparison of band gap calculated from the periodic silicon band structure and the projected 3D density of states.



performance considerations of the NEGF procedure. Once the Hamiltonian is created from the DFT simulation, the Hamiltonian is used as input for NEGF.

NEGF can give spectral results that can be used to help understand the solvation in terms of the spectral broadening and shift. Fig. 9.6 shows the density of states for caffeine in a  $3\text{ nm}^3$  box of water molecules at the LUMO. The coupling strength of the Hamiltonian between the active ingredient and the solvent is varied from 0 (no coupling) to 1 (full coupling). This is done to show how the environment affects the density of states. As can be seen, the no coupling case, gives a sharp peak at the LUMO state. An electron on the active ingredient stays on the active ingredient infinitely (infinite lifetime). As the coupling between the active ingredient and solvent is increased the energy increases and the state broadens. Physically this means that the electron lifetime in the active ingredient is no longer infinite.

### 9.3 Hamiltonian for Liquid Leads

The previous results, with a crystalline solvent, use DFT however using DFT with 1000+ atoms becomes intractable. Additionally, in order to make the solvent liquid, energy relaxation is necessary. With liquid solvents, the number of relaxation steps necessary is an order of magnitude larger than for crystalline. Thus, compromises were made and the DFTB described in chapter 7 was used with the DFTB+ [98] software. The initial structure for the solvent was created using the PACKMOL software [106]. This initial structure was then relaxed using DFTB+. Results of an example calculation of methane embedded in water solvent molecules is shown in fig. 9.7. Atoms are relaxed until the maximum force component was  $1E - 4$  Bohr/Angstrom. As above with DFT, the Hamiltonian was created for use in NEGF. The Hamiltonian in contrast to the crystalline results in DFT, is created without an additional localization procedure. Since DFTB is formed in a tight-binding basis, a Hamiltonian can be constructed straightforwardly. DFTB is non-orthogonal but

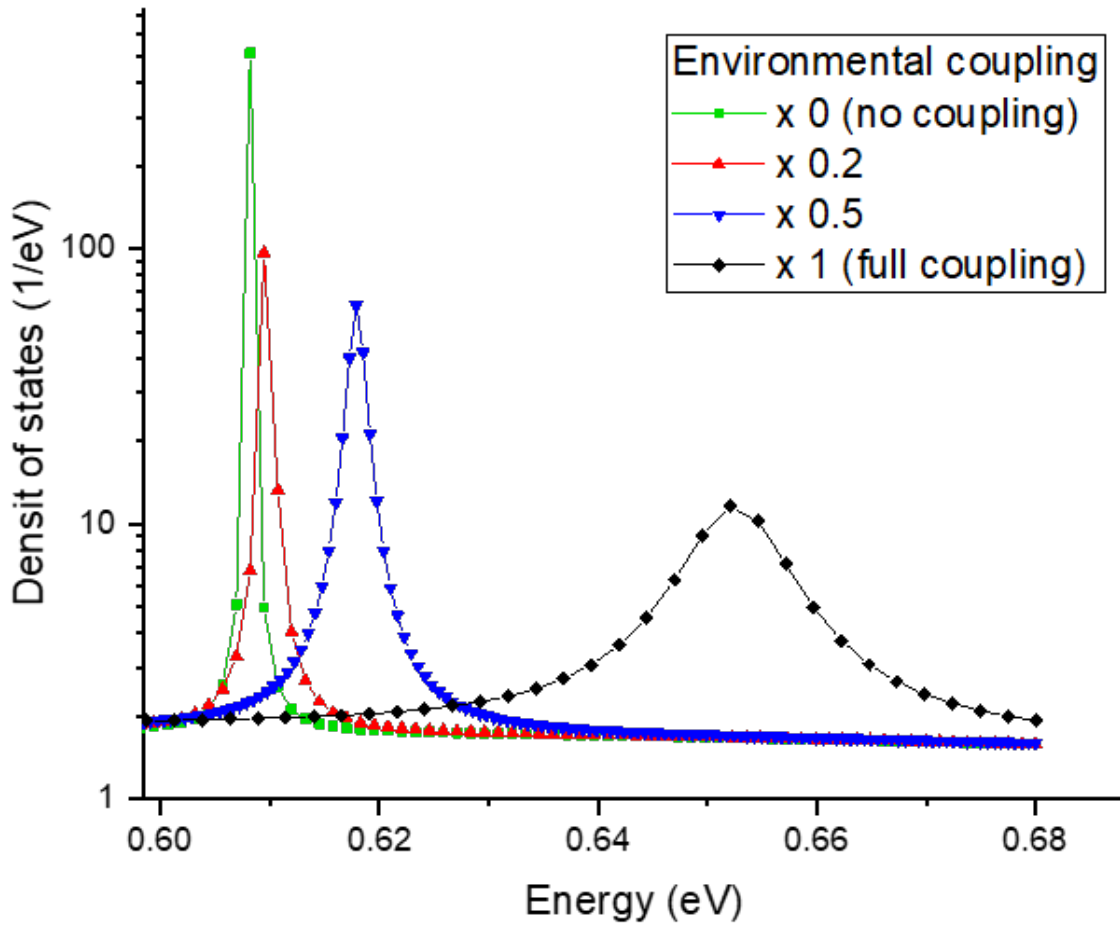


Fig. 9.6. The density of states calculated from NEGF near the LUMO of caffeine. The coupling is varied from 0 (no coupling) to 1 (full coupling).

NEGF can handle non-orthogonal basis' with slight modifications to the equations. The energies are multiplied by the overlap matrix  $S$ .

$$G^R = (ES - H - \Sigma^R)^{-1} \quad (9.1)$$

Additionally, charge populations are assigned to atoms with the Mulliken charge approximation:

$$n_{Mulliken}(\vec{x}) = \int \Im \{diag[trace(G^<(\alpha, \beta, E) S(\alpha, \beta))]\} dE \quad (9.2)$$

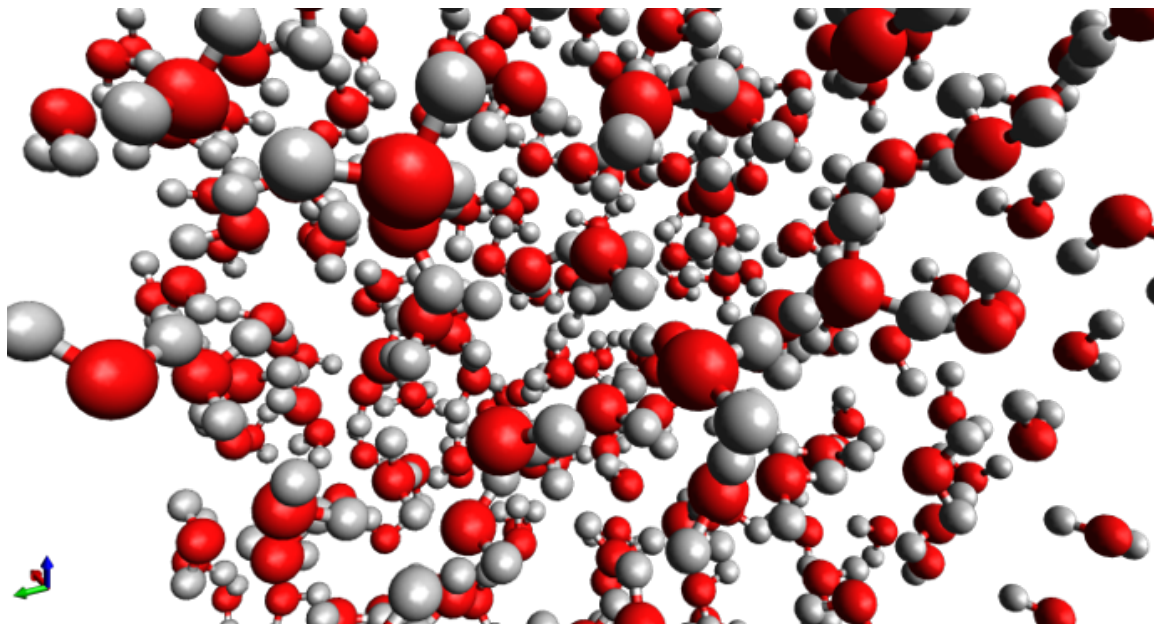


Fig. 9.7. DFTB relaxed structure with methane embedded in water.

## 9.4 Extension of Thermodynamic Integration for Quantum Mechanical Calculations

### Introduction

In order to calculate the solvation energy for an active ingredient in a liquid, the thermodynamic integration discussed in chapter 6 is extended. In the molecular dynamics calculations of Shirts and coworkers [107], the variational coupling parameter,  $\lambda$ , is varied from 0.0 to 1.0.  $\lambda = 0.0$  is the fully coupled case in which the solvent and the active ingredient interaction potentials (Coulomb and Lennard-Jones) have the full strength.  $\lambda = 1.0$  is the case in which they are in the same simulation domain but are not coupled. Due to singularities in the Coulomb and Lennard-Jones potential when atoms are too close together, the two interaction potentials are switched separately and the  $\lambda$  variation calculation has to be done twice. The reason mentioned in this work for the  $\lambda$  calculations are to span more of the configurational space.

Each  $\lambda$  value calculated, simulates a different configuration that is possible during the work done to solvate the active ingredient, i.e. the solvation energy. In the work of Shirts and coworkers [107], the molecular dynamics calculations are done independently for each  $\lambda$  value. As can be imagined, this method can be quite expensive with calculations needing typically 50 separate  $\lambda$  values.

## End-Point Methods for Solvation Energy Calculations

Keeping in mind, the overall goal of this work: to create a fast and accurate method for an explicit quantum-mechanical solvent and active ingredient combination simpler methods were first tested. The simplest method would be calculating only the end points i.e. the fully-coupled and the isolated case. For this calculation, only 3 simulations are necessary, the solvent box, the isolated, gas phase active ingredient, and the combination of the solvent with the active ingredient. The solvation energy is then calculated as:

$$E_{solvation} = (E_{combination}) - (E_{solvent} + E_{AI,gas}) \quad (9.3)$$

Care must be taken so that the energies between the combination and the addition of the solvent and the isolated gas phase do not change too much. The number of solvent atoms must stay the same and most of the solvent atoms, especially the ones further away from the active ingredient must not have large changes in energy. Inherently, the convergence tolerances must be tighter than typical DFT and relaxation calculations.

First tests of this end-point method, were performed on acetone in water. The solvation energy of ref. [108] is -2.91 kcal/mol. This value is calculated using an implicit PCM model with the DFTB method. This reference is used to separate differences between the DFT method and the implicit and explicit methods. Implicit DFT methods give different results but qualitatively are the same, i.e. if DFT predicts solvation, DFTB does also. The acetone solvation energy value for different DFT functionals

of ref. [108] varies from -1.21 to 5.42 kcal/mol. The results of this calculation for the DFTB with explicit solvent gave a result of -414 kcal/mol. This is 140 times too small (prediction of more soluble) than the reference implicit DFTB method. This is an unphysically strong solvation. Attempts were made in order to reduce this value but was not successful with the end-point method. The configurational overlap between the two systems at the end-point is small and thus small changes in energy on each atom add up and give a large value.

Explicit methods such as in ref. [107] discuss this issue and possible solutions. As was discussed above, the improved method increases the configurational space overlap. It allows a smooth transition from the fully coupled state to the isolated state.

## Thermodynamic Integration Methods

In this work, the thermodynamic integration method of ref. [107] is extended to a quantum-mechanical description of the system. In their work, only the non-bonding interaction terms are varied with  $\lambda$ , namely the Coulomb potential and the Lennard-Jones potential. Additionally, they perform a molecular dynamics calculation at each step. Equilibration must be carefully checked for each of the  $\lambda$  calculations.

The goal of this section is to develop an extension that is faster than the molecular dynamics approach. Additionally, this method will include quantum mechanical bonding interaction that are so far neglected in traditional thermodynamic integration methods. The ingredients for a thermodynamic integration method is interaction potentials that can be varied with  $\lambda$  and an output parameter that depends on  $\lambda$  and can be differentiated.

Thermodynamic integrations are best calculated when there is maximum overlap in the configurational space. In order to accommodate,  $\lambda$  configurations in the DFTB-relaxation approach are calculated in serial, i.e. the next  $\lambda$  configuration initial structure is the converged structure of the last calculated  $\lambda$  structure. An-

other advantage of this approach is that if  $\Delta\lambda$ , the steps between  $\lambda$  values, is small and the variation is smooth then less iterations for energy minimization are needed. In practice, an order of magnitude less iterations are sometimes needed where the variations between  $\lambda$ s are minimal. The molecular dynamics thermodynamic integration uses Lennard-Jones potential and the Coulomb potential to vary with  $\lambda$ . This DFTB-relaxation method adds in the bonding interaction terms by also modifying the quantum-mechanical Hamiltonian calculated within the DFTB framework. All DFTB calculations are calculated using DFTB+ [98]. Energy minimization was performed until the maximal force component was 1E-4 eV/angstrom on any atom. The initial structure was created using PACKMOL [106] with the number of atoms to give a mass density of 1.00 g/cm<sup>3</sup>. The solvation energy can be written in terms of the position-resolved total energy at each  $\lambda$  value.

$$\Delta E_{solvation} = \int_0^1 d\lambda \left\langle \frac{dE(\lambda, \vec{x})}{d\lambda} \right\rangle_{\lambda} \quad (9.4)$$

$$\left\langle \frac{dE(\lambda, \vec{x})}{d\lambda} \right\rangle = \frac{\int \frac{dE(\lambda, \vec{x})}{d\lambda} e^{-E(\lambda, \vec{x})/kT} d\vec{x}}{\int e^{-E(\lambda, \vec{x})/kT} d\vec{x}} \quad (9.5)$$

The solvation energy is a sum of the partial contributions of thermodynamically averaged  $\frac{dE}{d\lambda}$ . In order to further illustrate the new method, calculations of both methane and acetone in water are performed. Methane is expected to be poorly soluble in water, whereas acetone is expected to be soluble. This means that for methane  $\frac{dE}{d\lambda} \approx 0$  and for acetone  $\frac{dE}{d\lambda}$  should be negative. The more negative the solvation energy, the more soluble the results. Fig. 9.8 shows  $\frac{dE}{d\lambda}$  for both methane and acetone. Methane's values are flat and approximately 0. Acetone's values are negative for each value of  $\lambda$ .

This DFTB-relaxation method is used as a starting for point for NEGF calculations with liquid leads. The NEGF method needs a Hamiltonian. For this work, the Hamiltonian is taken from periodic calculations with DFTB as an approximation.

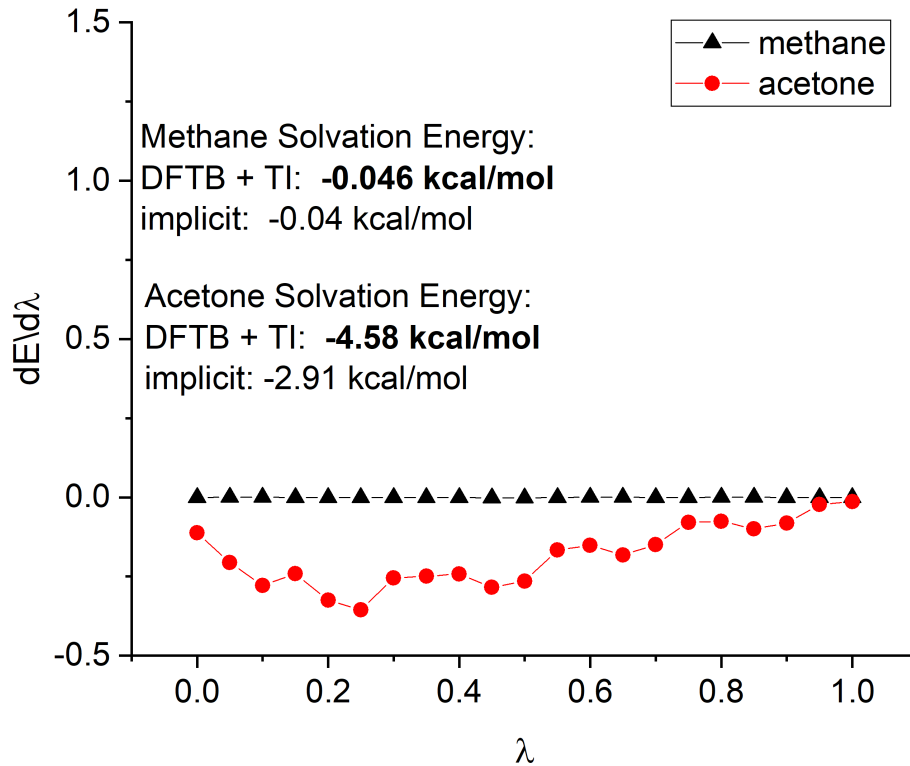


Fig. 9.8.  $\frac{dE}{d\lambda}$  profiles for methane and acetone using the DFTB-relaxed method. Implicit solvent method values are from [108] using DFTB.

## 9.5 Future Outlook

The previous sections introduced the NEGF method in a system in which the NEGF method has not been used until this work. The extension of the general leads to three-dimensional leads has allowed this. These are the first steps and do not utilize the full power of the NEGF method. In actuality, the above results have only touched the surface calculating equilibrium ground-state properties. Additionally, the Hamiltonian is currently calculated with a closed, periodic system approximation. DFT has been coupled with NEGF [109] but only for ideal infinite leads. A solution of the

Hamiltonian with open boundary conditions would allow consistent open calculations of the explicit solvent with an embedded active ingredient.

Future work could include calculating the solvation energy with molecular vibrations. NEGF is suited for this with the self-energy approach with example results shown in chapter 2-4.

The work on solubility has also paved the way for reactivity calculations. Each snapshot of the reactivity process can be treated with the methods developed.



## 10. CONCLUSION

### Summary

This thesis can be broken down into two different parts that at first glance may seem disjoint but in later chapters the connection was made more apparent. Chapter 2 introduced the current state of the art for calculation of transport properties in transistors using the NEGF algorithm. Chapter 3 shows results of using this method for when the approximation of local scattering is made. The next chapter and final chapter of this part, chapter 4, introduces a new method that extends the algorithms used for local scattering to the more realistic treatment with non-local scattering. Transport results were shown for this method in a system that would not previously be possible. Along with detailed analysis of the performance in terms of time and memory.

Chapter 5 and Chapter 6 are devoted to discussing the state of the art of the important question of predicting solvation energies. Two methods, implicit solvent and explicit solvent, are compared. Since the goal of this work is to extend the explicit solvent models to open quantum-mechanical systems, the details of the implicit models are left out with references given for interested readers.

Chapter 7 and 8 discuss the ingredients needed for the prediction of solvation energy in an open-quantum mechanical environment. Chapter 7 introduces the density functional theory tight-binding method with its different levels of sophistication and shows the bandstructure and density of states of a model system - bulk crystalline TiO. Chapter 8 presents different methods for calculation of the contact self-energies needed for transport in NEGF. The first two methods, Sancho-Rubio and transfer matrix, do not allow for infinite ideal leads. The last method, general leads algorithm, allows transport in traditional transistors with a source and drain but the assumption

of ideal, infinite leads is relaxed. This general leads algorithm is a starting point for the next chapter’s method development.

Chapter 9 extends the general leads algorithm to arbitrary three-dimensional leads. Careful verification is undergone using a simple Silicon in tight-binding. The goal of this verification is two-fold. One to improve confidence in the new method and secondly, to illustrate the effects of bad convergence of the lead algorithm. Chapter 9 shows that if the leads are made too small than the lead/device interface will have artificial reflections. Silicon bandstructure properties such as the bandgap are reproduced with the new method.

Chapter 9 continues with demonstrations of an active ingredient in a crystalline solvent. The goal here is to illustrate the spectral properties that are possible from an open, quantum-mechanical description of the system. The density of states shows the broadening of shift near the LUMO of a caffeine molecule for this crystalline system. To calculate the solvation energy, the thermodynamic integration method typically used with molecular dynamics calculations is extended to a quantum-mechanical framework using DFTB with geometry relaxation (energy minimization) for each  $\lambda$  configuration. The Hamiltonian is then used to compare the DFTB-relaxation method of a periodic system with an open-system described with NEGF.

## Future Work

The first part of this thesis lays out a new method that opens doors for simulating quantum systems including non-local scattering using an efficient algorithm. However, this method is still at least an order of magnitude more expensive than a local scattering algorithm. Using the non-local results that are now technically feasible, a local scattering approximation can be developed. The transferability of a local scattering approximation can be assessed. Alternatively, using low rank approximation methods, the NL-RGF algorithm can be made much faster by changing basis.

The second part of this thesis discusses an entirely different problem of calculating the solvation energy for an active ingredient embedded in a solvent. The NEGF method is used to apply open boundary conditions to a typically treated closed system. For this work, the closed, periodic boundary Hamiltonian is assumed transferable to the open system calculation. A better, more consistent solution would be to calculate the Hamiltonian with an open boundary. This has been done before for traditional transport problems but can be extended to the active ingredient-solute system. In this work, only the equilibrium, ground state properties were calculated using NEGF. NEGF also allows for non-equilibrium calculations such as what is currently done in traditional transport problems. NEGF also allows for time-dependent calculations. Non-equilibrium time-dependent calculations would in principle be enough to calculate chemical reactions.

## REFERENCES

## REFERENCES

- [1] S. Datta, “Nanoscale device modeling: the greens function method,” *Superlattices and Microstructures*, vol. 28, no. 4, pp. 253–278, 2000.
- [2] J. Taylor, H. Guo, and J. Wang, “Ab initio modeling of quantum transport properties of molecular electronic devices,” *Physical Review B*, vol. 63, no. 24, p. 245407, 2001.
- [3] S. Sadasivam, Y. Che, Z. Huang, L. Chen, S. Kumar, and T. S. Fisher, “The atomistic greens function method for interfacial phonon transport,” *Ann. Rev. Heat Transfer*, vol. 17, pp. 89–145, 2014.
- [4] S. Steiger, R. G. Veprek, and B. Witzigmann, “Electroluminescence from a quantum-well led using negf,” in *Computational Electronics, 2009. IWCE’09. 13th International Workshop on*. IEEE, 2009, pp. 1–4.
- [5] D. A. Stewart and F. Léonard, “Energy conversion efficiency in nanotube optoelectronics,” *Nano letters*, vol. 5, no. 2, pp. 219–222, 2005.
- [6] J. Schwinger, “Brownian motion of a quantum oscillator,” *Journal of Mathematical Physics*, vol. 2, no. 3, pp. 407–432, 1961.
- [7] L. P. Kadanoff and G. Baym, “Quantum statistical mechanics,” 1962.
- [8] S. Fujita, “Partial self-energy parts of kadanoff-baym,” *Physica*, vol. 30, no. 4, pp. 848–856, 1964.
- [9] S. M. Goodnick, D. K. Ferry, C. Wilmsen, Z. Liliental, D. Fathy, and O. Krivanek, “Surface roughness at the si (100)-sio<sub>2</sub> interface,” *Physical Review B*, vol. 32, no. 12, p. 8171, 1985.
- [10] M. R. Amirzada, A. Tatzel, V. Viereck, and H. Hillmer, “Surface roughness analysis of sio<sub>2</sub> for pecvd, pvd and ibd on different substrates,” *Applied Nanoscience*, pp. 1–8, 2015.
- [11] S. Jin, M. V. Fischetti, and T.-W. Tang, “Modeling of surface-roughness scattering in ultrathin-body soi mosfets,” *Electron Devices, IEEE Transactions on*, vol. 54, no. 9, pp. 2191–2203, 2007.
- [12] S. R. Mehrotra, A. Paul, and G. Klimeck, “Atomistic approach to alloy scattering in sil-xge,” *Applied Physics Letters*, vol. 98, no. 17, p. 173503, 2011.
- [13] A. Esposito, M. Frey, and A. Schenk, “Quantum transport including non-parabolicity and phonon scattering: application to silicon nanowires,” *Journal of computational electronics*, vol. 8, no. 3-4, pp. 336–348, 2009.

- [14] M. Luisier and G. Klimeck, “Atomistic full-band simulations of silicon nanowire transistors: Effects of electron-phonon scattering,” *Physical Review B*, vol. 80, no. 15, p. 155430, 2009.
- [15] M. A. Khayer and R. K. Lake, “Effects of band-tails on the subthreshold characteristics of nanowire band-to-band tunneling transistors,” *Journal of Applied Physics*, vol. 110, no. 7, p. 074508, 2011.
- [16] J. Charles, P. Sarangapani, R. Golizadeh-Mojarad, R. Andrawis, D. Lemus, X. Guo, D. Mejia, J. E. Fonseca, M. Povolotskyi, T. Kubis *et al.*, “Incoherent transport in nemo5: realistic and efficient scattering on phonons,” *Journal of Computational Electronics*, pp. 1–7, 2016.
- [17] S. M. Sze and K. K. Ng, *Physics of semiconductor devices*. John wiley & sons, 2006.
- [18] S. Karpov, “Abc-model for interpretation of internal quantum efficiency and its droop in iii-nitride leds: a review,” *Optical and Quantum Electronics*, vol. 47, no. 6, pp. 1293–1303, 2015.
- [19] W. Scheibenzuber, U. Schwarz, L. Sulmoni, J. Dorsaz, J.-F. Carlin, and N. Grandjean, “Recombination coefficients of gan-based laser diodes,” *Journal of Applied Physics*, vol. 109, no. 9, p. 093106, 2011.
- [20] J. Piprek, “Efficiency droop in nitride-based light-emitting diodes,” *physica status solidi (a)*, vol. 207, no. 10, pp. 2217–2225, 2010.
- [21] M. F. Frasco and N. Chaniotakis, “Semiconductor quantum dots in chemical sensors and biosensors,” *Sensors*, vol. 9, no. 9, pp. 7266–7286, 2009.
- [22] S. Zeng, S. Hu, J. Xia, T. Anderson, X.-Q. Dinh, X.-M. Meng, P. Coquet, and K.-T. Yong, “Graphene–mos 2 hybrid nanostructures enhanced surface plasmon resonance biosensors,” *Sensors and Actuators B: Chemical*, vol. 207, pp. 801–810, 2015.
- [23] T. Ando and Y. Uemura, “Theory of quantum transport in a two-dimensional electron system under magnetic fields. i. characteristics of level broadening and transport under strong fields,” *Journal of the Physical Society of Japan*, vol. 36, no. 4, pp. 959–967, 1974.
- [24] T. Ando, “Screening effect and quantum transport in a silicon inversion layer in strong magnetic fields,” *Journal of the Physical Society of Japan*, vol. 43, no. 5, pp. 1616–1626, 1977.
- [25] T. Kubis and P. Vogl, “Assessment of approximations in nonequilibrium greens function theory,” *Physical Review B*, vol. 83, no. 19, p. 195304, 2011.
- [26] C. Jacoboni and L. Reggiani, “The monte carlo method for the solution of charge transport in semiconductors with applications to covalent materials,” *Reviews of Modern Physics*, vol. 55, no. 3, p. 645, 1983.
- [27] S. Kim, A. Konar, W.-S. Hwang, J. H. Lee, J. Lee, J. Yang, C. Jung, H. Kim, J.-B. Yoo, J.-Y. Choi *et al.*, “High-mobility and low-power thin-film transistors based on multilayer mos2 crystals,” *Nature communications*, vol. 3, p. 1011, 2012.

- [28] Next nano. [Online]. Available: <https://www.nextnano.com>
- [29] T. Kubis, “Quantum transport in semiconductor nanostructures,” Ph.D. dissertation, Verein zur Förderung des Walter Schottky Instituts der Technischen Universität München e.V., Garching, 2009.
- [30] B. C. Doak, R. S. Norton, and M. J. Scanlon, “The ways and means of fragment-based drug design,” *Pharmacology & Therapeutics*, vol. 167, pp. 28–37, 2016.
- [31] E. K. Gross and R. M. Dreizler, *Density functional theory*. Springer Science & Business Media, 2013, vol. 337.
- [32] R. G. Parr and Y. Weitao, *Density-functional theory of atoms and molecules*. Oxford university press, 1994, vol. 16.
- [33] J. J. Klicić, R. A. Friesner, S.-Y. Liu, and W. C. Guida, “Accurate prediction of acidity constants in aqueous solution via density functional theory and self-consistent reaction field methods,” *The Journal of Physical Chemistry A*, vol. 106, no. 7, pp. 1327–1335, 2002.
- [34] C. Liao and M. C. Nicklaus, “Comparison of nine programs predicting p k a values of pharmaceutical substances,” *Journal of chemical information and modeling*, vol. 49, no. 12, pp. 2801–2812, 2009.
- [35] B. Marten, K. Kim, C. Cortis, R. A. Friesner, R. B. Murphy, M. N. Ringnalda, D. Sitkoff, and B. Honig, “New model for calculation of solvation free energies: correction of self-consistent reaction field continuum dielectric theory for short-range hydrogen-bonding effects,” *The Journal of Physical Chemistry*, vol. 100, no. 28, pp. 11 775–11 788, 1996.
- [36] A. Dreuw, J. L. Weisman, and M. Head-Gordon, “Long-range charge-transfer excited states in time-dependent density functional theory require non-local exchange,” *The Journal of chemical physics*, vol. 119, no. 6, pp. 2943–2946, 2003.
- [37] Vasp. [Online]. Available: <https://www.vasp.at>
- [38] Quantum espresso. [Online]. Available: <http://www.quantum-espresso.org/>
- [39] A. C. Van Duin, S. Dasgupta, F. Lorant, and W. A. Goddard, “Reaxff: a reactive force field for hydrocarbons,” *The Journal of Physical Chemistry A*, vol. 105, no. 41, pp. 9396–9409, 2001.
- [40] J. A. Charles, “Efficient inelastic scattering in atomistic tight binding,” Ph.D. dissertation, Purdue University, 2016.
- [41] J.-S. Wang, J. Wang, and J. Lü, “Quantum thermal transport in nanostructures,” *The European Physical Journal B*, vol. 62, no. 4, pp. 381–404, 2008.
- [42] S.-C. Lee and A. Wacker, “Nonequilibrium greens function theory for transport and gain properties of quantum cascade structures,” *Physical Review B*, vol. 66, no. 24, p. 245314, 2002.
- [43] F. J. Dyson, “The radiation theories of tomonaga, schwinger, and feynman,” *Physical Review*, vol. 75, no. 3, p. 486, 1949.

- [44] L. V. Keldysh, “Diagram technique for nonequilibrium processes,” *Sov. Phys. JETP*, vol. 20, no. 4, pp. 1018–1026, 1965.
- [45] G. D. Mahan, *Many-particle physics*. Springer Science & Business Media, 2013.
- [46] A. Wacker, “Semiconductor superlattices: a model system for nonlinear transport,” *Physics Reports*, vol. 357, no. 1, pp. 1–111, 2002.
- [47] J. Bardeen and W. Shockley, “Deformation potentials and mobilities in non-polar crystals,” *Physical Review*, vol. 80, no. 1, p. 72, 1950.
- [48] M. Lundstrom, *Fundamentals of carrier transport*. Cambridge University Press, 2009.
- [49] S. Datta, “A simple kinetic equation for steady-state quantum transport,” *Journal of Physics: Condensed Matter*, vol. 2, no. 40, p. 8023, 1990.
- [50] “Derivation and approximations of the frohlich scattering with polar optical phonons.”
- [51] R. Lake, G. Klimeck, R. C. Bowen, and D. Jovanovic, “Single and multiband modeling of quantum electron transport through layered semiconductor devices,” *Journal of Applied Physics*, vol. 81, no. 12, pp. 7845–7869, 1997.
- [52] M. Anantram, M. S. Lundstrom, and D. E. Nikonov, “Modeling of nanoscale devices,” *Proceedings of the IEEE*, vol. 96, no. 9, pp. 1511–1550, 2008.
- [53] P. Long, J. Huang, M. Povolotskyi, D. Verreck, J. Charles, T. Kubis, G. Klimeck, M. Rodwell, and B. Calhoun, “A tunnel fet design for high-current, 120 mv operation,” in *Electron Devices Meeting (IEDM), 2016 IEEE International*. IEEE, 2016, pp. 30–2.
- [54] P. Long, J. Z. Huang, M. Povolotskyi, G. Klimeck, and M. J. Rodwell, “High-current tunneling fets with (1bar10) orientation and a channel heterojunction,” *IEEE Electron Device Letters*, vol. 37, no. 3, pp. 345–348, 2016.
- [55] A. Svizhenko, M. Anantram, T. Govindan, B. Biegel, and R. Venugopal, “Two-dimensional quantum mechanical modeling of nanotransistors,” *Journal of Applied Physics*, vol. 91, no. 4, pp. 2343–2354, 2002.
- [56] W. Kohn, A. D. Becke, and R. G. Parr, “Density functional theory of electronic structure,” *The Journal of Physical Chemistry*, vol. 100, no. 31, pp. 12 974–12 980, 1996.
- [57] T. Klaver, G. Madsen, and R. Drautz, “A dft study of formation energies of fe–zn–al intermetallics and solutes,” *Intermetallics*, vol. 31, pp. 137–144, 2012.
- [58] M. J. Spencer, A. Hung, I. K. Snook, and I. Yarovsky, “Density functional theory study of the relaxation and energy of iron surfaces,” *Surface Science*, vol. 513, no. 2, pp. 389–398, 2002.
- [59] J. Autschbach and T. Ziegler, “Calculating molecular electric and magnetic properties from time-dependent density functional response theory,” *The Journal of chemical physics*, vol. 116, no. 3, pp. 891–896, 2002.



- [60] L. Sham and M. Schlüter, “Density-functional theory of the energy gap,” *Physical Review Letters*, vol. 51, no. 20, p. 1888, 1983.
- [61] P. Stephens, F. Devlin, C. Chabalowski, and M. J. Frisch, “Ab initio calculation of vibrational absorption and circular dichroism spectra using density functional force fields,” *The Journal of Physical Chemistry*, vol. 98, no. 45, pp. 11 623–11 627, 1994.
- [62] A. K. Mishra, A. Roldan, and N. H. de Leeuw, “A density functional theory study of the adsorption behaviour of co<sub>2</sub> on cu<sub>2</sub>o surfaces,” *The Journal of Chemical Physics*, vol. 145, no. 4, p. 044709, 2016.
- [63] K. Laasonen, M. Sprik, M. Parrinello, and R. Car, “ab initio liquid water,” *The Journal of chemical physics*, vol. 99, no. 11, pp. 9080–9089, 1993.
- [64] J. Winkelmann, U. Brodrecht, and I. Kreft, “Density functional theory: Modelling of surface tensions for molecular fluids,” *Berichte der Bunsengesellschaft für physikalische Chemie*, vol. 98, no. 7, pp. 912–919, 1994.
- [65] A. Pribram-Jones, S. Pittalis, E. Gross, and K. Burke, “Thermal density functional theory in context,” in *Frontiers and Challenges in Warm Dense Matter*. Springer, 2014, pp. 25–60.
- [66] N. D. Mermin, “Thermal properties of the inhomogeneous electron gas,” *Physical Review*, vol. 137, no. 5A, p. A1441, 1965.
- [67] M. C. Dharma-wardana, “Current issues in finite- $t$  density-functional theory and warm-correlated matter,” *Computation*, vol. 4, no. 2, p. 16, 2016.
- [68] F. Furche and R. Ahlrichs, “Adiabatic time-dependent density functional methods for excited state properties,” *The Journal of chemical physics*, vol. 117, no. 16, pp. 7433–7447, 2002.
- [69] S. S. Leang, F. Zahariev, and M. S. Gordon, “Benchmarking the performance of time-dependent density functional methods,” *The Journal of chemical physics*, vol. 136, no. 10, p. 104101, 2012.
- [70] S. Chibani, B. Le Guennic, A. Charaf-Eddin, O. Maury, C. Andraud, and D. Jacquemin, “On the computation of adiabatic energies in aza-boron-dipyrromethene dyes,” *Journal of chemical theory and computation*, vol. 8, no. 9, pp. 3303–3313, 2012.
- [71] A. Dreuw and M. Head-Gordon, “Failure of time-dependent density functional theory for long-range charge-transfer excited states: the zincbacteriochlorin-bacteriochlorin and bacteriochlorophyll- spheroidene complexes,” *Journal of the American Chemical Society*, vol. 126, no. 12, pp. 4007–4016, 2004.
- [72] M. J. Gillan, D. Alfè, and A. Michaelides, “Perspective: How good is dft for water?” *The Journal of chemical physics*, vol. 144, no. 13, p. 130901, 2016.
- [73] Y. Marcus, “Thermodynamics of solvation of ions. part 5. gibbs free energy of hydration at 298.15 k,” *Journal of the Chemical Society, Faraday Transactions*, vol. 87, no. 18, pp. 2995–2999, 1991.

- [74] J. L. McDonagh, D. S. Palmer, T. v. Mourik, and J. B. Mitchell, "Are the sublimation thermodynamics of organic molecules predictable?" *Journal of chemical information and modeling*, vol. 56, no. 11, pp. 2162–2179, 2016.
- [75] C. Cervinka and M. Fulem, "State-of-the-art calculations of sublimation enthalpies for selected molecular crystals and their computational uncertainty," *Journal of chemical theory and computation*, vol. 13, no. 6, pp. 2840–2850, 2017.
- [76] K. Moth-Poulsen and T. Bjørnholm, "Molecular electronics with single molecules in solid-state devices," *Nature nanotechnology*, vol. 4, no. 9, pp. 551–556, 2009.
- [77] J. Tomasi, B. Mennucci, and R. Cammi, "Quantum mechanical continuum solvation models," *Chemical reviews*, vol. 105, no. 8, pp. 2999–3094, 2005.
- [78] Q. Du and G. A. Arteca, "Derivation of fused-sphere molecular surfaces from properties of the electrostatic potential distribution," *Journal of computational chemistry*, vol. 17, no. 10, pp. 1258–1268, 1996.
- [79] A. K. Felts, Y. Harano, E. Gallicchio, and R. M. Levy, "Free energy surfaces of  $\beta$ -hairpin and  $\alpha$ -helical peptides generated by replica exchange molecular dynamics with the agbnp implicit solvent model," *Proteins: Structure, Function, and Bioinformatics*, vol. 56, no. 2, pp. 310–321, 2004.
- [80] M. Feig and C. L. Brooks III, "Recent advances in the development and application of implicit solvent models in biomolecule simulations," *Current opinion in structural biology*, vol. 14, no. 2, pp. 217–224, 2004.
- [81] L. Onsager, "Electric moments of molecules in liquids," *Journal of the American Chemical Society*, vol. 58, no. 8, pp. 1486–1493, 1936.
- [82] M. W. Wong, K. B. Wiberg, and M. J. Frisch, "Ab initio calculation of molar volumes: comparison with experiment and use in solvation models," *Journal of computational chemistry*, vol. 16, no. 3, pp. 385–394, 1995.
- [83] J. Bentley, "Exclusion surfaces for molecules in argon and helium," *The Journal of chemical physics*, vol. 119, no. 11, pp. 5449–5456, 2003.
- [84] B. Mennucci, "Polarizable continuum model," *Wiley Interdisciplinary Reviews: Computational Molecular Science*, vol. 2, no. 3, pp. 386–404, 2012.
- [85] A. Klamt, *COSMO-RS: from quantum chemistry to fluid phase thermodynamics and drug design*. Elsevier, 2005.
- [86] B. Mennucci, M. Cossi, and J. Tomasi, "A theoretical model of solvation in continuum anisotropic dielectrics," *The Journal of chemical physics*, vol. 102, no. 17, pp. 6837–6845, 1995.
- [87] A. Klamt and G. Schüürmann, "Cosmo: a new approach to dielectric screening in solvents with explicit expressions for the screening energy and its gradient," *Journal of the Chemical Society, Perkin Transactions 2*, no. 5, pp. 799–805, 1993.
- [88] A. Klamt, "Conductor-like screening model for real solvents: a new approach to the quantitative calculation of solvation phenomena," *The Journal of Physical Chemistry*, vol. 99, no. 7, pp. 2224–2235, 1995.

- [89] A. Klamt, V. Jonas, T. Bürger, and J. C. Lohrenz, "Refinement and parametrization of cosmo-rs," *The Journal of Physical Chemistry A*, vol. 102, no. 26, pp. 5074–5085, 1998.
- [90] F. Eckert and A. Klamt, "Fast solvent screening via quantum chemistry: Cosmo-rs approach," *AIChE Journal*, vol. 48, no. 2, pp. 369–385, 2002.
- [91] A. Klamt, F. Eckert, and M. Diedenhofen, "Prediction of the free energy of hydration of a challenging set of pesticide-like compounds," *The Journal of Physical Chemistry B*, vol. 113, no. 14, pp. 4508–4510, 2009.
- [92] A. Warshel and M. Levitt, "Theoretical studies of enzymic reactions: dielectric, electrostatic and steric stabilization of the carbonium ion in the reaction of lysozyme," *Journal of molecular biology*, vol. 103, no. 2, pp. 227–249, 1976.
- [93] A. Omer, V. Suryanarayanan, C. Selvaraj, S. K. Singh, and P. Singh, "Explicit drug re-positioning: Predicting novel drug–target interactions of the shelved molecules with qm/mm based approaches," in *Advances in protein chemistry and structural biology*. Elsevier, 2015, vol. 100, pp. 89–112.
- [94] G. Groenhof, "Introduction to qm/mm simulations," in *Biomolecular Simulations*. Springer, 2013, pp. 43–66.
- [95] G. Hegde, M. Povolotskyi, T. Kubis, T. Boykin, and G. Klimeck, "An environment-dependent semi-empirical tight binding model suitable for electron transport in bulk metals, metal alloys, metallic interfaces, and metallic nanostructures. i. model and validation," *Journal of Applied Physics*, vol. 115, no. 12, p. 123703, 2014.
- [96] R. Hoffmann, "An extended hückel theory. i. hydrocarbons," *The Journal of Chemical Physics*, vol. 39, no. 6, pp. 1397–1412, 1963.
- [97] M. Elstner and G. Seifert, "Density functional tight binding," *Phil. Trans. R. Soc. A*, vol. 372, no. 2011, p. 20120483, 2014.
- [98] B. Aradi, B. Hourahine, and T. Frauenheim, "Dftb+, a sparse matrix-based implementation of the dftb method," *The Journal of Physical Chemistry A*, vol. 111, no. 26, pp. 5678–5684, 2007.
- [99] M. Gaus, Q. Cui, and M. Elstner, "Dftb3: extension of the self-consistent-charge density-functional tight-binding method (scc-dftb)," *Journal of chemical theory and computation*, vol. 7, no. 4, pp. 931–948, 2011.
- [100] M. L. Sancho, J. L. Sancho, and J. Rubio, "Quick iterative scheme for the calculation of transfer matrices: application to mo (100)," *Journal of Physics F: Metal Physics*, vol. 14, no. 5, p. 1205, 1984.
- [101] M. Luisier, A. Schenk, W. Fichtner, and G. Klimeck, "Atomistic simulation of nanowires in the s p 3 d 5 s\* tight-binding formalism: From boundary conditions to strain calculations," *Physical Review B*, vol. 74, no. 20, p. 205323, 2006.
- [102] Y. He, Y. Wang, G. Klimeck, and T. Kubis, "Non-equilibrium green's functions method: Non-trivial and disordered leads," *Applied Physics Letters*, vol. 105, no. 21, p. 213502, 2014.

- [103] T. Kubis, Y. He, R. Andrawis, and G. Klimeck, “General retarded contact self-energies in and beyond the non-equilibrium green’s functions method,” in *Journal of Physics: Conference Series*, vol. 696, no. 1. IOP Publishing, 2016, p. 012019.
- [104] J. P. Perdew, K. Burke, and M. Ernzerhof, “Generalized gradient approximation made simple,” *Physical review letters*, vol. 77, no. 18, p. 3865, 1996.
- [105] N. Marzari and D. Vanderbilt, “Maximally localized generalized wannier functions for composite energy bands,” *Physical review B*, vol. 56, no. 20, p. 12847, 1997.
- [106] L. Martínez, R. Andrade, E. G. Birgin, and J. M. Martínez, “Packmol: a package for building initial configurations for molecular dynamics simulations,” *Journal of computational chemistry*, vol. 30, no. 13, pp. 2157–2164, 2009.
- [107] M. R. Shirts, J. W. Pitner, W. C. Swope, and V. S. Pande, “Extremely precise free energy calculations of amino acid side chain analogs: Comparison of common molecular mechanics force fields for proteins,” *The Journal of chemical physics*, vol. 119, no. 11, pp. 5740–5761, 2003.
- [108] V. Barone, I. Carnimeo, and G. Scalmani, “Computational spectroscopy of large systems in solution: The dftb/pcm and td-dftb/pcm approach,” *Journal of chemical theory and computation*, vol. 9, no. 4, pp. 2052–2071, 2013.
- [109] M. Brandbyge, J.-L. Mozos, P. Ordejón, J. Taylor, and K. Stokbro, “Density-functional method for nonequilibrium electron transport,” *Physical Review B*, vol. 65, no. 16, p. 165401, 2002.

## PUBLICATIONS

**Peer-Reviewed Publications**

1. T. Ameen, H. Ilatikhameneh, A. Tankasala, Y. Hsueh, J. Charles, J. Fonseca, M. Povolotskyi, J. Kim, S. Krishna, M. Allen, J. Allen, R. Rahman, G. Klimeck, "Theoretical study of strain-dependent optical absorption in doped Stranski-Krastanov grown InAs/InGaAs/GaAs/AlGaAs quantum dots" Beilstein Journal of Nanotechnology, Thematic Series LightMatter interactions on the nanoscale (2018).
2. J. Geng, P. Sarangapani, K.C. Wang, E. Nelson, B. Browne, C. Wordelman, J. Charles, Y. Chu, T. Kubis, G. Klimeck, Quantitative Multi-Scale, Multi-Physics Quantum Transport Modeling of GaN-Based Light Emitting Diodes, Phys. Status Solidi A, 1700662 (2017)
3. D. Lemus, J. Charles, A. Afzalain, J. Huang, T. Kubis, Mode-space-compatible inelastic scattering in atomistic nonequilibrium Greens function implementations J. Comput. Electron (2017) (submitted).
4. S. Sadasivam, N. Ye, J. P. Feser, J. Charles, K. Miao, T. Kubis, and T. S. Fisher, Thermal transport across metal silicide-silicon interfaces: First-principles calculations and Green's function transport simulation, Phys. Rev. B 95, 085310 (2017)
5. J. Charles, P. Sarangapani, R. Golizadeh-Mojarad, R. Andrawis, D. Lemus, X. Guo, D. Mejia, J. E. Fonseca, M. Povolotskyi, T. Kubis, G. Klimeck, Incoherent transport in NEMO5: realistic and efficient scattering on phonons J Comput Electron (2016).

6. P. Long, J. Z. Huang, M. Povolotskyi, D. Verreck, J. Charles, T. Kubis, G. Klimeck, M. J. W. Rodwell, B. H. Calhoun, A tunnel FET design for high-current, 120mV operation, Electron Devices Meeting (IEDM) (2016)
7. K. Miao, S. Sadasivam, J. Charles, G. Klimeck, T.S. Fisher, T. Kubis, Bttiker probes for dissipative phonon quantum transport in semiconductor nanostructures Applied Physics Letters, 108, 113107 (2016).
8. G. Hedge, M. Povolotskyi, T. Kubis, J. Charles, and G. Klimeck. An environment-dependent semi-empirical tight binding model suitable for electron transport in bulk metals, metal alloys, metallic interface, and metallic nanostructures II Application Effect of quantum confinement and homogeneous strain on Cu conductance.. (2014).
9. J. Charles, M. Cahay, R.S. Newrock. Intrinsic bistability in quantum point contacts with in-plane side gates, Applied Physics Letters, 102(11) (2013).
10. N. Bhandari, M. Dutta, J. Charles, M. Cahay, R.S. Newrock, Hysteresis in the conductance of asymmetrically biased GaAs quantum point contacts with in-plane side gates, Journal of Applied Physics, 114(3) (2013).
11. P.P. Das, N. Bhandari, J. Wan, J. Charles, M. Cahay, K. Chetry, R.S. Newrock, and S.T. Herbert, Influence of surface scattering on the anomalous plateaus in an asymmetrically biased InAs/InAlAs quantum point contact, Nanotechnology 13, 215201 (2012).

## Book Chapter

1. N. Bhandari, M. Dutta, J. Charles, J. Wan, M. Cahay, S.T. Hebert, Potential Applications of All Electric Spin Valves Made of Asymmetrically Biased Quantum Point Contacts in Nanomagnetic and Spintronic Devices for Energy-Efficient Memory and Computing by J. Atulasimha and S. Bandyopadhyay (2016).
2. J. Wan, J. Charles, M. Cahay, P.P. Das, N. Bhandari, and R.S. Newrock, Influence of impurity and dangling bond scattering on the conductance anomalies

of side gated quantum point contacts in Nanoelectronic Device Applications Handbook, James Morris and Krzysztof Iniewski, Editors, CRC Press, Taylor and Francis (2013).

## Conferences

1. J. Charles, S. Kais, T. Kubis, Modeling Molecules in Interacting Environments ACS National Meeting and Exposition 2018, March 18-22, New Orleans Louisiana
2. J. Charles, P. Sarangapani, Y. Chu, G. Klimeck, T. Kubis Non-Local Scattering with a New Recursive Nonequilibrium Greens Function Method IWCE 2017, June 7-9, Windermere, United Kingdom.
3. K.C. Wang, T. Stanev, D. Valencia, J. Charles, P. Sarangapani, A. Henning, V. Sangwan, A. Lahiri, M. Povolotskyi, A. Afzalian, G. Klimeck, L. Lauhon, N. Stern, and T. Kubis Stark effect in the photoluminescence of transition metal dichalcogenide structures IWCE 2017, June 7-9, Windermere, United Kingdom.
4. P. Sarangapani, Y. Chu, J. Charles, G. Klimeck, and T. Kubis Non-equilibrium Greens function method: Band tail formation in non-local polar optical phonon scattering IWCE 2017, June 7-9, Windermere, United Kingdom
5. Y. Chu, P. Sarangapani, J. Charles, M. Povolotskyi, G. Klimeck, and T. Kubis Nonequilibrium Greens function method: Performance prediction of band-to-band tunneling devices with electron-only representation IWCE 2017, June 7-9, Windermere, United Kingdom.
6. P. Long, J.Z. Huang, M. Povolotskyi, D. Verreck, J. Charles, T. Kubis, M.J.W Rodwell, B.H. Calhoun A Tunnel FET Design for High-current, 120 mV Operation IEDM (2016).
7. K.C. Wang, D. Valencia, J. Charles, Y. He, M. Povolotskyi, G. Klimeck, J. Maassen, M. Lundstrom, T. Kubis, NEMO5: Predicting MOS2 Heterojunctions SISPAD (2016)

8. Y. Maeda, T. Sakurai, J. Charles, M. Povolotskyi, G. Klimeck and J.E. Roman  
A parallel eigensolver using numerical quadrature for annular regions EPASA  
September 14-16, 2015, Tsukuba, Japan.
9. A. Afzalian, J. Huang, H. Ilatikhameneh, J. Charles, D. Lemus, J Bermeo Lopez,  
S. Perez Rubiano, T. Kubis, M. Povolotskyi, G. Klimeck, M. Passlack, Y.C. Yeo,  
Mode Space Tight Binding Model for Ultra-fast Simulations of III-V Nanowire  
MOSFETs and Heterojunction TFETs (IWCE) 2015.
10. P. Sarangapani, D. Mejia, J. Charles, W. Gilbertson, H. Ilatikhameneh, T.  
Ameen, Andrew Roche, Jim Fonseca, Gerhard Klimeck, Quantum dot lab: an  
online platform for quantum dot simulations International Workshop on Com-  
putational Electronics (IWCE), 2015.
11. P. Sarangapani, Y. Tan, J. Charles, T. Ameen, J. Geng, M. Povolotskyi, T.  
Kubis, G. Klimeck, Atomistic Tight Binding Simulations with Real Space Basis  
Functions: Optical Properties of Quantum Wells and Dots IWCE 2014, June  
3-6, Paris, France.
12. J. Charles, M. Povolotskyi, Y. He, D. Lemus, Y. Maeda, T. Kubis, G. Klimeck,  
and T. Sakurai, "Applications of Eigenvalues Solvers in Nanoelectronic Device  
Modeling" EPASA March 7-9 2014, Tsukuba, Japan.
13. T. Ameen, H. Ilatikhameneh, J. Charles, Y. Hsueh, S. Chen, J. Fonseca, M.  
Povolotskyi, R. Rahman, "Optimization of the Anharmonic Strain Model to  
Capture Realistic Strain Distributions in Quantum Dots" IEEE Nano, Toronto,  
August 2014
14. N. Bhandari, J. Charles, M. Dutta, P. Das, M. Cahay, R. Newrock, S. Herbert,  
Tunable All Electric Spin Polarizer Using a Quantum Point Contact With Two  
Pairs of In-Plane Side Gates APS (2013).



VITA

## VITA

James Charles was born in Cincinnati, Ohio on October 1st, 1989. He attended the University of Cincinnati from 2008 to 2013. He graduated with a bachelor's degree in electrical engineering in 2013. He joined Purdue University in the same year to pursue his PhD in electrical engineering in the iNEMO group. He received his Master's degree in electrical engineering in 2016 and continued with his PhD. His research interests are in quantum transport algorithms and method development.